

NOVEL ALGORITHMS FOR X-RAY COMPUTED TOMOGRAPHY

By

Peter Lekeaka-Takunju

A DISSERTATION

Submitted to
Michigan State University
in partial fulfillment of the requirements
for the degree of

DOCTOR OF PHILOSOPHY

Electrical Engineering

2011

ABSTRACT

NOVEL ALGORITHMS FOR X-RAY COMPUTED TOMOGRAPHY

By

Peter Lekeaka-Takunju

X-ray computed tomography (CT) is a non-destructive technique for assessing the structural integrity of an object without compromising its usefulness. This imaging modality uses a number of projection measurements of the attenuated X-rays after passing through the object at different angles of incident beam orientation. The object is reconstructed from these projection measurement data usually using Filtered Backprojection (FBP) Algorithm which is based on Fourier Slice Theorem. FBP however assumes ideal conditions, notably monoenergetic X-ray photons and the availability of a very large number (hundreds and even thousands) of projections.

However in practice, X-ray sources are polychromatic producing X-rays photons of varying energies and intensities. The X-ray attenuation of a material depends on energy, being high at low incident energy and decreasing as incident energy increases. This leads to an undesirable effect called beam hardening (BH). BH results in an underestimation of the attenuation values of the FBP reconstructed image, degrading it and thus potentially rendering it diagnostically unusable. In this thesis we propose a novel model-based correction scheme for BH based on the Lambert-Beer's law for polychromatic X-rays, knowledge of source spectrum and computer-aided design (CAD) model of the specimen. The validity of the correction scheme is demonstrated on a uniform tungsten alloy rod through simulation and experiment conducted using a 320 kV_p X-ray source. It is found that the application of this correction scheme improves the beam hardened CT reconstructed image, particularly reducing the BH cupping artifact inherent in FBP reconstructed images. The proposed

technique is evaluated using two quantitative metrics of the reconstructed image.

The application of X-ray CT in the nuclear industry to inspect nuclear fuel rods is discussed in this thesis. For real-time tomography, data acquisition time is critical. In order to reduce the time for imaging there is a need to develop reconstruction algorithms using as few projections as possible. However limited number of projections implies an insufficiently filled Radon Space rendering imaging via FBP algorithm unsuitable. Any attempt to invert from the insufficiently filled Radon space back to the object space during the reconstruction problem gives rise to undesired artifacts which should be removed. In this thesis a novel artifact removal algorithm is proposed and its performance is demonstrated using both simulation and experimental data. A statistical reconstruction algorithm for reconstruction from a limited number of projections is also presented. The reconstruction results proves the technique to be promising in obtaining accurate inversion results, even in the presence of an extremely limited number of X-ray projections and noise. Availability of limited projections renders the X-ray CT problem ill-posed. In this thesis, X-ray CT problem is reformulated in terms of matrix product to facilitate the application of Tikhonov inversion technique. Reconstruction results obtained using a limited number of simulation and experimental data are shown and compared with FBP reconstructed results. It is relevant to note here that the new inversion technique is independent of any *a priori* information.

ACKNOWLEDGMENTS

I would like to acknowledge the advice and guidance of my academic advisor, Prof. Lalita Udpa. I thank her for her encouragement and financial support throughout my doctoral study. Special thanks also goes to my co-advisor, Prof. Satish Udpa for his guidance and suggestions.

I also wish to express my sincere gratitude to my committee members Prof. Vladimir Zelevinsky, Prof. Edward Rothwell, and Prof. Prem Chahal for their unfailing support in my doctoral study. Their advice on technical matters, encouragement, motivation and constructive criticism are greatly acknowledged.

Many thanks to George Harmon, development engineer at the Chrysler's Non-Destructive Evaluation (NDE) laboratory for helping me with experimental data collection at the Chrysler facility in Auburn Hills, Michigan. The experimental work performed in the NDE laboratory here at MSU would not have been possible without the help of Brian Wright, Research Equipment Technologist at the ECE department, Michigan State University. I really appreciate his technical assistance.

I would like to thank all members of the NDE laboratory for creating a nice working environment. I am grateful to Dr. Tariq Khan for his stimulating conversations and suggestions.

Finally, I wish to express my heartfelt gratitude to my family, especially my wife and in-laws for the constant support and encouragement. Their support and encouragement made my doctoral study possible. I also acknowledge the patience and understanding of my beloved daughter, Kasey throughout this period.

TABLE OF CONTENTS

List of Tables	viii
---------------------------------	-------------

List of Figures	ix
----------------------------------	-----------

1 Introduction	1
-----------------------	----------

1.1 Background and Motivation	1
---	---

1.2 Organization	9
----------------------------	---

1.3 Contributions	10
-----------------------------	----

2 X-ray Physics	13
------------------------	-----------

2.1 Introduction	13
----------------------------	----

2.2 Production of X-rays	14
------------------------------------	----

2.2.1 The X-ray Source	14
----------------------------------	----

2.2.2 Bremsstrahlung Radiation	15
--	----

2.2.3 Characteristic Radiation	16
--	----

2.3 X-ray Interaction with Matter	17
---	----

2.3.1 Classical (Coherent) Scattering	17
---	----

2.3.2 Photoelectric Effect	18
--------------------------------------	----

2.3.3 Compton Scattering	19
------------------------------------	----

2.3.4 Pair Production	20
---------------------------------	----

2.3.5 Photodisintegration	22
-------------------------------------	----

2.4 X-ray Detectors	22
-------------------------------	----

2.4.1 X-ray Photographic Plates, Films and Fluoroscopy	23
--	----

2.4.2 Flat Panel Detectors	24
--------------------------------------	----

2.4.2.1 Amorphous Silicon Flat Panel Detectors	24
--	----

2.4.2.2 Amorphous Selenium Flat Panel Detectors	27
---	----

3	X-ray Computed Tomography	29
3.1	Introduction to X-ray Computed Tomography	29
3.2	Applications of X-ray Computed Tomography	30
3.3	Radon Transform and the Fourier Slice Theorem	31
3.4	Image Reconstruction by Filtered Backprojection Algorithm	34
3.5	Artifacts in X-ray Computed Tomographic Images	35
4	A Model-based Correction Scheme for Beam Hardening in X-ray Computed Tomography	37
4.1	Proposed Model-Based Correction Scheme	37
4.2	Results with Simulation Data	41
4.3	Results with Experimental Data	44
4.4	Parametric Study	47
4.4.1	Cupping Artifact as a Function of Source Energy	47
4.4.2	Performance of Correction Scheme at Different Contrasts	48
4.5	Conclusion	50
5	Nuclear Fuel Rods Inspection using X-ray Computed Tomography	51
5.1	Introduction	51
5.2	Existing Methods of Nuclear Fuel Rods Inspection	53
5.2.1	Ultrasonic Inspection	53
5.2.2	Visual Inspection and Photography	55
5.2.3	Eddy Current Inspection	56
5.2.4	Sipping Test	56
5.3	Assessment of Nuclear Fuel Pellets using X-ray Computed Tomography	57
5.3.1	Convex Interpolation in the projection domain	58
5.3.2	Simulation and Results	60
5.3.3	Experimental Validation of Convex Interpolation Technique	65
5.3.4	Implementation Results with Low Contrast Data	69
5.3.5	Reconstruction Error as a Function of Number of Projections	70

5.4	Conclusion	71
6	X-ray Tomographic Inspection of Nuclear Fuel Rods using a Limited Number of Projections	73
6.1	Introduction	73
6.2	Experimental work and Projections	74
6.3	Tomographic Reconstruction	77
6.3.1	The Filtered Back-projection Algorithm	77
6.3.2	Statistical Reconstruction Algorithm	78
6.4	Proposed Technique	80
6.5	Results with Experimental data	82
7	Tikhonov Inversion Technique in X-ray Computed Tomography	84
7.1	Introduction	84
7.2	Problem Formulation	85
7.3	Implementation Results with Simulation Data	91
7.4	Results with Experimental Data	94
8	Conclusion and Future Work	99
	Bibliography	103

LIST OF TABLES

4.1	Quantitative Measures	47
-----	---------------------------------	----

LIST OF FIGURES

1.1	Energy dependence of X-ray beam	5
1.2	Energy dependence of material attenuation	5
1.3	Logarithmic Attenuation as a function of mass absorption thickness [3]	6
1.4	Illustration of cupping artifact due to X-ray beam polychromaticity	7
2.1	Schematic overview of an X-ray source and its components [19]	14
2.2	Illustration of X-ray production at the anode	16
2.3	Illustration of coherent scattering	18
2.4	Illustration of the photoelectric effect	19
2.5	Illustration of Compton scattering	19
2.6	Percentage of different types of interactions as a function of energy in water [2]	21
2.7	Illustration of pair production mechanism	21
2.8	Illustration of photodisintegration mechanism	22
2.9	Schematic drawing of a-Si FPD	25
2.10	Principle of operation of Indirect X-ray detector	25

2.11	Photograph of an a-Si Flat Panel Detector	27
2.12	Schematic diagram showing concept of a-Se FPD	27
3.1	Principles of Fan-beam X-ray CT	30
3.2	An object, $f(x,y)$, and its object, $P(s_1, \theta)$ are shown for an angle of θ [27]	32
3.3	The Fourier Slice Theorem	34
3.4	Steps involved in Filtered-Backprojection Reconstruction Algorithm	36
4.1	An Overview of the Correction Technique for reducing BH effects	38
4.2	Coordinate Transformation from (x, y) to (s, θ) [28]	39
4.3	Spectral Plot of Mass Attenuation Coefficients of Tungsten up to 300 keV	41
4.4	Comparison of projection data	43
4.5	CT reconstructed images	43
4.6	CT reconstructed attenuation values showing cupping artifact	44
4.7	Phantom with Defects	44
4.8	CT reconstructed images with defects	45
4.9	Experimental set-up	45
4.10	Experimental projection data	46
4.11	Experimental CT reconstructed images	47

4.12	CT reconstructed attenuation values showing cupping artifact at 100 keV, 200 keV and 300 keV	48
4.13	CT reconstructed images with 5% contrast defects	49
4.14	CT reconstructed images with 10% contrast defects	49
4.15	CT reconstructed images with 15% contrast defects	49
5.1	A missing pellet surface and through-wall crack of a failed fuel rod	52
5.2	Sample 1 with notch defect at UO_2 /zircaloy interface	60
5.3	Original and Interpolated sinograms	61
5.4	Reconstructed Images with 60 projections	61
5.5	Reconstructed Images with 9 projections	61
5.6	Performance on non-symmetric defect	62
5.7	Reconstruction results with Convex Interpolation	63
5.8	Results using 30 projections on sample with real defect	64
5.9	Cross-sectional diagram of the test sample with machined defects	65
5.10	Side view of the sample mounted on a rotational stage	66
5.11	Raw 2-D radiographic data of the sample taken at angle 0°	66
5.12	Projection data acquired at angle 0°	67

5.13	Reconstructed result with convex interpolation	68
5.14	Result with convex interpolation and thresholding	68
5.15	FBP reconstructed result without convex interpolation	69
5.16	Phantom with defects	70
5.17	Reconstructed Images with 9 projections	70
5.18	Mean square error as a function of number of projections	71
6.1	Mass Attenuation Coefficients for UO_2 and W	74
6.2	Photograph of Tungsten rod alongside Zircaloy cladding	75
6.3	Experimental Set-Up (side view) of CR system	75
6.4	Experimental Projections	76
6.5	Experimental Projections	76
6.6	Experimental Projections	77
6.7	Experimental Projections	77
6.8	Reconstruction using FBP algorithm	81
6.9	Initial guess	82
6.10	Reconstructed cross-section using experimental projections	82
6.11	Reconstructed cross-section using experimental projections	83

7.1	M×N imaging space in fan-beam geometry	89
7.2	Phantom with Defects	91
7.3	Simulated projection data acquired at angle 0°	92
7.4	Reconstructed cross-section using 10 simulated projections	93
7.5	FBP reconstructed cross-section using 10 simulated projections	94
7.6	Cross-sectional diagram of the test sample with machined defects	95
7.7	Side view of the sample mounted on a rotational stage	95
7.8	Raw 2-D radiographic data of the sample taken at angle 0°	96
7.9	Projection data acquired at angle 0°	97
7.10	Reconstructed cross-section using 12 experimental projections	97
7.11	FBP reconstructed cross-section using 12 experimental projections	98

Chapter 1

Introduction

1.1 Background and Motivation

In 1895, the German Physicist Wilhelm Conrad Röntgen (1845-1923) discovered X-rays while attempting to see if any radiation could be produced which would traverse matter opaque to ordinary light. While experimenting with an electric discharge through a highly evacuated tube, Röntgen noticed that a phosphor screen located at some distance from the tube fluoresced. In an attempt to stop this fluorescence, he put various objects in the way of this unknown radiation, finally putting his hand in front of the screen and seeing a shadowed image of his bones. This was the first radiograph and hence the birth of radiography. He named this radiation as *X-rays* indicating their unknown nature, though many referred to the radiation as *Röntgen rays* for several decades after their discoverer. Röntgen has been accredited as the discoverer of X-rays because he was the first to perform a systematic study on them, though he was not the first to have observed their effects.

Although in imaging, a radiograph represents a two dimensional image of a three dimensional object, it does not give any information about the depth. For example, a shadow image (radiograph) of a patient may reveal a broken bone but not other subtle problems present. Also in radiography, there is superimposition of images of structure outside the region of interest. Hence, there is a need of a better imaging technique. These problems can be overcome by reconstructing an object using projection data about the object obtained by illuminating the object with X-rays from many different directions and orientations. This type of imaging is known as *X-ray Computed Tomographic (X-ray CT) Imaging*. Tomography comes from two Greek words: *tomos* (meaning: *slice* or *section*) and *graphein* (meaning: *to write*). Thus tomography is imaging by section or sections using information about the interaction of energy with the object being imaged. CT was the first non-invasive radiological method allowing the generation of tomographic images of every part of an object without superimposition of adjacent structures.

The first CT scanner was invented by Sir Godfrey Hounsfield in Hayes, United Kingdom at EMI Central Research Laboratories using X-rays for which he received a Nobel Prize in 1979. This was the major breakthrough from which the current excitement in tomographic imaging originated although back in 1917 the Austrian Mathematician Johann Karl August Radon (1887-1956) provided solution to the mathematical problem on how to reconstruct a function from its projections.

According to Radon theory, given an unknown function f of an object, then the line integral of f along a straight line inclined at an angle θ is called the *projection* or *Radon Transform* of f at that angle θ . Thus projections of an object represent an analytic transform for that object. Hence the inverse of the Radon Transform can be used to reconstruct the original function f from the projection data and thus this forms the mathematical basis for tomographic reconstruction.

The transmitted intensity I of a monochromatic beam of photons of incident intensity I_0 as it passes through a homogeneous material of mass thickness t and attenuation coefficient μ is given by the Beer-Lambert's law:

$$I(t) = I_0 e^{-\mu t} \Rightarrow -\ln\left(\frac{I}{I_0}\right) = \mu t \quad (1.1)$$

From Equation (1.1), the attenuation is a linear function of the mass thickness t .

If the material is heterogeneous, the simple product μt in Equation (1.1) can be replaced by a line integral and the transmitted intensity through the material with spatial distribution of attenuation coefficient $\mu(x, y)$ at the point (x, y) can be expressed as [1]:

$$I = I_0 e^{-\int_L \mu(x, y) du} \quad (1.2)$$

where L is the path of the ray and u is the length along L . By measuring the natural logarithm of the intensity ratio at different sensor positions s on the detector array and several source locations θ , we obtain:

$$p(s, \theta) = \ln\left(\frac{I_0}{I}\right) = \int_L \mu(x, y) du \quad (1.3)$$

The quantity $p(s, \theta)$ is termed the *projection* or *Radon Transform* of μ at an angle θ .

CT scanners record the X-ray projection data at different angles of incident beam orientation. These recorded projection data are then used to reconstruct the object using an image reconstruction algorithm. There are several image reconstruction algorithms available and these can be grouped into *analytical*, *algebraic* and *statistical*. Of these available algorithms, the most widely used is the analytical algorithm called the *Filtered-Backprojection* (FBP) algorithm. FBP is based

on Radon Transform and the Fourier Slice Theorem and is used in almost all available commercial CT scanners thanks to its easy practical implementation which takes advantage of the Fast Fourier Transform (FFT). FBP is fast and deterministic, and its properties are very well understood.

The Radon Transform however assumes ideal conditions, namely: monoenergetic X-ray photons, infinite number of projections with infinitely thin X-ray beams, noiseless data, etc. Any deviation from these ideal conditions will lead to artifacts in the reconstructed image. Of particular significance is the problem of assuming a monochromatic X-ray source. The attenuation of an object is linearly dependent on mass thickness of that object according to the Beer-Lambert's law of Equation (1.1) when a monochromatic source is assumed. However in practice, monochromatic X-ray sources do not exist. All X-ray sources are polychromatic, producing photons of varying energies and intensities. X-ray photon attenuation coefficient of a material depends on energy, being high at low photon energy and decreases as the photon energy increases. Figures 1.1 and 1.2 illustrate the energy dependence of a polychromatic beam of X-rays and material attenuation respectively. The peak energy of the X-ray source is 300 kV_p and the material is Tungsten alloy (with density 18.5 g/cm³).

Because of this energy dependence of the attenuation coefficients, each of the photons in the polychromatic beam will experience a different attenuation. This can be described mathematically by the following relationship [2]:

$$I = I_0 \int \Omega(E) e^{-\int_L \mu(x, y, E) du} dE \quad (1.4)$$

Here $\Omega(E)$ represents the incident X-ray spectrum, the area under which is unity. Obtaining the projections from Equation (1.4) by taking the natural logarithm of the transmitted to incident ratio

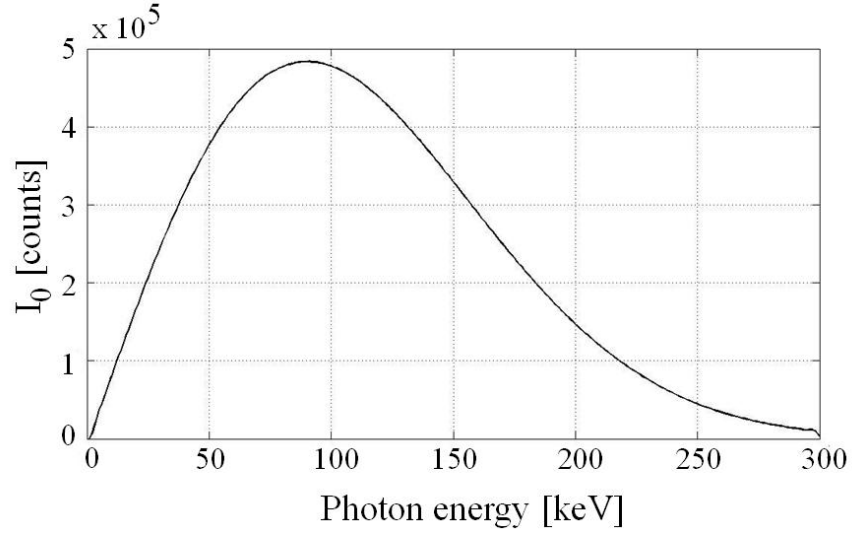


Figure 1.1: Energy dependence of X-ray beam

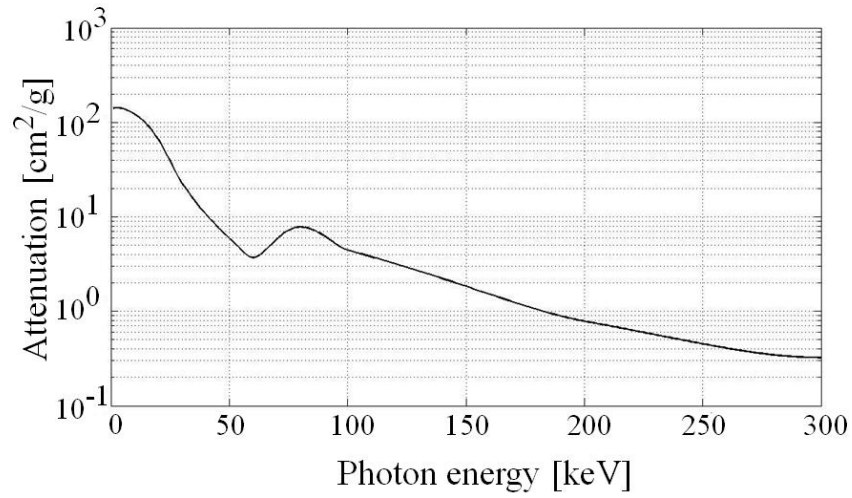


Figure 1.2: Energy dependence of material attenuation

gives:

$$p(s, \theta) = -\ln \left(\frac{I}{I_0} \right) = -\ln \left(\int \Omega(E) e^{-\int_L \mu(x, y, E) du} dE \right) \quad (1.5)$$

Comparing Equation (1.5) to Equation (1.1), the linear relationship between the logarithmic attenuation (measured projection p) and the path length of the material no longer holds for actual polychromatic sources as shown in Figure 1.3 [3].

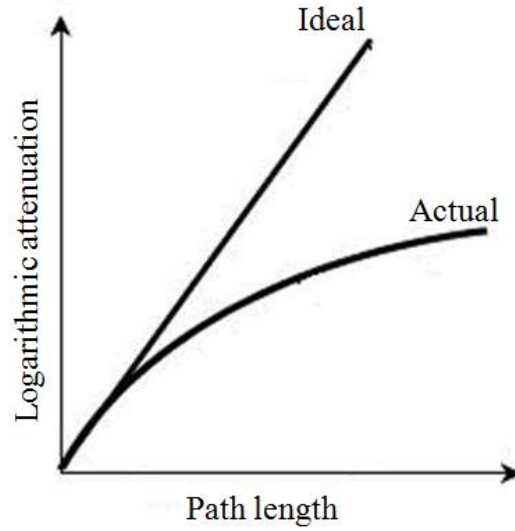


Figure 1.3: Logarithmic Attenuation as a function of mass absorption thickness [3]

BH results in an underestimation of the attenuation values in the reconstructed image using FBP especially along the ray path where this phenomenon is well-pronounced. This results in artifacts such as streaks, edges and cupping which are generally referred to as *beam hardening artifacts*. In Figure 1.4, a circular uniform homogeneous phantom was simulated and used to illustrate cupping artifact. Monochromatic and polychromatic projections were acquired from this phantom using at 300 kV_p peak voltage of the X-ray source. Reconstruction from these projection data was done using the FBP algorithm with 180 projections and 258 parallel rays in each projection. Figures 1.4a and 1.4b show the reconstructed phantom for both the monochromatic and polychromatic cases respectively. For comparison, horizontal line profiles taken through the middle part of the CT reconstructed images are shown in Figures 1.4c and 1.4d, from where the cupping artifact due to BH can be observed.

Apart from the visual effects associated with these artifacts, it can be difficult to interpret the reconstructed images quantitatively especially in medical imaging because these artifacts change the

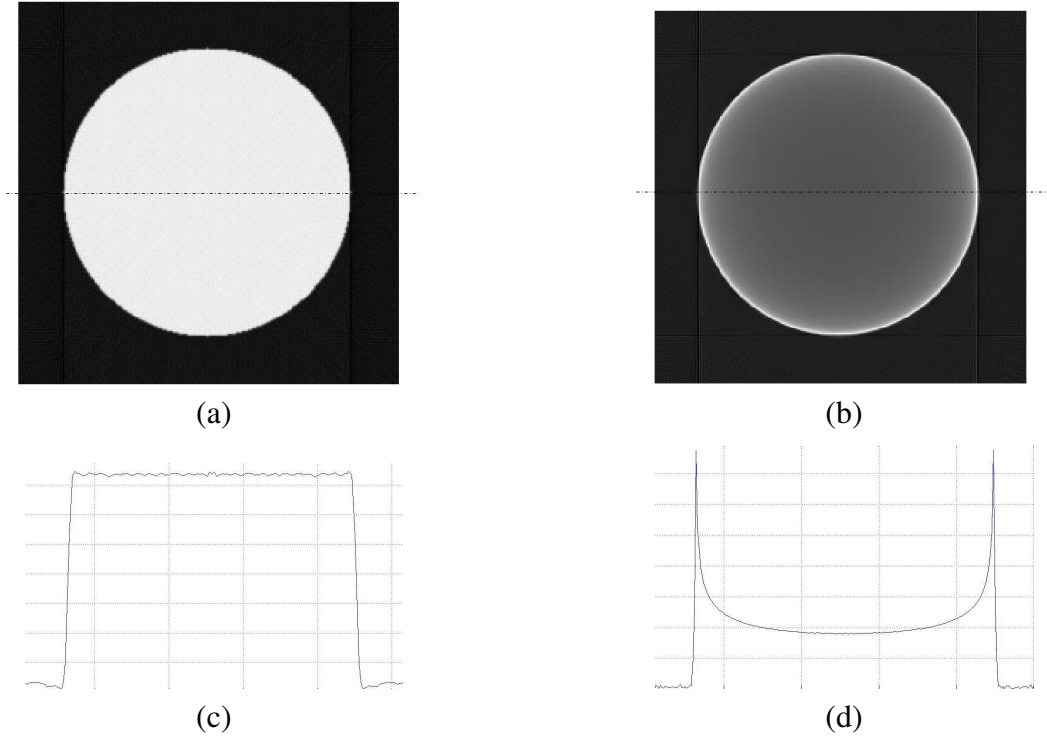


Figure 1.4: Reconstructed Images: (a) Monochromatic (b) Polychromatic; and their horizontal line profiles: (c) Monochromatic and (d) Polychromatic illustrating cupping artifact due to Polychromaticity.

attenuation of the object [4] resulting in diagnostic errors. In diagnostic imaging, the attenuation values of the reconstructed image is translated to an integer (CT number) measured in Hounsfield units (HU). CT numbers are relative to the attenuation of water, which is assigned a value of 0 HU. Other examples include bone (+1000 HU), liver (40-60 HU), blood (40 HU), fat (-50 to -100 HU) and air (-1000). The accuracy of the CT number plays an important role in accurate diagnosis, especially in cases where threshold identification is used [5]. This accuracy is remarkably degraded by the artifacts induced by BH effects.

The problem of beam hardening correction (BHC) or reduction in CT has been an active research area for over four decades [6, 7]. Several schemes have been proposed and used to correct BH and they generally fall under:

1. *Hardware filtering*, the most popular method where a filter such a thin aluminum plate is placed between the source and the object. This helps to absorb the lower energy photons and allow only the higher energy photons to go through the object under test. But this scheme results in very low signal-to-noise ratio and the reconstructed image is very noisy [8]. Also the choice of filter should be appropriate for maximum effect and details on choice of filter materials are given in [9].
2. *Pre-processing*, a technique that mainly involves compensating for the departure from linearity of the relationship between the measured projection data and path length of the object [10]. This approach generally works well for low attenuating materials like soft tissues but fails in the presence of high attenuation materials.
3. *Post-processing*, , this involves an initial reconstruction from which the material distribution is estimated [11]. A BH factor is then estimated from this distribution and used to correct the measured projection data. A new reconstruction is then computed from these corrected measurements. The process is time-consuming as it is iterative and this technique does not offer much improvement in the presence of a material with very high atomic number.
4. *Dual energy imaging*, a technique whereby two separate scans are taken at two different energy windows [7]. However, this technique is complex to implement, very sensitive to noise, requires more exposure to radiation and data acquisition and is material dependent.

Apart from the above-mentioned correction techniques, there have been significant interest recently in applying different reconstruction approach for tomographic reconstruction, particularly statistical iterative algorithms [12, 13] which have been motivated by their success in emission tomography namely: Positron Emission Tomography (PET) and Single Photon Emission Computed

Tomography (SPECT). These statistical reconstruction algorithms however already have very long computation time and difficult to implement in a commercial CT scanner as compared to the standard FBP algorithm. Owing to the fact that almost all commercial CT scanners today produced by major CT manufacturers still implement FBP, there is a motivation to continue developing novel versions of FBP algorithms that can overcome the existing drawbacks. This thesis presents novel FBP algorithms that can overcome the existing inherent beam hardening effects due to polychromaticity faced by the standard FBP algorithm. For real time tomography, data acquisition time is critical. This calls for the need of tomographic reconstruction from limited number of projections. This thesis also presents the development of novel algorithms for tomographic reconstruction from limited number of X-ray projections and their application in the nuclear industry to inspect nuclear fuel rods.

1.2 Organization

In this chapter, the background and the motivation behind this thesis is discussed. In particular, beam hardening phenomenon is illustrated by simulation. An overview of existing beam hardening correction schemes is presented together with their drawbacks. The chapter concludes with an outline of the contributions of this thesis. Chapter 2 discusses some fundamentals of X-ray physics including their production, interaction with matter and detection. In Chapter 3, the principles of X-ray CT are presented. Radon Transform and the Fourier Slice Theorem, which form the basis of the FBP algorithm, are covered. Artifacts in X-ray computed tomographic images are also introduced. Chapter 4 presents a model-based correction scheme for beam hardening artifacts in X-ray CT. Both simulation and experimental results are presented. A systematic study of the influence of the beam hardening effect at different energy levels is also presented in this chapter. The evaluation of

the performance of the proposed model-based correction scheme is also presented as a function of contrast. Chapter 5 describes the application of nuclear fuel rods inspection in the nuclear industry. Current methods of nuclear fuel rods inspection are presented together with their drawbacks. The application of X-ray CT in the nuclear industry to inspect nuclear fuel rods is discussed. X-ray tomographic inspection of nuclear fuel rods using a limited number of projections is given in Chapter 6. A statistical reconstruction technique is presented together with experimental results. X-ray CT problem is reformulated in Chapter 7 in terms of matrix product. Tikhonov inversion technique is then applied to solve the ill-posed X-ray tomographic reconstruction problem without any *a priori*. Chapter 8 concludes the thesis with a summary of the accomplished research work. A discussion on the future work stemming from this research is also presented.

1.3 Contributions

In this thesis, novel algorithms for beam hardening correction and reconstruction from limited projections in X-ray CT are presented. These algorithms are applied to reduce cupping artifacts caused by beam hardening and also to the problem of nuclear fuel rod inspection in the nuclear industry. To this end, the following contributions are made by the thesis:

- A model-based correction scheme for beam hardening artifacts in X-ray CT is proposed [14]. This correction scheme is based on the Lambert-Beer's law for polychromatic X-rays, knowledge of source spectrum and CAD model of the specimen. The validity of the correction scheme is demonstrated on a uniform tungsten alloy rod through simulation and experiment conducted using a 320 kV_p X-ray source. It is found that the application of this correction scheme improves the beam hardened CT reconstructed image, particularly reducing the BH cupping artifact inherent in FBP reconstructed images. The proposed technique

is evaluated using two quantitative metrics of the reconstructed image. A systematic study of the influence of the beam hardening effect at different energy levels is also presented. The evaluation of the performance of the proposed model-based correction scheme is also presented as a function of contrast.

- Assessment of nuclear fuel pellets using X-ray CT is investigated in this thesis [15]. Current methods of nuclear fuel rods inspection are presented together with their drawbacks. The application of X-ray CT in the nuclear industry to inspect nuclear fuel rods is discussed. In this work, a novel convex interpolation method is proposed and used to interpolate the projection data and completely fill up the Radon space which was otherwise partially filled with limited projections.
- Experimental validation of the convex interpolation technique on data acquired from a high density polyethylene rod with machined defects [16]. The experimental projections were acquired using a GE vertical X-ray inspection system having a 150 kVp microfocus X-ray source from Hamamatsu and peak current of 500 μ A. Since the X-ray source and detector are both fixed, the sample was mounted on a rotational stage to get a complete tomographic scan. This rotational stage was controlled by labview software. The sample was rotated at regular angular intervals over a complete range (0 to 360 $^{\circ}$) to collect projection data from different directions. Reconstruction of a cross-sectional slice of the rod using 18 experimental projections with convex interpolation is shown and compared with results obtained using conventional methods.
- The feasibility of using X-ray tomographic inspection technique for detection and characterization of defects in fuel pellets using a limited number of projections is investigated [17]. In this work, a statistical recursive algorithm is proposed and implemented on eight

experimental projections obtained using 320 kV_p and 13 mA X-ray source. Tomographic reconstruction results of the cross-section of the nuclear fuel rod are presented.

- The use of Tikhonov inversion technique in X-ray CT using a limited number of projections is given [18]. In this work, X-ray CT problem is reformulated in terms of matrix product. This reformulation enables the application of Tikhonov inversion technique to solve the ill-posed X-ray tomographic reconstruction problem. Reconstruction results with a limited number of simulation and experimental data are presented and compared with FBP reconstructed results. It is relevant to note here that the new inversion technique is independent of any *a priori* information.

Chapter 2

X-ray Physics

2.1 Introduction

X-rays are a form of electromagnetic radiation having wavelengths in the range from 10 nm down to 10 pm, corresponding to frequencies in the range from 30 PHz to 30 EHz (3×10^{16} Hz to 3×10^{19} Hz). They are longer in wavelength than gamma rays but shorter than ultra-violet radiation. X-rays are described by the intensity I (number of photons) and energy E of their photons. The energy E is proportional to the frequency, ν of the radiation by [2]:

$$E = h\nu = h\frac{c}{\lambda} \quad (2.1)$$

where

h is Planck's constant (6.63×10^{-34} Js)

c is the speed of light in free space (3×10^8 m/s)

λ is the wavelength of the X-ray radiation

This chapter describes the types of interaction that lead to the production of X-rays and the mechanisms of interactions of these X-rays with matter. The underlying principles of operation and types of X-ray detectors are also discussed in the chapter.

2.2 Production of X-rays

X-rays are produced when fast-moving electrons bombard a target material. Upon this collision, part of the kinetic energy of the projectile electrons is transformed to the energy of the released X-rays and part (about 99 %) is lost as heat in the target material.

2.2.1 The X-ray Source

Figure 2.1 is a schematic overview of an X-ray source consisting of a cathode and an anode inside a vacuum tube [19].

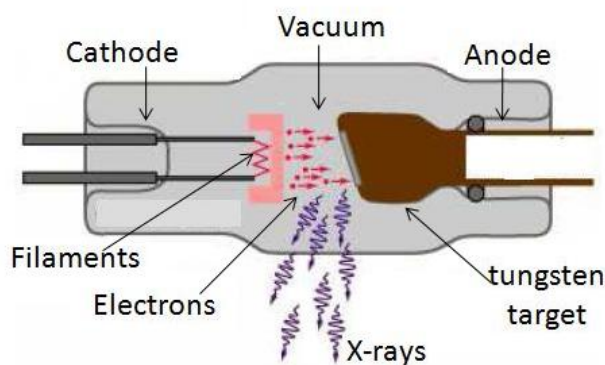


Figure 2.1: Schematic overview of an X-ray source and its components [19]. For interpretation of the references to color in this and all other figures, the reader is referred to the electronic version of this dissertation.

The cathode is the negative electrode which consists of a helical filament made up of tungsten wire. The filament provides the electrons for acceleration to the target electrode (anode). The anode is the positive terminal of the X-ray tube and is made up of a material with very high atomic

number and melting point. Tungsten metal is the most commonly used anode material. The anode serves three important functions, namely:

1. It completes the circuit for providing potential difference to accelerate electrons
2. It houses the target material for X-ray production
3. It helps to dissipate the heat produced in the tube

High-speed electrons are released from the heated filament of the cathode by thermionic emission. These electrons are accelerated towards the anode by the potential difference applied between the cathode and the anode. When these accelerated electrons strike the target material of the anode, two types of X-ray radiation are produced, namely: *Bremsstrahlung* and *Characteristic* radiation. The particular type of radiation produced depends on the mode of interaction of the high-speed electrons with the atoms of the target material as illustrated in Figure 2.2 [2].

2.2.2 Bremsstrahlung Radiation

Bremsstrahlung Radiation is generated by the interaction of an electron with the nucleus of an atom. A high-speed electron traveling near a nucleus experiences a sudden deceleration due to the coulomb's force of attraction between these oppositely charged particles as shown in Figure 2.2a. The partial loss of kinetic energy of the high-speed electron is given off as bremsstrahlung radiation, whose energy increases with the amount of the kinetic energy loss. This radiation covers a wide range of a continuous spectrum.

In a rare case when a high-speed electron collides head on with a nucleus, the total kinetic energy of the electron is given off to form a single photon with the highest energy in the bremsstrahlung spectrum. This type of interaction is illustrated in Figure 2.2c with an example of a 120 kV_p X-ray

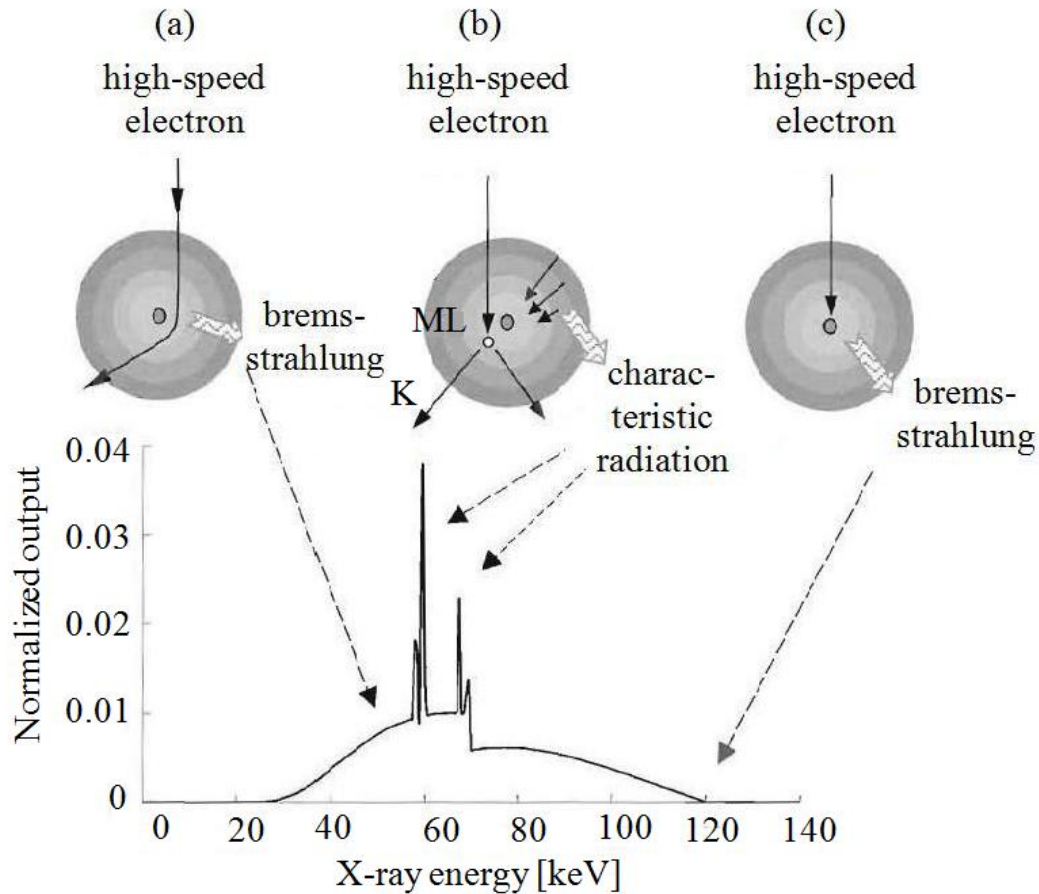


Figure 2.2: Illustration of electron interaction with an atom of the target and X-ray production (a) Bremsstrahlung Radiation, (b) Characteristic Radiation, and (c) Bremsstrahlung Radiation [2]

tube producing X-ray photons of 120 keV energy. However, the overall probability of occurrence of this type of bremsstrahlung radiation is very low as shown by the negligible magnitude in the spectrum. The X-ray energy produced by this interaction represents the upper energy limit in the X-ray spectrum.

2.2.3 Characteristic Radiation

A high-speed electron emitted by the cathode can also interact through collision with one of the inner-shell electrons of the target atom. If the kinetic energy of the high-speed electron exceeds the binding energy of the inner-shell electron, the inner-shell electron will be liberated leaving behind

a hole. When an electron from a higher energy outer shell fills this hole, a characteristic radiation is emitted with energy equal to the difference between the binding energies of the two shells as illustrated in Figure 2.2b for tungsten material. The radiation is discrete in nature and material dependent as each element of the periodic table has its own unique shell binding energies. Details on these binding energies and the characteristic X-rays produced during transition of an orbital electron from an outer shell to an inner shell for various elements can be found in [20].

2.3 X-ray Interaction with Matter

X-rays have wavelengths comparable to sizes of atoms and hence will penetrate deeply into a material before interacting with an individual atom leading to either their scattering or absorption. Generally, there are five basic modes of interaction of X-rays with matter with the probability of occurrence of each mode determined primarily by the energy of the incident X-ray photon and the atomic number of the matter. These modes of interaction are: *classical (Coherent) scattering*, *photoelectric effect*, *Compton scattering*, *pair production* and *photodisintegration*. All these modes of interaction of X-rays with matter lead to either scattering or the absorption of the X-ray photons.

2.3.1 Classical (Coherent) Scattering

Classical or coherent scattering is the mode of scattering experienced by low energy X-rays of about 10 keV when they interact with matter. Here the incident photon interacts with the whole atom of the matter. Upon incidence of an X-ray photon on the atom, the atom absorbs the photon and electrons of the atom oscillate at the frequency of the incident photon. The atom becomes unstable and emits a secondary photon at the same frequency as the incident photon. In this type of interaction, there is no energy transferred and no ionization occurs. The only effect is that the incident photon is scattered in the forward hemisphere and its direction is changed as shown in

Figure 2.3.

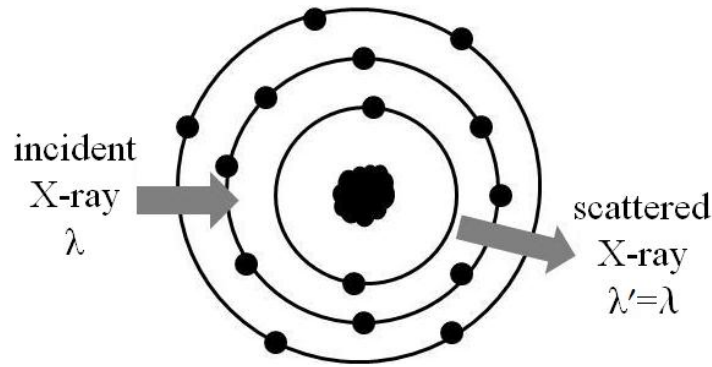


Figure 2.3: Illustration of coherent scattering

2.3.2 Photoelectric Effect

Photoelectric effect is a photon absorption effect which occurs when the X-ray photon incident on an atom of a material has energy greater than the binding energy of an electron of that atom. Some of the energy of the incident photon is used to overcome the binding energy of the interacting electron, thus ejecting the electron off from an inner electronic shell deep inside the atom leaving behind a hole. The free electron is often called a photoelectron. The incident photon ceases to exist as it also gives up its remaining energy as kinetic energy of the photoelectron, with which the photoelectron escapes. An electron dropping from a higher-energy-state outer shell to fill the hole will generate characteristic (secondary) X-rays with energy equal to the difference between the two energy states. This effect is illustrated in Figure 2.4.

The photoelectric effect is most probable when the incident photon energy is approximately equals to the binding energy of the electron. This gives rise to the so-called *K-edge* and *L-edge* in the absorption coefficient. The probability of occurrence of the photoelectric effect is roughly inversely proportional to the cube of the excess photon energy [21] and directly proportional to the cube of the atomic number [4]. A photoelectric interaction cannot occur unless the incident X-ray

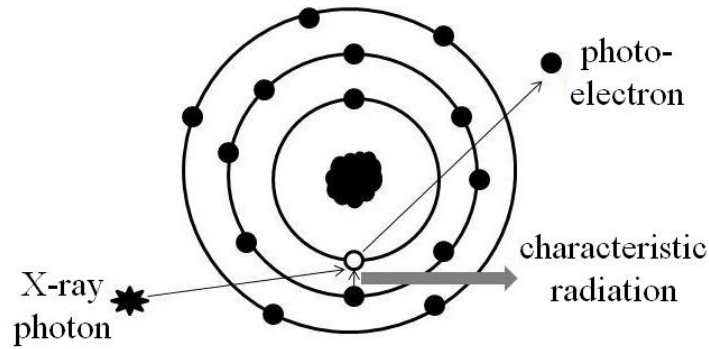


Figure 2.4: Illustration of the photoelectric effect

photon has energy equal to or greater than the electron binding energy.

2.3.3 Compton Scattering

Compton scattering, also known as incoherent scattering is the most important mechanism of interaction of X-rays in tissue-like materials [4]. It occurs when the incident X-ray photon has energy considerably higher than the binding energy of an outer-shell (free or valence) electron. When the incident X-ray photon strikes the outer-shell electron, it frees the electron from the atom. This mode of interaction of X-rays with matter gives rise to a positive ion, a "recoil" electron, and a scattered photon, which may be deflected at any angle from 0° to 180° as shown in Figure 2.5.

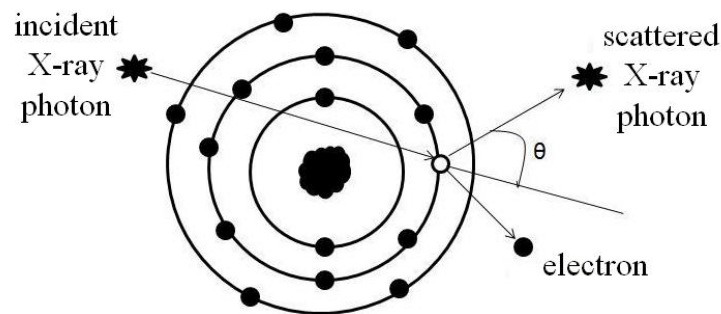


Figure 2.5: Illustration of Compton scattering

The incident X-ray photon suffers some partial loss of its initial energy. The amount of energy loss depends on the angle of deflection and initial energy of the incident photon. This amount

equals the binding energy plus the kinetic energy with which the electron leaves the atom. For an incident photon energy E , the scattered photon energy E' is given by [20]:

$$E' = \frac{E}{1 + \frac{E}{m_e c^2} (1 - \cos \theta)} \quad (2.2)$$

where

m_e is the rest mass of the electron

c is the speed of light in free space

θ is the scattering angle

If E is lower than $m_e c^2$ (rest energy of an electron, which is 511 keV), then E' is roughly independent of θ . If E is higher than $m_e c^2$, then E' is higher for small θ . Scattered photons with higher energies will continue in approximately the same direction as most of the energy is retained by the photon after a Compton scattering. Thus scattered photon interact many times with the matter before it losses all of its energy. It is worth noting here that, Equation (2.2) is valid only if the electron was free, i.e. we can neglect the original binding energy.

Unlike photoelectric effect, the probability of occurrence of Compton scattering does not depend on the atomic number of the material but instead on the electronic density of the material. Figure 2.6 shows, for example, the percentage of the above three different types of interactions of X-rays with matter as a function of energy in water [2].

2.3.4 Pair Production

Pair production is a form of interaction of X-ray with matter characterized by photon-nucleus interaction. If the incident X-ray photon has sufficiently large amount of energy (>1.02 MeV),

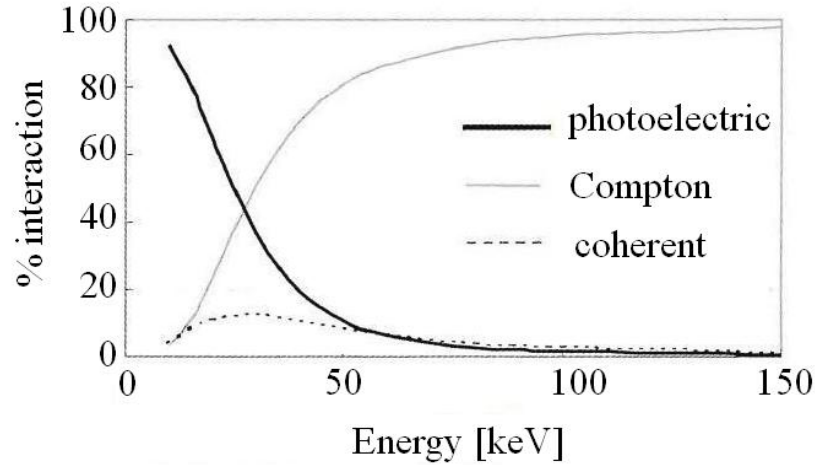


Figure 2.6: Percentage of different types of interactions as a function of energy in water [2]

it may escape the electron cloud and come close enough to the nucleus to experience the strong electrostatic field of the nucleus. This strong electrostatic field causes the nucleus to absorb the high-energy photon and emit a pair of charged particles: a *positron* (positively charged) along with an *electron* (negatively charged). This mechanism is illustrated in Figure 2.7 and describes antimatter formation used in Positron Emission Tomography (PET) imaging.

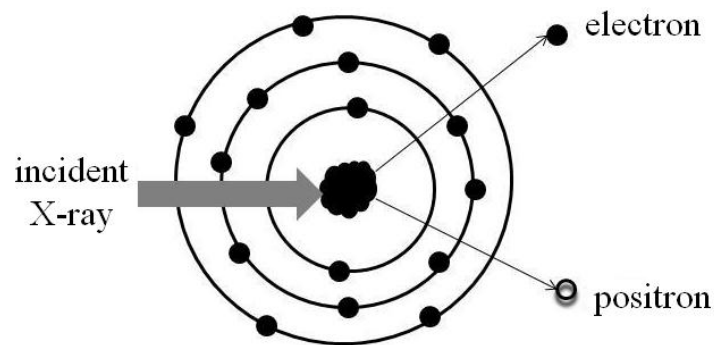


Figure 2.7: Illustration of pair production mechanism

2.3.5 Photodisintegration

When the energy of the incident X-ray photon exceeds 8 MeV, the photon can escape interaction with both the electrons and the strong electrostatic fields of the nucleus and gets absorbed directly by the nucleus of the atom. This absorption excites the nucleus which results in one or more particles being ejected and the transformation of one element to the other. Figure 2.8 illustrates the process of photodisintegration.

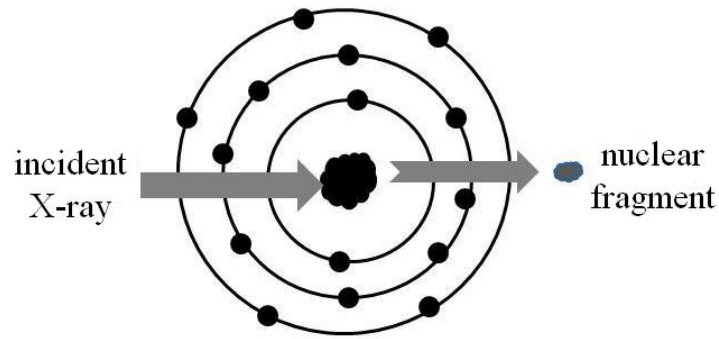


Figure 2.8: Illustration of photodisintegration mechanism

2.4 X-ray Detectors

An X-ray photon, after going through and interacting with matter is detected by an X-ray detector. X-ray detectors are very important part of an imaging system as they determine the quality of an X-ray image. There are several different types of X-ray detector technology available. No single type of X-ray detector is best for all applications. The choice of an X-ray detector largely depends on the application at hand and on several other factors, namely: the size of the object to be imaged, how fast we want to image the object, the material of which the object is made, the level of details we want to see in the image, imaging technique, the X-ray source parameters, etc.

2.4.1 X-ray Photographic Plates, Films and Fluoroscopy

Photographic plates were used at the early stage of radiography to produce most radiographic images before the coming of digital computer and the birth of digital imaging. These plates, made of glass were sensitive to X-rays and were able to convert the X-ray pulses into images with the main drawback being their weight and longer exposure time needed to detect the image. These photographic plates were later replaced by thinner and easier-to-use X-ray films which are essentially baryta paper coated with silver nitrate. Molecules of this silver nitrate coating detect and absorb the incident X-ray photons, and convert them into images. Though this process still requires some exposure, the exposure time and intensity is less than for photographic plates. Due to the fact that silver is considered as a non-renewable resource, fluorescent chemicals are instead used to detect and absorb light given off by X-rays in a process called *fluoroscopy*. The formation of an image is a result of the chemical reaction that takes place when the fluorescent screen absorbs the light.

However, with the advent of digital computers, the above traditional X-ray detectors were replaced by digital X-ray sensors in X-ray digital radiography which offers the potential of improved image quality. Advantages of this form of radiography include: fastness, easiness to transfer data to the computer and storage of data in digital form for later use, better image quality and less radiation exposure than conventional radiography. The function of any X-ray detector can fundamentally be outlined in the following steps:

1. X-ray photons are absorbed
2. The absorbed energy is converted to a usable signal, generally light or electric charge

3. This usable signal is collected
4. In the case of phosphor-based detectors, light signal is converted to electrical signal
5. The electrical signal is readout, amplified and digitized

For the detectors to provide high-quality images at appropriate dosage levels, the steps outlined above must be optimized since several detector parameters can affect image quality. These parameters include field coverage, geometrical characteristics, quantum efficiency, sensitivity, spatial resolution, noise characteristics, dynamic range, uniformity, acquisition, frame rate [22].

2.4.2 Flat Panel Detectors

Flat panel detectors are usually amorphous silicon (a-Si) or amorphous selenium (a-Se). The former requires scintillators while the later can be used as an intrinsic detector.

2.4.2.1 Amorphous Silicon Flat Panel Detectors

Amorphous Silicon FPD is the most frequent type of FPD in use today. It is based on an indirect detection of X-rays as illustrated in Figure 2.9 [23]. The scintillators or phosphors absorb X-ray photons, convert their energy to light photons emission and channel the light photons towards the a-Si photodiode array. Each photodiode represents a pixel. The low-noise photodiode after absorbing the light converts it to electrical signal. The low-noise readout electronics reads out the charge at each pixel and send it to the computer for processing.

The scintillator is made up of Caesium Iodide (CsI) or Gadolinium Oxysulphide ($\text{Gd}_2\text{O}_2\text{S}$ also called *GADOX*) materials. These are crystalline semiconductor materials doped with impurities to create intermediate energy levels in the forbidden gap between the valence and conduction bands as illustrated in Figure 2.10.

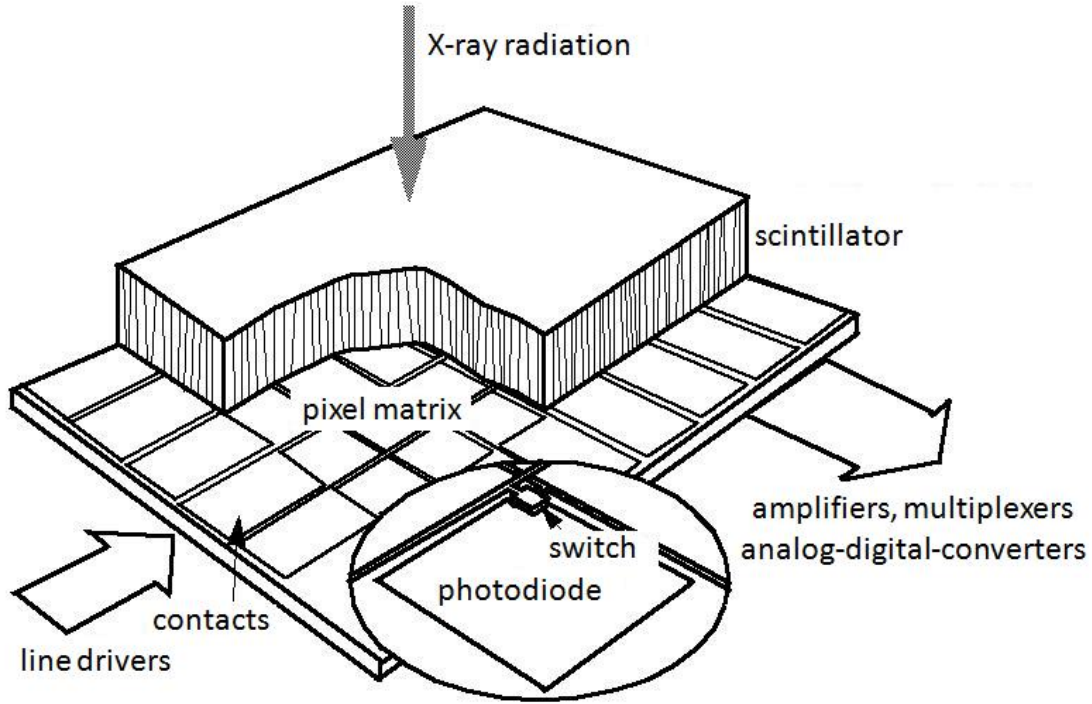


Figure 2.9: Schematic drawing of a-Si FPD [23]

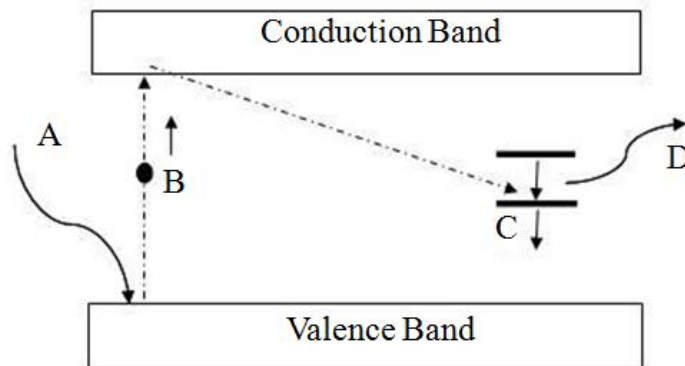


Figure 2.10: Principle of operation of Indirect X-ray detector

As shown in Figure 2.10, X-rays photons upon incidence on the material (A) excite electrons in the conduction band (B) and these excited electrons are captured by the impurities center (C) and rapidly released to the valence band there releasing some energy in the form of light (D). The choice of the impurities levels are made such that the difference in energy between these levels and the valence band ΔE should give radiation in the visible spectrum, whose wavelength λ is given,

following Equation 2.1, by:

$$\lambda = \frac{hc}{\Delta E} \quad (2.3)$$

where

h is Planck's constant

c is the speed of light in free space

The phosphor *GADOX*, which has become the standard for phosphor-based detection, absorbs and emits visible photons predominantly at 545 nm (2.28 eV) with approximately a conversion efficiency of 15 %. That is, the number of visible photons N emitted per absorbed X-ray photon of energy E (eV) will be given by:

$$N = \frac{E \times 0.15}{2.28} \quad (2.4)$$

Due to the inherent scattering in the phosphor itself, the process of absorption-emission is a noisy one both in terms of intensity and spatial distribution. Figure 2.11 is a photograph of an a-Si FPD of field size 24 x 30 cm and 14-bit digitization produced by General Electric Medical Systems (Milwaukee, WI) [24].

The major advantages of flat panel detectors are that they are fast, very sensitive and have a simple assembly. However they have a major disadvantage in their limited dynamic range which is further reduced by crosstalk and scattering. This indirect FPD has additional advantages over direct FPD which include: increased dynamic range especially at higher photon energies due to the fact that fewer photoelectrons are produced in the device per each X-ray photon detected; also the extra phosphor coating can be tailored to suit any applications providing wide range of usability and also protecting the a-Si photodiodes from the X-ray radiation.



Figure 2.11: Photograph of an a-Si Flat Panel Detector [24]

2.4.2.2 Amorphous Selenium Flat Panel Detectors

Unlike a-Si FPD, a-Se FPD are direct detectors because X-rays photons are converted to electrical charge directly. The design of an a-Se FPD has a high-voltage bias electrode on the outer layer followed by thin layer (100-200 μm) as shown in Figure 2.12 [25].

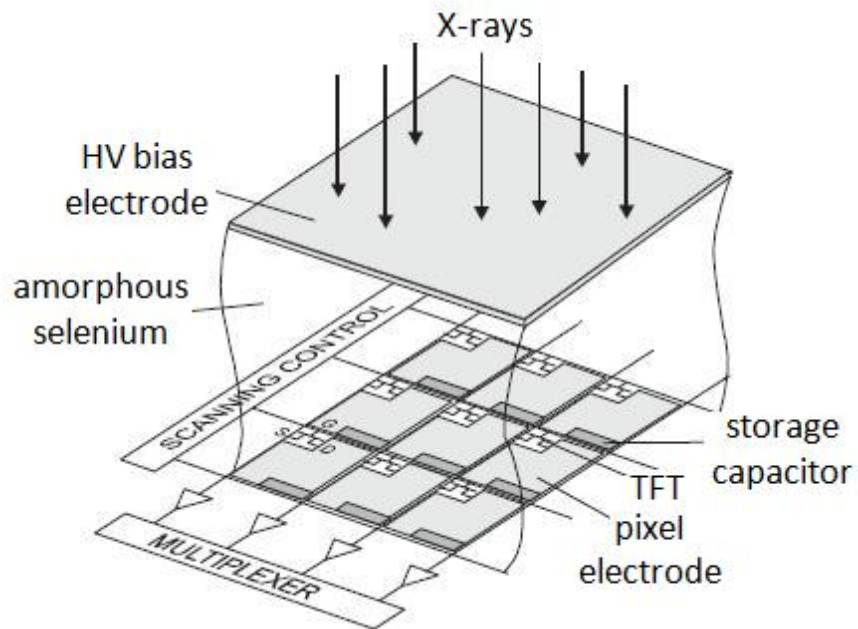


Figure 2.12: Schematic diagram showing concept of a-Se FPD [25]

When exposed to X-rays, the captured X-ray photons are accelerated through the amorphous selenium layer by the bias electrode, interacting with selenium and producing energetic photoelectrons. The X-ray photons lose their kinetic energy through multiple interactions with outer-shell electrons of the selenium atoms, releasing these electrons and leaving behind corresponding holes. The number N of electron-hole pairs formed is given by:

$$N = \frac{E}{\varepsilon_i} \quad (2.5)$$

where

E is the absorbed energy

ε_i is the bandgap energy of the element of the material

The electron-hole pair constitutes a usable signal and is separated by an internal electric field and subsequently read-out electronically by a 2-D array of thin film transistors (TFTs). The TFTs are switched *on* and *off* one row at a time by the pulses generated by the scanning control circuit and the image charge is transferred from the pixel to external charge sensitive amplifiers subsequently to the computer for processing.

Chapter 3

X-ray Computed Tomography

3.1 Introduction to X-ray Computed Tomography

X-ray computed tomography (CT) is the non-destructive visualization of the internal structure of objects using information of the interaction of X-rays with the object in question, particularly the attenuation information. The X-ray beam produced by the X-ray source in the CT scanner can be *parallel* or *fan-shaped* depending on the scanner. Figure 3.1 illustrates the basic principles of X-ray CT using fan-beam geometry [26].

In Fan-beam X-ray CT as shown in Figure 3.1, a cross-section of the beam generated by the X-ray source is shaped by a collimator to produce a fan-beam and transmitted through the sample. The attenuated X-ray data after passing through the sample is collected by a detector array. The sample is rotated at regular angular intervals over a complete range $[0^\circ - 360^\circ]$ to collect projection data from different directions which are used to reconstruct a cross-sectional slice of the sample.

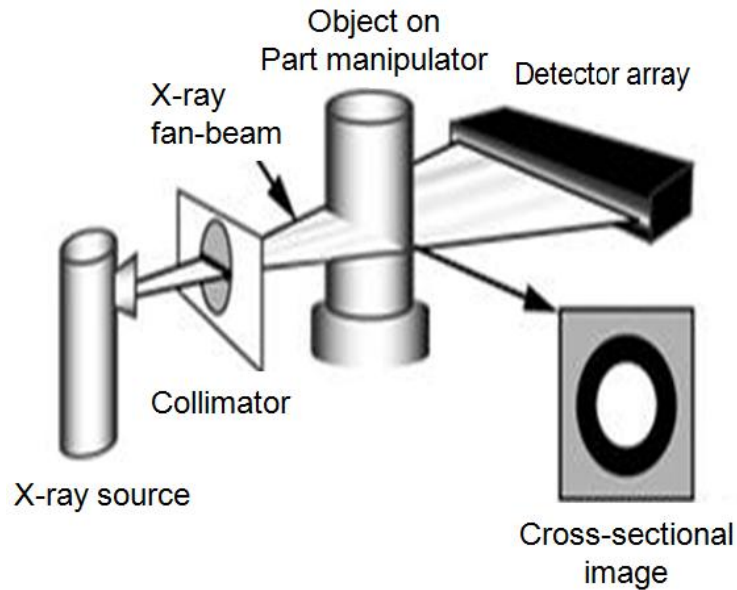


Figure 3.1: Principles of Fan-beam X-ray Computed Tomography [26]

3.2 Applications of X-ray Computed Tomography

X-ray CT has numerous industrial and biomedical applications. In industrial applications, resolution is important and some of these applications include:

- Research - Material Structure, New Material Analysis
- Non-destructive testing or Inspections of materials - Inclusions, Cracks, Porosities, Displacement, Quality Control
- Aviation - aircraft wings and other parts
- Reverse Engineering - Rapid Prototyping, Surface Rendering, CAD, Drawing and Design
- Measurements and Meterology
- Assembly analysis

In biomedical applications, low attenuating tissues are being imaged. In these types of application contrast is very important. This is to be able to distinguish between tissues which are very close in attenuation of the X-rays. Biomedical applications of X-ray CT include:

- Head CT
- Cardiac CT
- CT of the lungs
- Abdominal and pelvic CT

3.3 Radon Transform and the Fourier Slice Theorem

Given a two-dimensional function $f(x, y)$ in Figure 3.2 [27], the line integral of $f(x, y)$ along a straight line inclined at an angle θ to the x -axis is given as [28]:

$$p(s, \theta) = \int_{(\theta, s) \text{ line}} f(x, y) du \quad (3.1)$$

Equation (3.1) can be rewritten using delta function as:

$$p(s, \theta) = \int_{-\infty}^{\infty} \int_{-\infty}^{\infty} f(x, y) \delta(x \cos \theta + y \sin \theta - s) dx dy \quad (3.2)$$

The function, $p(s, \theta)$ is called the *Radon Transform* of $f(x, y)$ and represents an analytic transform for that object. A set of line integrals combine to form a projection, with the simplest projection being a collection of parallel ray integrals as given by $p(s, \theta)$ in Equations (3.1) and (3.2) for a constant θ .

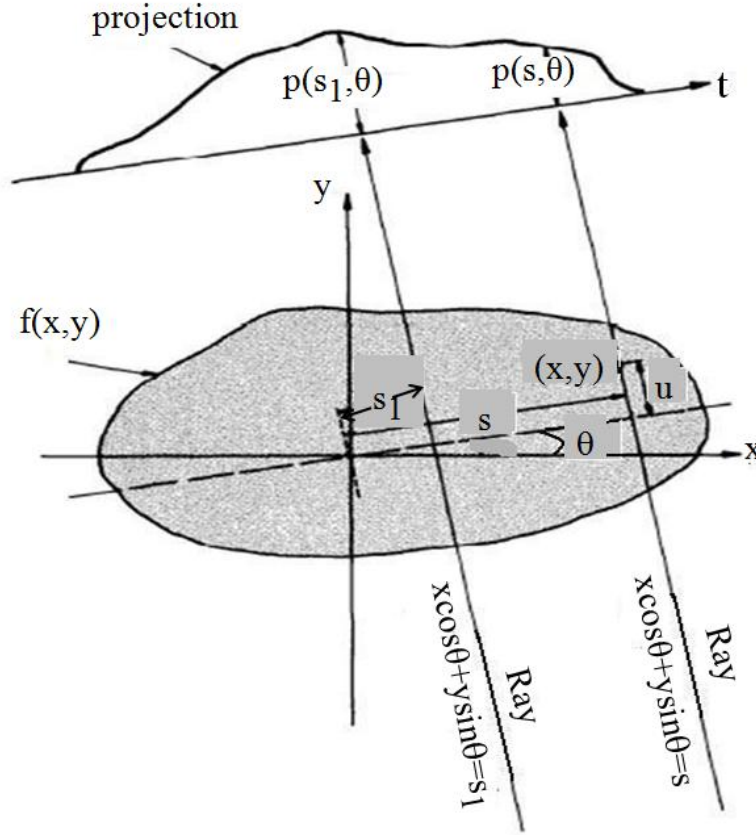


Figure 3.2: An object, $f(x,y)$, and its object, $P(s_1, \theta)$ are shown for an angle of θ [27]

The Fourier Slice theorem is presented here following the derivation given in [28]. Given an object function $f(x, y)$, the two-dimensional Fourier transform (FT) of $f(x, y)$ is given as:

$$F(k_x, k_y) = \int_{-\infty}^{\infty} \int_{-\infty}^{\infty} f(x, y) e^{-j2\pi(k_x x + k_y y)} dx dy \quad (3.3)$$

Given a projection $p(s, \theta)$, its Fourier transform is given by:

$$P(\omega, \theta) = \int_{-\infty}^{\infty} p(s, \theta) e^{-j2\pi\omega s} ds \quad (3.4)$$

For simplicity $\theta = 0^\circ$ which leads to $k_y = 0$, the Fourier transform of Equation (3.3) simplifies

to:

$$F(k_x, 0) = \int_{-\infty}^{\infty} \int_{-\infty}^{\infty} f(x, y) e^{-j2\pi k_x x} dx dy \quad (3.5)$$

Since the phase factor of the integrand in Equation (3.5) no longer depends on y , rearranging the integral gives:

$$F(k_x, 0) = \int_{-\infty}^{\infty} \left[\int_{-\infty}^{\infty} f(x, y) dy \right] e^{-j2\pi k_x x} dx \quad (3.6)$$

The integral in brackets of Equation (3.6) is effectively the equation for a projection along lines of constant x :

$$p_{\theta=0}(x) = \int_{-\infty}^{\infty} f(x, y) dy \quad (3.7)$$

Substituting Equation (3.7) into Equation (3.6), we get:

$$F(k_x, 0) = \int_{-\infty}^{\infty} p_{\theta=0}(x) e^{-j2\pi k_x x} dx \quad (3.8)$$

The right hand side of Equation (3.8) represents the one-dimensional Fourier transform of the projection $p_{\theta=0}$; thus giving the following relationship between the vertical projection and the 2-D transform of the object function:

$$F(k_x, 0) = P_{\theta=0}(k_x) \quad (3.9)$$

i.e. the line along $k_y = 0$ in the 2-D FT = the FT of the projection at $\theta = 0^\circ$. This is the simplest form of the Fourier Slice Theorem but is clearly independent of the orientation between the object and the coordinate system. Hence it is easily generalized by using the rotated co-ordinate system

(s, u) :

$$\begin{bmatrix} s \\ u \end{bmatrix} = \begin{bmatrix} \cos \theta & \sin \theta \\ -\sin \theta & \cos \theta \end{bmatrix} \begin{bmatrix} x \\ y \end{bmatrix} \quad (3.10)$$

The Fourier Slice Theorem states that the 1-D Fourier Transform of a projection taken at an angle θ equals the central radial slice at angle θ of the 2-D Fourier Transform of the original object. This theorem makes it possible to reconstruct the original object by simply performing the 2-D inverse Fourier Transform as depicted in Figure 3.3 and has been shown to be extremely accurate [28, 29].

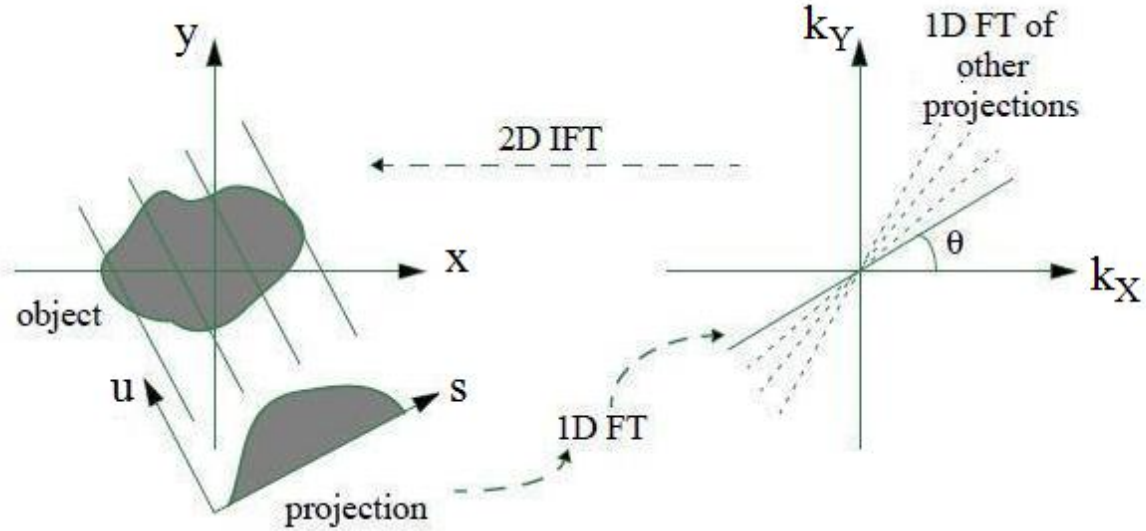


Figure 3.3: The Fourier Slice Theorem relates the Fourier transform of a projection to the Fourier transform of the object along a radial line

3.4 Image Reconstruction by Filtered Backprojection Algorithm

Image reconstruction from X-ray projections is usually performed using the classical Filtered-Back Projection (FBP) algorithm. This algorithm is based on Radon transform and the Fourier slice theorem, assuming ideal conditions such as monochromatic X-ray beam and infinite number

of projections. According to Beer-Lambert's law, the transmitted intensity I of a monochromatic beam of photons of incident intensity I_0 as it passes through a material with spatial distribution of attenuation coefficient $\mu(x, y)$ at the point (x, y) can be expressed as [1]:

$$I = I_0 e^{-\int_L \mu(x, y) du} \quad (3.11)$$

where L is the path of the ray and u is the length along L . By measuring the natural logarithm of the intensity ratio at different sensor positions s on the detector array and several source locations θ , we obtain:

$$P(s, \theta) = \ln \left(\frac{I_0}{I} \right) = \int_L \mu(x, y) du \quad (3.12)$$

Equation (3.12) is the projection or Radon Transform of μ at an angle θ . Therefore, the inversion of the transform in Equation (3.12) gives a direct solution to the reconstruction problem as [21, 28]:

$$\hat{\mu}(x, y) = \underbrace{\int_0^\pi \underbrace{\int_{-\infty}^\infty \underbrace{P(\omega, \theta)|\omega|}_{\text{filtering}} e^{j2\pi\omega(x \cos \theta + y \sin \theta)} d\omega}_{\text{inverse Fourier transform}} d\theta}_{\text{Backprojection}} \quad (3.13)$$

where in Equation (3.13) $P(\omega, \theta)|\omega|$ is the filtering process of the projections, the inner integral (over ω) is the inverse Fourier Transform of the filtered projections $P(\omega, \theta)|\omega|$ and the outer integral is the backprojection. The entire reconstruction process can be summarized in Figure 3.4.

3.5 Artifacts in X-ray Computed Tomographic Images

Artifacts in X-ray computed tomographic (CT) reconstructed images generally refer to any systematic discrepancy between the reconstructed value and the true attenuation coefficients of the

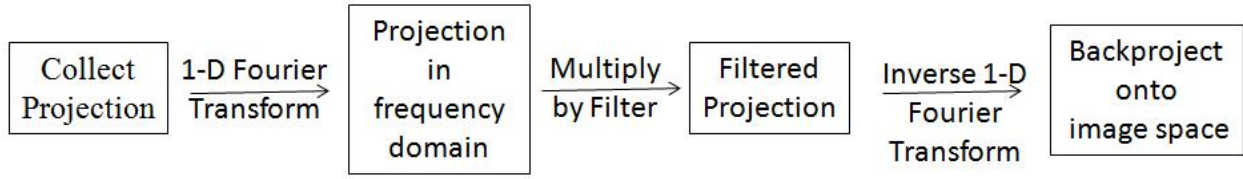


Figure 3.4: Steps involved in Filtered-Backprojection Reconstruction Algorithm

object. Artifacts can seriously degrade the quality of CT images, at times making them diagnostically unusable. CT images often have these artifacts because they are reconstructed from million of detector measurements and the reconstruction algorithms always assume that these measurements are consistent. So any discrepancy in the measurement will reflect as a discrepancy in the reconstructed image. The types of artifacts generally encountered in CT images are: *streaking artifacts* which are intense straight but not necessarily parallel lines across the image and caused by inconsistency in a single measurement; *shading artifacts* which appear near objects of high contrasts and are due to some projection measurements deviating gradually from the true measurements; *ring artifacts* which appear as rings in the reconstructed image and are due to an individual detector error over all projections; artifacts due to limited number of projections as a result of insufficiently filled Radon space.

Also based on their origin, these artifacts can be grouped in the following categories: *physics-based artifacts*, which are brought about by the physical processes involved in the CT data acquisition, *patient-based artifacts*, which are caused by factors such as patient movement or the presence of metallic materials in the patient, *scanner-based artifacts*, which results from the imperfection of scanner function. Of all the aforementioned artifacts, the physics-based artifacts due to beam hardening and limited number of projections are of interest in this thesis. These artifacts are addressed in subsequent chapters.

Chapter 4

A Model-based Correction Scheme for Beam Hardening in X-ray Computed Tomography

4.1 Proposed Model-Based Correction Scheme

Beam hardening (BH), as discussed in Section 1.1, is an undesirable effect which results in artifacts in images reconstructed using Filtered Back Projection (FBP) algorithm. FBP, based on Radon Theory and the Fourier Slice Theorem, assumes the X-ray source to be monochromatic though polychromatic. In Section 1.1, several existing techniques for correcting BH artifacts were introduced. In this thesis we propose a novel model-based correction scheme for BH based on the Lambert-Beer's law for polychromatic X-rays, knowledge of source spectrum and CAD model of the specimen. The proposed correction scheme is summarized in Figure 4.1 and explained below [14].

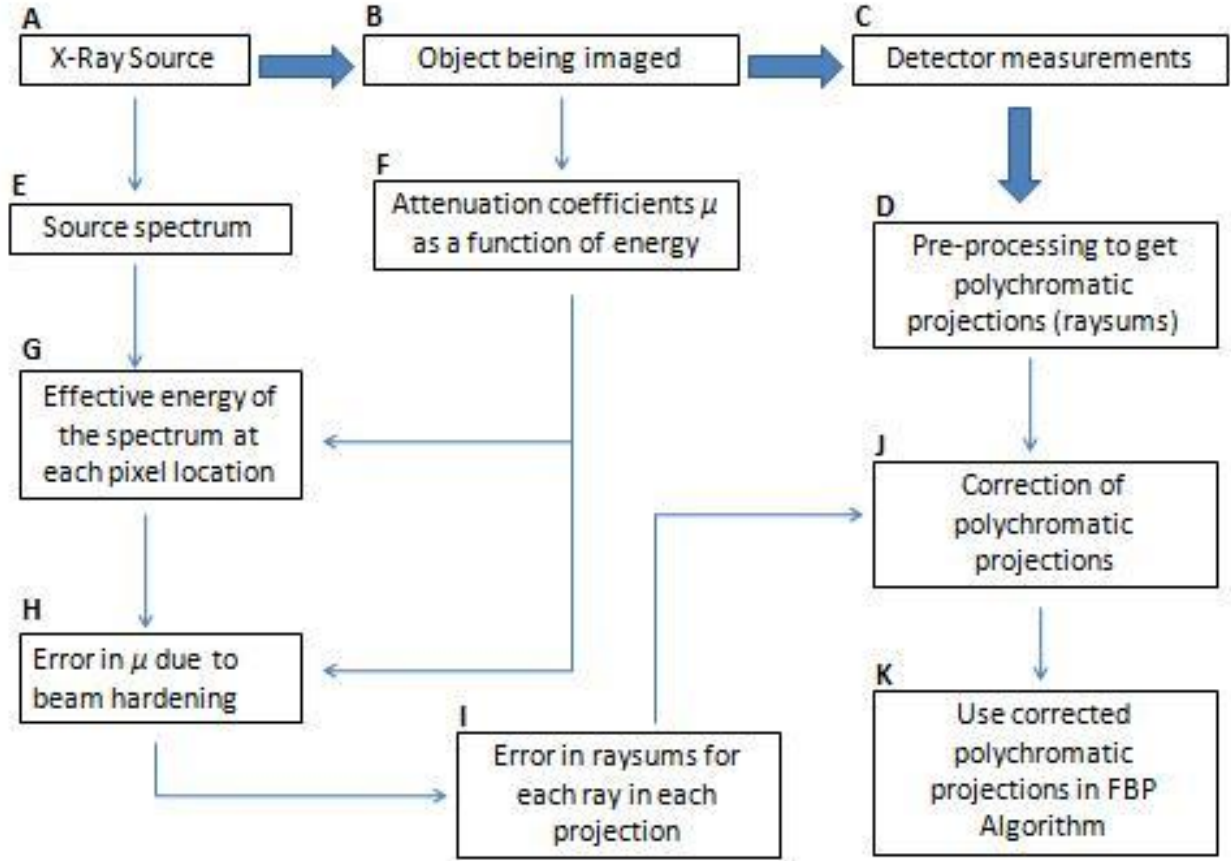


Figure 4.1: An Overview of the Correction Technique for reducing BH effects

The steps in boxes *A* to *D* of Figure 4.1 describe the standard procedure to acquire X-ray projection data. This projection data is then used to reconstruct the object. The novelty of the proposed technique is the introduction of additional steps described by steps *E* through *K*.

Consider an object with two dimensional spatial distribution of mass attenuation coefficient $\mu(x, y)$. Figure 4.2 shows the coordinate transformation from spatial domain (x, y) to the projection domain (s, θ) [28].

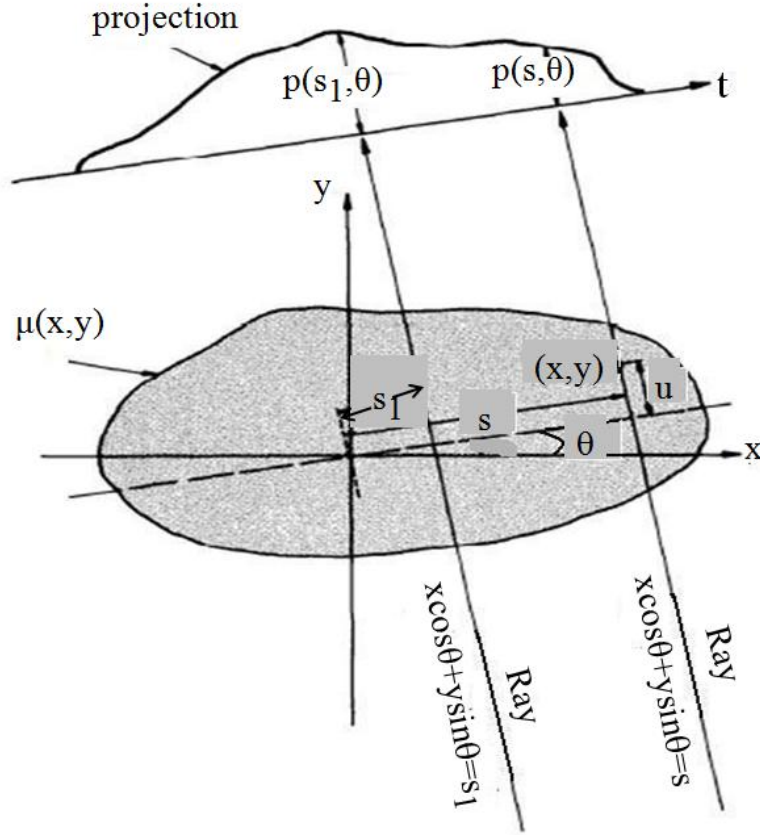


Figure 4.2: Coordinate Transformation from (x, y) to (s, θ) [28]

The forward propagation model is based on polychromatic Lambert-Beer's law described mathematically as [2]:

$$I = I_0 \int \Omega(E) e^{-\int_L \mu(x, y, E) du} dE \quad (4.1)$$

where $\Omega(E)$ is the incident spectrum acquired from the X-ray source (step E) and $\mu(x, y)$ is the energy dependent model of the object (step F). Describing an X-ray spectrum in terms of *quality* (the energy E of the photons) and *quantity* (the number of photons $N = I$ with energy E), its

effective energy E_{eff} at each pixel location (x, y) is computed as (step G):

$$E_{eff}(x, y) = \frac{\sum_{e=1}^{e=E_{max}} N_e \cdot E_e}{\sum_{e=1}^{e=E_{max}} N_e} \quad (4.2)$$

At a particular pixel (x, y) error in μ values due to beam hardening is given as (step H):

$$\Delta\mu(x, y) = \mu(x, y, E_0) - \mu(x, y, E_{pixel}(x, y)) \quad (4.3)$$

where E_0 and E_{pixel} are the effective spectrum energies of the calibration scan (no object) and at each pixel location (with the object present) respectively, computed using Equation (4.2). Figure 4.3 below shows a spectral plot of mass attenuation coefficient of tungsten up to 300 keV. The effective energy of the calibration scan of this spectrum, E_0 is 120 keV. The pixel is located at the center of the object where due to beam hardening, the effective energy, E_{eff} of the spectrum at this point is 265 keV. This shift in the effective energy due to beam hardening corresponds to $\Delta\mu = 0.5480 \text{ cm}^2/\text{g}$ at that pixel location as given by Equation (4.3).

For a particular ray s in each projection θ , the cumulative error in μ values at all pixels traversed by that ray (error in raysums) is given as (step I):

$$\Delta P(s, \theta) = \sum_{x, y} \Delta\mu(x, y) \delta(x \cos \theta + y \sin \theta - s) \quad (4.4)$$

where $s = x \cos \theta + y \sin \theta$ is the equation of the line defining the ray path as shown in Figure 4.2.

For a given BH polychromatic projection $P_{poly}(s, \theta)$ obtained from the detector measure-

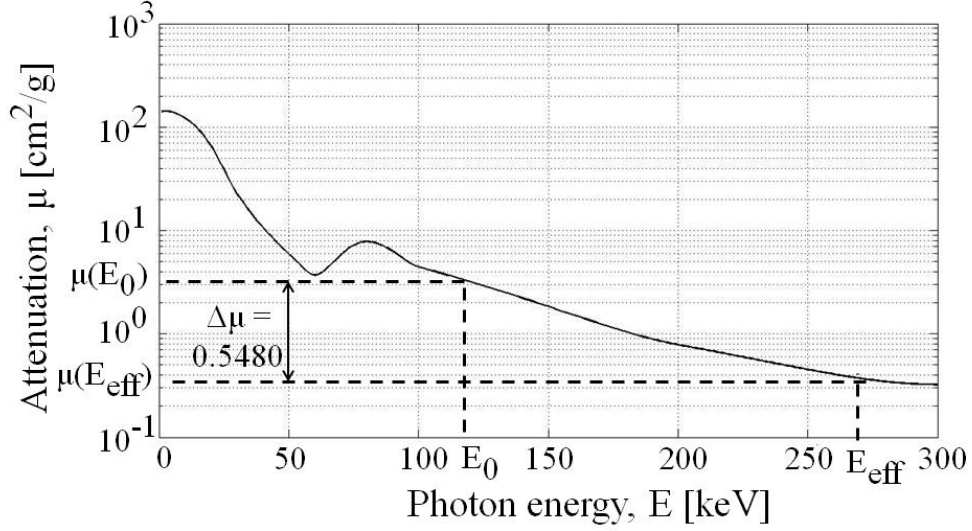


Figure 4.3: Spectral Plot of Mass Attenuation Coefficients of Tungsten up to 300 keV

ments, a corrected projection $P_{corr}(s, \theta)$ is computed as (step J):

$$P_{corr}(s, \theta) = P_{poly}(s, \theta) + \Delta P(s, \theta) \quad (4.5)$$

In step K , the object is reconstructed from the corrected polychromatic projection using FBP algorithm.

4.2 Results with Simulation Data

To demonstrate the validity of the technique proposed in Section 4.1, a uniform circular phantom was simulated using attenuation coefficients values of tungsten obtained from the National Institute of Science and Technology (NIST) database [30] for photon energies up to 320 keV. X-ray polychromatic projections were then obtained from the simulated phantom in an $M \times N$ imaging space. The following step-wise procedure is used for obtaining all projection angles:

1. Let the rows be represented by $i = 1 : M$ and the columns, by $j = 1 : N$

2. Set the incident intensity at the first row $i = 1$ to a reference value of 65536 which corresponds to the 16-bit dynamic range of the detector used in the experimental work
3. For rows $i = 2 : M$ and at the j^{th} column, the polychromatic transmitted beam $I(i, j, E)$ through a particular pixel (i, j) follows from Equation (4.1) as:

$$I(i, j, E) = I(i - 1, j, E) e^{-\mu(i, j, E)} \quad (4.6)$$

4. The raysum (Rsm) corresponding to column j on exiting the imaging space at the last row $i = M$, will be given be as:

$$Rsm(j) = -\ln \left(\frac{I(M, j, E)}{I(1, j, E)} \right) \quad (4.7)$$

5. The BH sinogram is obtained by repeating steps 1 to 4 for different projection angles

The BH projections are corrected using the steps outlined in Equations (4.1) to (4.5) above. Figure 4.4 shows the BH polychromatic projection data for the case of $\theta = 0^\circ$. Also shown for comparison are the ideal (monochromatic) projection and the corrected polychromatic projection.

Reconstructions from these projection data were performed by applying the FBP algorithm using 180 projections with 194 rays per projection. Figure 4.5 shows the 134×134 CT reconstructed images from the BH polychromatic projections before and after correction.

Figure 4.6 are horizontal line profiles taken through the middle part of the CT reconstructed images, from where the cupping effect due to BH can be observed.

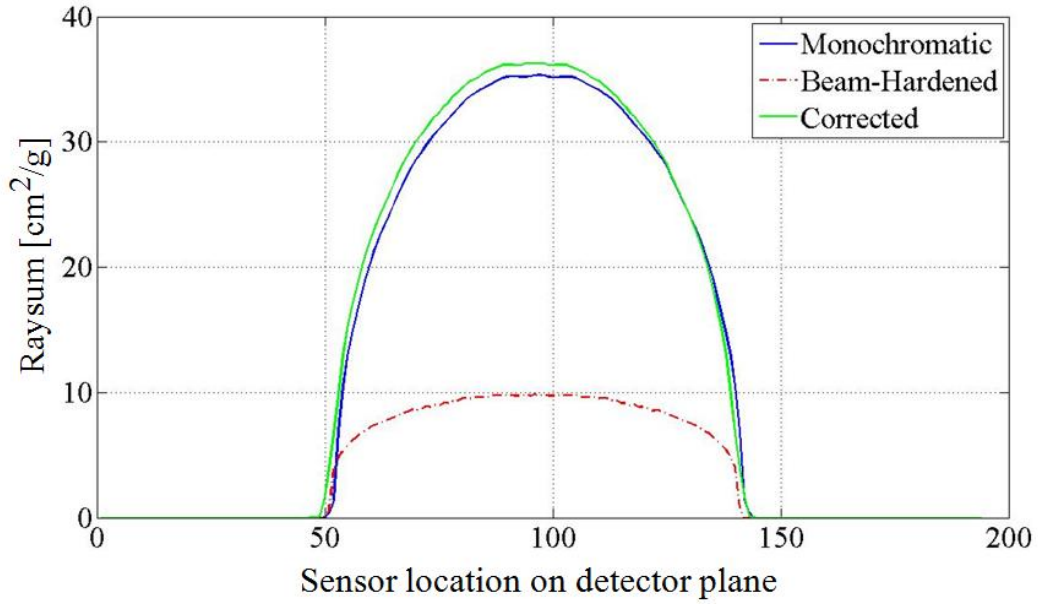


Figure 4.4: Comparison of projection data

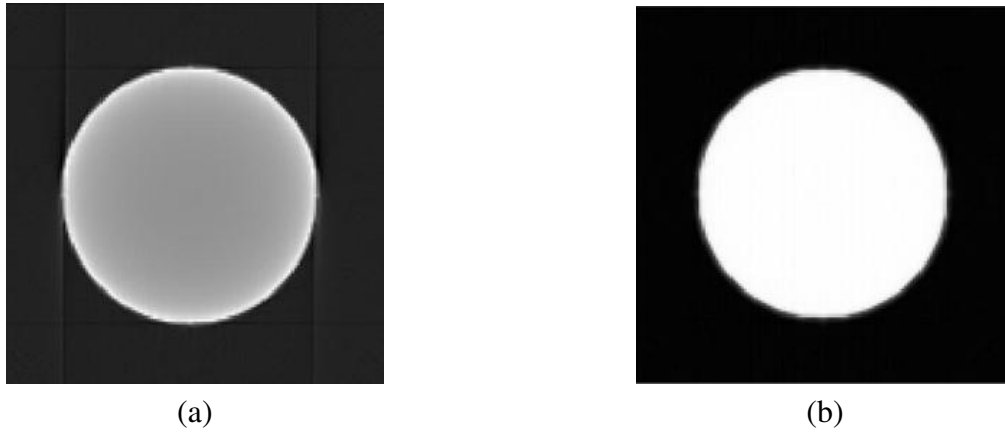


Figure 4.5: CT reconstructed images [14]: (a) Before correction (b) After correction

The effect of beam-hardening in non-destructive evaluation of an object was investigated by introducing 3 very low contrast circular defects in the simulated uniform circular phantom shown in Figure 4.7.

Figure 4.8 shows the FBP reconstructed results using 180 projections with 194 rays per projection; where as a result of beam-hardening, the defects are not clearly visible in Figure 4.8a.

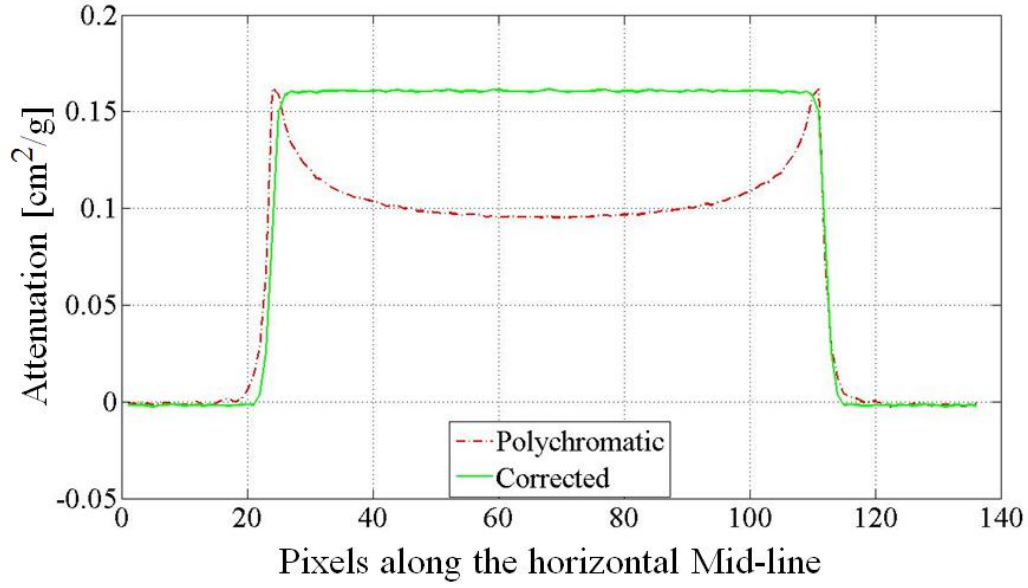


Figure 4.6: CT reconstructed attenuation values showing cupping artifact

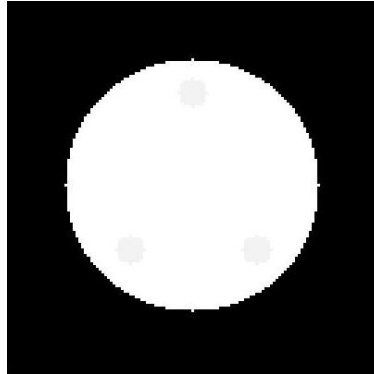


Figure 4.7: Phantom with Defects

However, after applying the proposed correction scheme, the beam hardened CT reconstructed image is greatly improved thus revealing the low contrast defects as seen in Figure 4.8b.

4.3 Results with Experimental Data

The validity of the proposed technique was further tested using experimental projection data. The sample used in the experiment was a 12" rod of heavy tungsten alloy 18.5 (18.5 refers to the

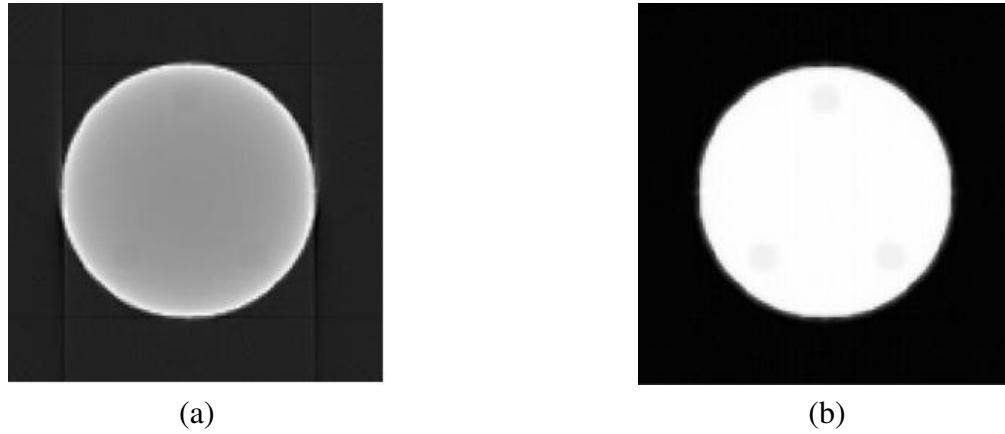


Figure 4.8: CT reconstructed images with defects [14]: (a) Before correction (b) After correction

density of the alloy in g/cm^3). This alloy is made up of 97 % Tungsten, 2.1 % Nickel and 0.9 % Iron. The diameter of the rod is 0.375 ". Figure 4.9 below shows the experimental set-up where an X-ray source of 320 kV_p and 10mA was used together with a photostimulable phosphor detector of spatial resolution of 500 μm . The Source-to-detector distance and the focal spot were 60 " and 4.0 mm respectively.

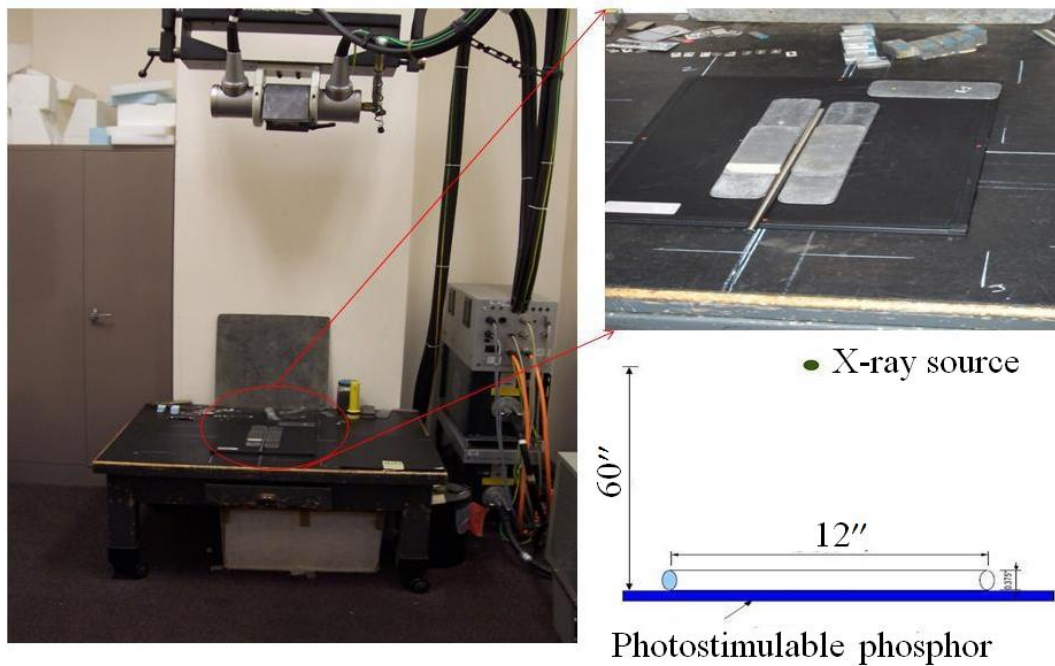


Figure 4.9: Experimental set-up

Projection data (raysums) of the tungsten rod sample were acquired at different angles by rotating the cylindrical tungsten sample. Figure 4.10 below shows an acquired 0° polychromatic projection data after calibration and log-processing.

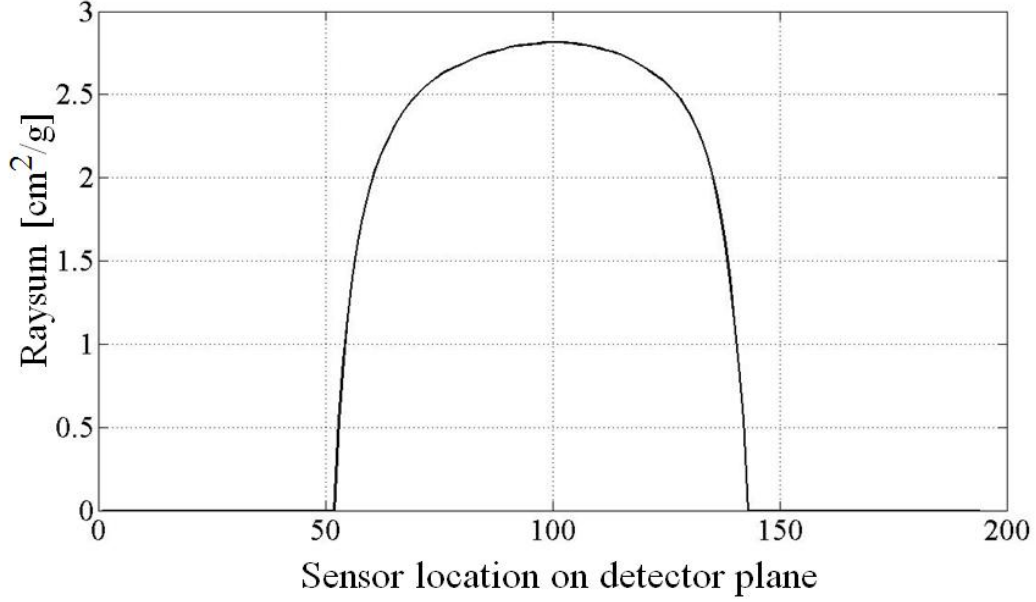


Figure 4.10: Experimental projection data

The proposed correction scheme was then applied to the experimental data following the steps outlined in Section 4.1, Equations (4.1) to (4.5). The reconstructed CT images from the experimental projection data are given in Figure 4.11 before and after correction.

To further evaluate the proposed correction scheme, two quantitative metrics of the CT reconstructed images are used namely: *Mean-Square-Error* (MSE) and *Peak Signal-to-Noise Ratio* (PSNR). Let $\hat{\mu}(i, j)$ be the reconstructed $M \times N$ image and $\mu(i, j)$ represent the corresponding true image. The metrics MSE and PSNR are computed respectively as [31]:

$$MSE = \frac{1}{MN} \sum_{i=0}^{M-1} \sum_{j=0}^{N-1} \left[|\mu(i, j) - \hat{\mu}(i, j)|^2 \right] \quad (4.8)$$



Figure 4.11: Experimental CT reconstructed images [14]: (a) Before correction (b) After correction

$$PSNR = 10 \log \left(\frac{(255)^2}{MSE} \right) \quad (4.9)$$

Table 4.1 shows the results for the MSE and PSNR of both the beam-hardened CT reconstructed image and the CT image reconstructed using the proposed correction scheme of Figure 4.1.

Table 4.1: Quantitative Measures

CT Image	MSE	PSNR [dB]
Beam-hardened	0.0011	77.72
Corrected	0.0003	83.35

As evident from the table, there is an improvement in both the MSE and PSNR when the correction scheme is applied.

4.4 Parametric Study

4.4.1 Cupping Artifact as a Function of Source Energy

A systematic study of the beam hardening phenomenon as a function of the peak voltage of the X-ray source was performed. Cupping artifact was simulated at 100 keV, 200 keV and 300 keV

using the procedure outlined in Section 4.2. Figure 4.12 are horizontal line profiles taken through the middle part of the respective CT reconstructed images, from where the cupping effect due to BH can be observed to increase with peak energy of the X-ray source.

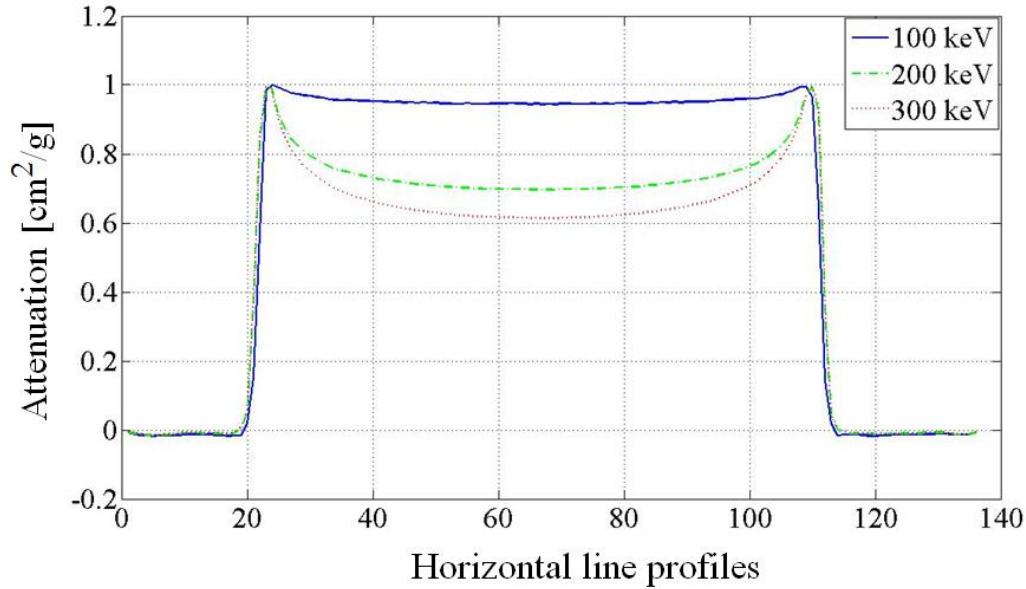
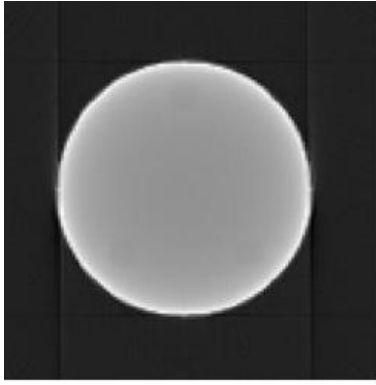


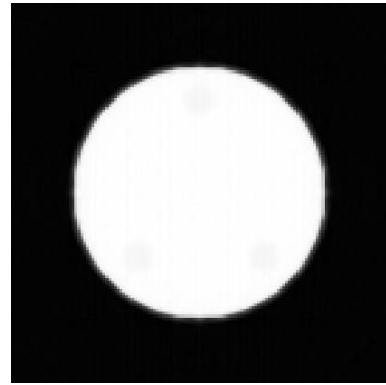
Figure 4.12: CT reconstructed attenuation values showing cupping artifact at 100 keV, 200 keV and 300 keV

4.4.2 Performance of Correction Scheme at Different Contrasts

In X-ray CT, the ability to detect very small low contrast defects is very important. Depending on the applications, contrast will be the primary concern as in biomedical imaging. In the non-destructive evaluation of a material, the size of the defect is critical. The performance of the proposed correction scheme was evaluated using the phantom with defects of Figure 4.7. The evaluation was done for 5%, 10% and 15% contrast between the defects and host material at 300 keV. CT reconstructed images before and after correction are shown in Figures 4.13, 4.14, and 4.15 for contrast levels of 5%, 10% and 15% respectively.

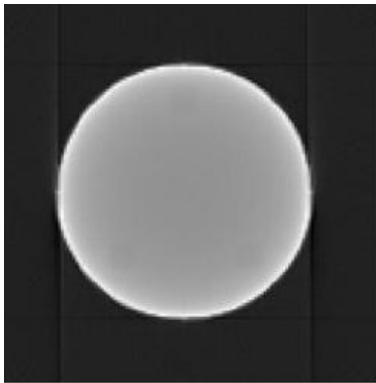


(a)

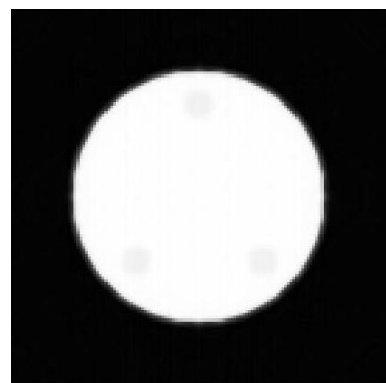


(b)

Figure 4.13: CT reconstructed images with 5 % defects: (a) Before correction (b) After correction



(a)

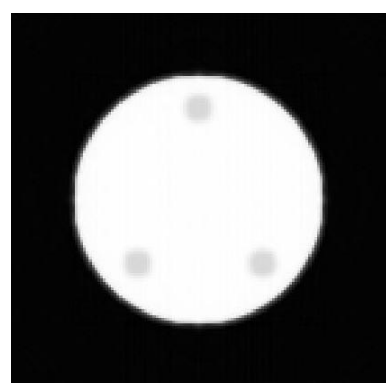


(b)

Figure 4.14: CT reconstructed images with 10 % defects: (a) Before correction (b) After correction



(a)



(b)

Figure 4.15: CT reconstructed images with 15 % defects: (a) Before correction (b) After correction

4.5 Conclusion

Beam hardening is an undesirable effect in X-ray Computed Tomography (CT) which results in artifacts, particularly, cupping artifacts in images reconstructed using Filtered Back Projection (FBP) algorithm. In this chapter, a physics-based beam hardening correction scheme in X-ray CT is presented. This scheme, using information of the source spectrum and CAD model of the object, exploits the underlying physics of beam hardening phenomenon by incorporating energy dependence in the Lambert-Beer's attenuation law.

The proposed model-based correction scheme has been applied to both simulation and experimental X-ray data. The performance of the correction scheme was evaluated as a function of contrast level between the defects and the host materials. The simulation results clearly demonstrate the importance of the correction scheme particularly when there is a low contrast defect in a sample. In the case of experimental data of a heavy tungsten sample, where the inherent cupping artifact due to beam hardening is apparent, the FBP reconstructed on BH corrected projection data has greatly reduced the artifacts as quantified in Table 4.1.

A parametric study of the dependence of cupping artifact on source energy shows that, this artifact becomes more prominent as the tube peak voltage increases as shown in Figure 4.12. This observation can be further explained by referring to the spectral plot of mass attenuation coefficient of Tungsten upto 320 keV in Figure 4.3. As seen in the figure, this attenuation coefficient is relatively high at lower energy, decreasing with increase in energy. Thus cupping artifact is more pronounced with higher peak source voltages.

Chapter 5

Nuclear Fuel Rods Inspection using X-ray Computed Tomography

5.1 Introduction

Nuclear fuel material, such as the uranium isotope U-235 (^{235}U) and the plutonium isotope Pu-239 (^{239}Pu), is consumed in nuclear power plants to generate energy. This energy is used to heat water to pressurized steam, which drives the turbine generator. For use as nuclear fuel, enriched UF_6 is converted into uranium dioxide (UO_2) powder that is then processed into pellet form. The ceramic oxide pellets are stacked, according to each reactor core's design specifications, into tubes of corrosion-resistant metal alloy, usually zirconium alloys to form nuclear fuel rods. There is a very thin layer of gap between the cladding and the oxide pellets. This gap is filled with pressurized helium in normal conditions but in the presence of a flaw, water partially fills the gap. These fuel rods are subject to extreme conditions such as high temperature, pressure and radiation level. In nuclear reactors, an interaction between the ceramic oxide pellet and the surrounding

zircaloy cladding can occur during transient power condition leading to cladding failure by stress corrosion cracking [32]. Such an interaction is termed *Pellet-Cladding Interaction* (PCI). The inner surface cracks continue as radial fuel cracks and are highly concentrated in the vicinity of pellet-pellet interface. Figure 5.1 shows a real photographic image of a Missing Pellet Surface (MPS) and through-wall crack of a failed rod caused by PCI, revealing the propagation of a defect from one region to another [33].

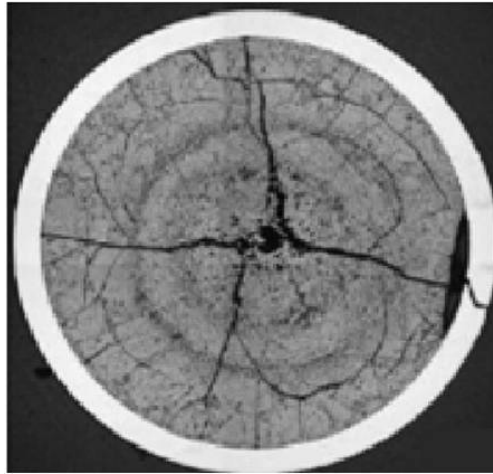


Figure 5.1: A missing pellet surface and through-wall crack of a failed fuel rod [33]

In order to avoid failures during the operation of a nuclear power plant under normal and transient conditions, it is necessary to maintain a high quality assurance of the components, especially the fuel pellets enclosed in zircaloy cladding. It is vitally important for the pellet surface to remain free from pits, cracks and chipping defects after it is loaded into the tubes to prevent local hot spots during reactor operation. The correct identification of failed rods, including fuel pellets, is important for safe operation of the power plant. The inspection of the fuel rod, however, presents several challenges [34]. There exist several methods of inspecting nuclear fuel pellets in a nuclear power plant. However, some of these methods have some inherent drawbacks as presented in the next section. X-ray computed tomography is proposed here in this thesis as a viable approach for inspecting pellets contained within the zircaloy tube.

5.2 Existing Methods of Nuclear Fuel Rods Inspection

5.2.1 Ultrasonic Inspection

Ultrasonic Testing (UT) uses high frequency sound energy to conduct examinations and make measurements. UT methods proposed and/or used in nuclear power plant include: *ultrasonic pulse-echo technique*, *ultrasonic guided wave inspection* and *ultrasonic resonance phenomena*.

The *ultrasonic pulse-echo technique* as described in [35] is based on the ability of the ultrasonic wave to distinguish between the presence of gas or water inside the rod gap. The difference in acoustic impedances of water and gas forms the physical basis for the inspection. The presence of water inside the gap thus indicates the presence of defect and hence rod failure. The drawbacks of this technique include the following:

- Due to the curvature of the fuel rod, the complicated nature of the reflected waveform would make the ultrasonic pulse-echo technique inapplicable.
- The *signal to noise* SNR ratio will be very low due to the discontinuity between the cladding and the fuel pellet.
- Based on the physical principle of the inspection method (which is the presence of water or gas inside the gap), defects located inside the pellets layer will not be detected.

The *ultrasonic guided wave inspection* is an active technique whereby an ultrasonic pulse is sent to interrogate a long path through the fuel rod. This guided wave propagates in the axial direction of a layer, while behaving as a standing wave through the rod [36]. A guided-wave probe, based on magnetostrictive sensor (MsS) technology operates at 250 kHz and detects the returned

guided wave signals from the end of the rods. A defect will be indicated by partial reflected signals along the length of the rod. The drawbacks of this technique include the following:

- This technique will detect flaws along the surface of the rod, but not flaws that originate from the surface and propagate into the inner pellet layer of the rod.
- It can only detect the presence of a defect but cannot characterize the defect. A separate additional sophisticated technique will be needed to characterize the defect.
- Guided waves inspection techniques have been used in geometries like beams and plates because of their simple geometries. However, the mechanics of propagation of guided circumferential waves has to be fully understood before the ultrasonic guided wave inspection technique can be applied to the inspection of nuclear fuel rods.

The *ultrasonic resonance phenomena* is used to detect leak-defective fuel rods using the circumferential Lamb waves excited by the resonance backscattering of ultrasonic pulses. These circumferential waves are elastic waves circumnavigating the cladding tube of the nuclear fuel rod and undergo transition to Lamb waves as the curvature of the tube is increased [37]. Depending on the curvature of the tube, there is a characteristic frequency region where each circumferential wave mode propagates well [38]. The lowest order symmetric (S_0) mode is used to detect the presence of water in the nuclear fuel rod. The drawbacks of this technique include the following:

- This technique will not be able to inspect assembled fuel rods because the inter-rod spacing in the assembly is too narrow (2-3 mm) to insert sensors with center frequency of 1 MHz, a frequency region at which the S_0 mode propagates well.
- In the presence of ambient noise, an otherwise healthy post-irradiated rod can be diagnosed

as failed rod because their very weak periodic resonance echoes are embedded in the noise.

This will lead to a false alarm which can be cost-expensive.

- The technique will only detect a water-filled rod but not the actual amount of water which can be used to compare against any given threshold value for failed and sound fuel rods.

5.2.2 Visual Inspection and Photography

Visual inspections include both human-based vision system and automated vision system. The human-based vision inspection method is the use of the naked eye or a periscope to judge which fuel rods are good or bad. The inherent drawbacks are:

- Very laborious and subject to inconsistencies and error.
- The inspection personnel is exposed to radiation.
- Very time-consuming and hence economically inefficient.

Automated visual system consists of a handling system to feed the fuel rods, an imaging system and image processing software [39]. One such system described in [40] uses photographic images of pellets and three artificial intelligence techniques for image analysis and defect classification. In the method, each nuclear fuel pellet was photographed 4 times at rotations of 90° each to provide the inspector with a 360° view of each pellet [41]. Each black and white negative was then scanned into the computer in a 256 grayscale image. These grayscale images are then pre-processed for pellet defect enhancement and features extraction. The output from this pre-processing stage is then given simultaneously to fuzzy logic, decision tree and neural network for automatic detection and classification of defects. The main drawbacks of these techniques are:

- It fails when inspecting fuel pellets already enclosed in the zircaloy cladding.
- Using photography, it can only image defects on the surface of the pellets.
- In the pre-processing part, the reference model has to be searched each time for each pellet.

5.2.3 Eddy Current Inspection

Eddy current inspection for nuclear fuel rods inspection has been proposed to inspect fuel cladding imperfections [42]. The apparatus used here consists of two differential coils through which the fuel rod is drawn. The output signal from the coil is displayed on the screen. A standard Zircaloy tube containing both internal and external defects is used to calibrate the eddy current system. The main drawbacks here are:

- The measured values of electrical conductivity of nearly stoichiometric single-crystal and polycrystalline uranium dioxide (UO_2) from room temperature to 3000°K as given in [43] indicate that it will be impossible to detect defects in the uranium dioxide pellet region because UO_2 is non-conducting.
- The eddy current method cannot be used in a fuel bundle without disassembling it.

5.2.4 Sipping Test

Sipping is an inspection technique used to inspect suspected nuclear fuel rod by investigating the fission product released in a fixed volume of circulating reactor cooling water [44]. In this test, the fuel rod to be inspected is placed in the sipping assembly which is a fixed volume of water in a container with two hoses attached; one at the bottom and one at the top for circulating this volume of water through the container containing the fuel rod. A failed nuclear fuel rod would release the

radioactive products of nuclear fission reaction through the zircaloy cladding into the circulating water. As time goes on, the concentration of these radioactive products in the sipping water will increase thus indicating the presence of a failed rod. This method of fuel rod inspection has some drawbacks namely:

- It may indicate the presence of a defected rod but not its exact location in the fuel bundle.
- A failed fuel rod with defects in the pellet region with an otherwise healthy cladding will go undetected since there will not be any release of radioactive products into the circulating water.

5.3 Assessment of Nuclear Fuel Pellets using X-ray Computed Tomography

X-ray computed tomography is proposed as a viable approach capable of overcoming the aforementioned drawbacks of the existing inspection methods. Using an X-ray source of appropriate energy capable of penetrating a cross-section of the tube, the transmitted X-rays photons recorded and used with a reconstruction algorithm to image flaws in the pellets. However, given the high atomic number of Zirconium (which makes up about 98% composition by weight of Zircaloy [45]), the incident X-ray beam will be severely attenuated as it passes through the cross-section of the rod leading to increased exposure times for measuring a projection. In order to reduce the time for imaging there is a need to develop reconstruction algorithms using as few projections as possible. However limited number of projections implies an insufficiently filled Radon Space rendering imaging via inverse Radon transform unsuitable [46]. Any attempt to invert from the insufficiently filled Radon space back to the object space during the reconstruction problem gives

rise to undesired artifacts which should be removed. In this thesis, the feasibility of using X-ray inspection techniques for imaging fuel pellets using limited number of projections is presented. A novel artifact removal algorithm is proposed and its performance is demonstrated using simulation data [15].

5.3.1 Convex Interpolation in the projection domain

Given an object with spatial distribution of attenuation coefficient $\mu(x, y)$, the X-ray projection $p(s, \theta)$ or Radon Transform of the object at different detector element positions s and for several source locations θ is given by [1]:

$$p(s, \theta) = \int_L \mu(x, y) du \quad (5.1)$$

where

L is the path of the ray

u is the distance along L

Each point in the Radon domain is called a *ray-sum* while the resulting image over all values of θ is called a *sinogram*. Image reconstruction is the problem of inverting the finite number of projections to yield an estimate of $\mu(x, y)$.

Estimating $\mu(x, y)$ in Equation (5.1) using a limited number of projections gives rise to undesired artifacts. One way to reduce and/or eliminate these lines is to interpolate the projection data to completely fill up the Radon space before inverting back to the image space. There are diverse interpolation algorithms with the simplest being nearest-neighbor replication which, however, suffers from a blocky effect [47]. A novel interpolation approach proposed in this thesis

is the *convex interpolation* [15]. Given two measured projections $P_1(s, \theta_1)$ and $P_2(s, \theta_2)$ where $s \in [-s_{max}, s_{max}]$ and $\theta_i \in [0^\circ, 360^\circ]$, an interpolated projection $P'(s, \theta)$ is expressed as:

$$P'(s, \theta) = \lambda P_1(s, \theta_1) + (1 - \lambda) P_2(s, \theta_2) \quad 0 \leq \lambda \leq 1 \quad (5.2)$$

These interpolated projections are used to fill up the Radon space in a continuous manner as λ varies continuously from 0 to 1. When $\lambda = 0$, $P'(s, \theta) = P_2(s, \theta_2)$. When $\lambda = 1$, $P'(s, \theta) = P_1(s, \theta_1)$.

The implementation for this interpolation technique is described next. Consider the availability of N number of X-ray projections, acquired over complete 360° rotation at regular interval, where N is a factor of 360.

Let P_1, P_2, \dots, P_N be the projections acquired respectively at orientations $\theta_1, \theta_2, \dots, \theta_N$. The following step-wise procedure is used to fill up the Radon space (sinogram):

1. Create a vector λ of ΔN elements linearly spaced between 0 and 1 inclusive, where $\Delta N = \frac{360}{N}$
2. Initialize the sinogram (Radon space) by creating a zero matrix R of size $S \times 360$, where S is the number of sensors in the detector array.
3. Using the first consecutive pair of acquired projections P_1 and P_2 , interpolate following Equation (5.2) to obtain ΔN projections between them as:

$$P_i = (1 - \lambda_i) P_1(:, \theta_1) + \lambda_i P_2(:, \theta_2), \quad 0 \leq \lambda_i \leq 1, \quad i = 1, \dots, \Delta N$$

Then fill Radon space as: $R(:, i) = P_i$

4. For subsequent consecutive pairs of acquired projections P_{k-1} and P_k ($k > 1$), interpolate

following Equation (5.2) to obtain ΔN projections between them as:

$$P_i = (1 - \lambda_i) P_{k-1}(:, \theta_{k-1}) + \lambda_i P_k(:, \theta_k), \quad 0 \leq \lambda_i \leq 1, \quad i = 1, \dots, \Delta N$$

Then fill Radon space as: $R(:, (k-1)\Delta N + i) = P_i$

5. Reconstruct the image using the filled Radon space R .

5.3.2 Simulation and Results

A cross-section of the rod of inner and outer radii of 0.38" and 0.44" respectively was simulated with a notch defect of size $0.04" \times 0.02"$ introduced at the $\text{UO}_2/\text{zircaloy}$ interface as shown in Figure 5.2.

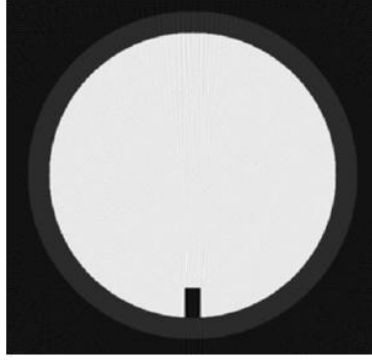


Figure 5.2: Sample 1 with notch defect at $\text{UO}_2/\text{zircaloy}$ interface

The sample is illuminated by a 200 kV_p X-ray source located at an optimum (measured from the fan-beam vertex to the center of rotation) distance $D = \sqrt{2}N$ ($N \times N$ is the size of the entire image). X-ray fan-beam projections were obtained from sample 1 and used to reconstruct images of the sample. The original sinogram with 9 projections is shown in Figure 5.3a and compared with the sinogram of Figure 5.3b obtained using the proposed convex interpolation scheme.

Figures 5.4a and 5.4b show the reconstructed images for the sample with notch defect using 60 projections without and with convex interpolation in the projection domain respectively.

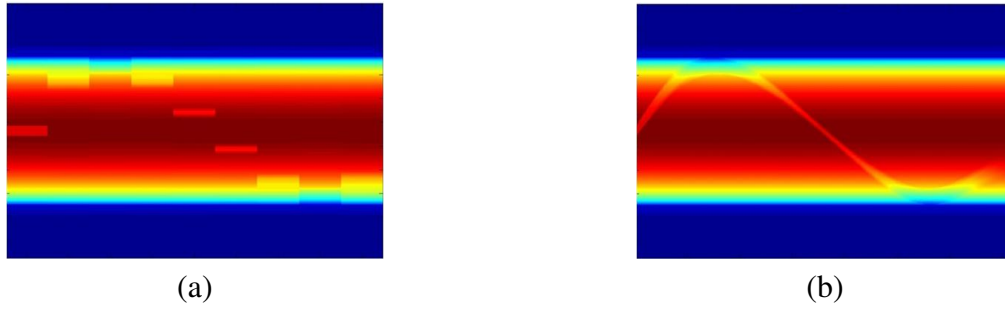


Figure 5.3: Original and interpolated sinograms with 9 projections: (a) Original (b) Interpolated. For interpretation of the references to color in this and all other figures, the reader is referred to the electronic version of this dissertation.

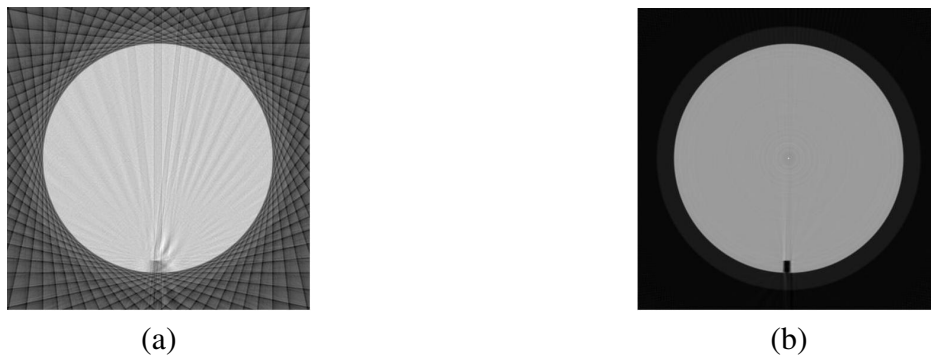


Figure 5.4: Reconstructed Images with 60 projections [15]: (a) Without and (b) With convex interpolation

The reconstructed images of sample 1 using 9 fan-beam projections without and with convex interpolation in the projection domain are also shown in Figures 5.5a and 5.5b respectively.



Figure 5.5: Reconstructed Images with 9 projections [15]: (a) Without and (b) With convex interpolation

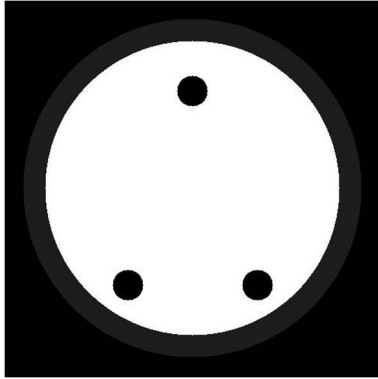
The performance of the proposed interpolation technique was evaluated by introducing a non-symmetric defect of size $0.02'' \times 0.02''$ in the UO_2 layer of sample 2. This sample was reconstructed using 9 projections acquired at 200 kV_p and the results are given in Figure 5.6.



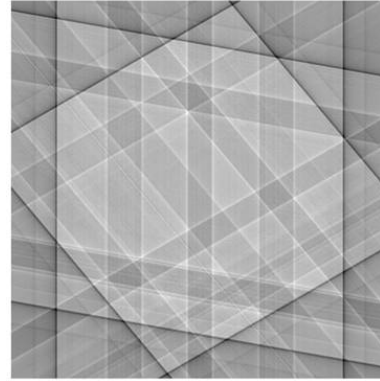
Figure 5.6: Performance on non-symmetric defect using 9 projections: (a) Without and (b) With convex interpolation

To show the performance of the proposed technique in the presence of multiple defects, sample 3 was simulated with 3 circular defects of $0.04''$ diameter introduced as shown in Figure 5.7a. This cross-section was illuminated by a 200 kV_p X-ray source and 9 fan-beam projections were acquired. Figures 5.7b and 5.7c show the reconstructed images without and with convex interpolation in the projection domain respectively. The reconstructed image in Figure 5.7c after applying convex interpolation was further thresholded to detect the 3 defects as shown in Figure 5.7d.

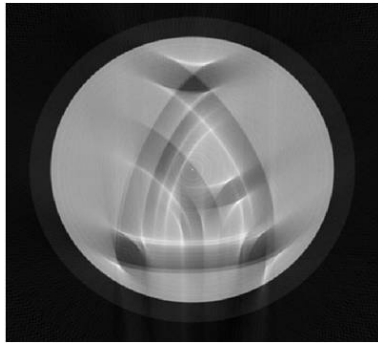
To further evaluate the performance of the proposed technique, a real photographic image of a Missing Pellet Surface (MPS) and through-wall crack of a failed fuel rod shown in Figure 5.8a [33] was preprocessed and then used as input into the tomographic imaging algorithm. Figure 5.8b shows the preprocessed binary image while the reconstructed image of the real defect sample using 30 fan-beam projections with the application of convex interpolation in the projection domain is shown in Figure 5.8c. Applying thresholding, the final reconstructed image is given in Figure 5.8d.



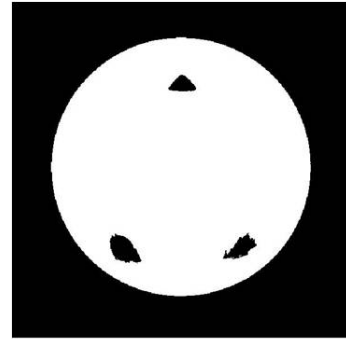
(a)



(b)

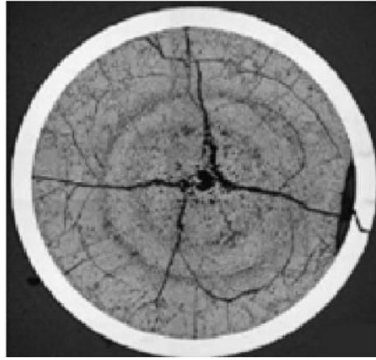


(c)



(d)

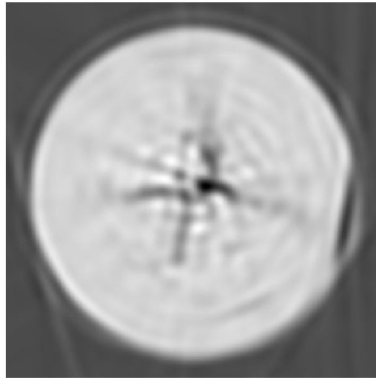
Figure 5.7: Results using 9 projections [15]: (a) Phantom with defects; (b) Reconstruction without convex interpolation; (c) Reconstruction with convex interpolation; (d) After thresholding (c)



(a)



(b)



(c)



(d)

Figure 5.8: Results using 30 projections on sample with real defect [15]: (a) Optical image; (b) Preprocessed image; (c) Reconstruction with convex interpolation; (d) After thresholding (c)

5.3.3 Experimental Validation of Convex Interpolation Technique

The validity of the technique was tested using experimental data. The sample used in the experiment was a high density (HDPE) rod of diameter 1.56". Four defects, each of diameter 0.11", were machined along the axial direction of the rod. Figure 5.9 is a schematic diagram of the cross-section of the HDPE rod showing the machined defects (holes) with specified dimensions. The mass attenuation coefficient for HDPE is $0.182 \text{ cm}^2/\text{g}$ at 80 keV [30]. Experimental projections

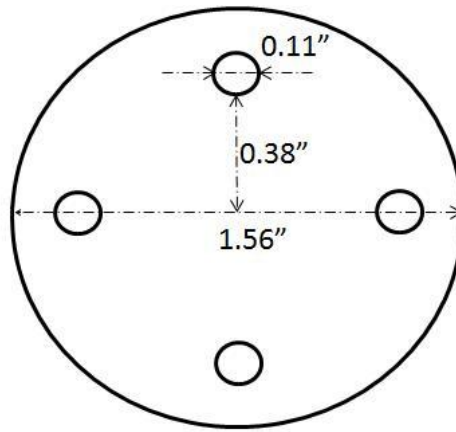


Figure 5.9: Cross-sectional diagram of the test sample with machined defects

were acquired using a GE vertical X-ray inspection system having a 150 kV_p microfocus X-ray source from Hamamatsu with peak current of 500 μA . The detector is a high resolution 12-bit CCD with 1024×1024 pixels, 4096 gray levels. The source-to-object and source-to-detector distances were 20" and 36" respectively. Since the X-ray source and detector are both fixed, the sample was mounted on a rotational stage to get a complete tomographic scan. This rotational stage was controlled by Labview software. The sample was rotated at regular angular intervals over a complete range (0° to 360°) to collect projection data from different directions. Figure 5.10 shows the side view of the sample mounted on the rotational stage inside the X-ray chamber. The tube voltage and current were optimized to acquire the best signal (radiographic data). The optimum

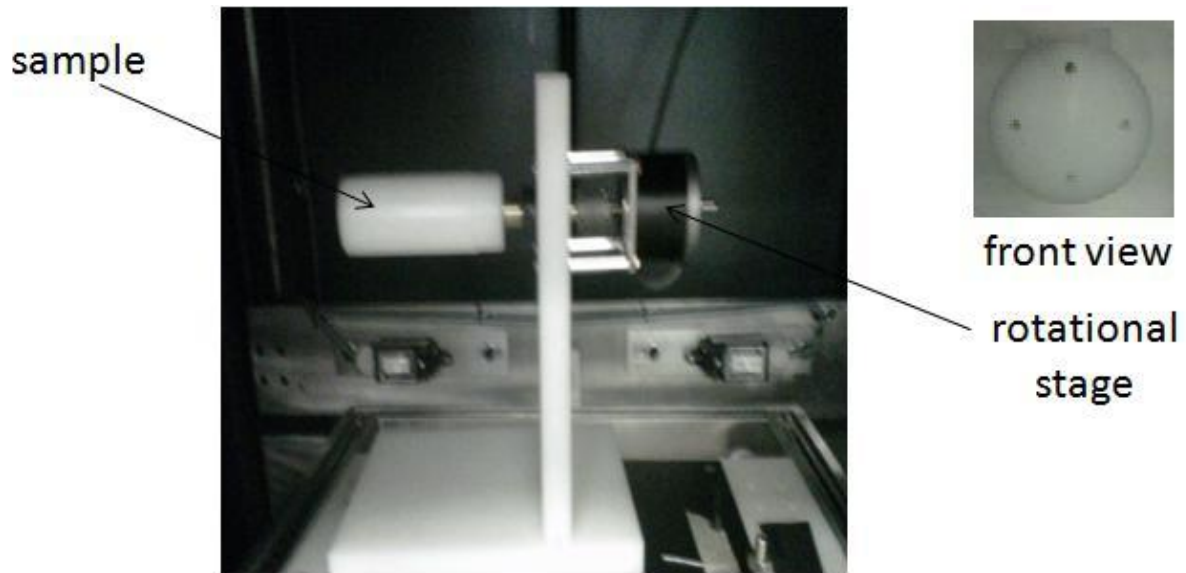


Figure 5.10: Side view of the sample mounted on a rotational stage. Front view of the sample also inserted

values used for the sample in this experiment were 77.7 kV_p and $122 \mu\text{A}$. X-ray measurements were taken at 18 different orientations at angular increments of 18° . Figure 5.11 shows the raw 2-D radiographic data of the sample taken at angle 0° relative to the X-ray source.

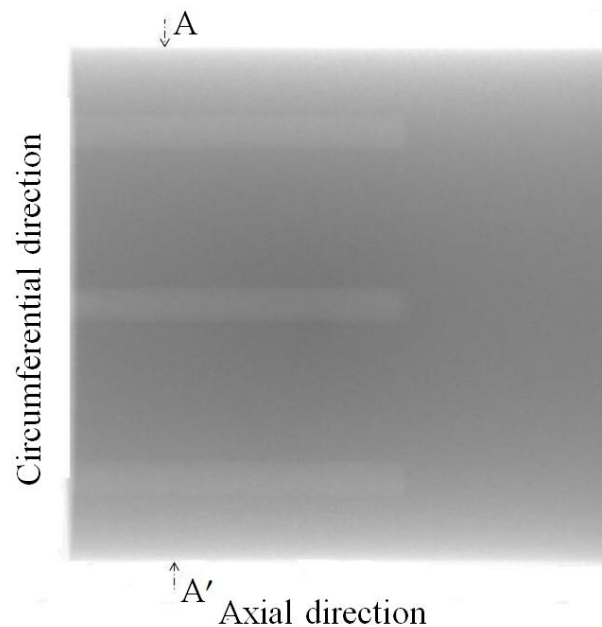


Figure 5.11: Raw 2-D radiographic data of the sample taken at angle 0°

The 2-D raw data was preprocessed and log-normalized to give a 2-D projection data at that particular angle $\theta = 0^\circ$. For 2-D tomographic reconstruction of the sample, a 1-D projection data was taken from the 2-D projection data along the line A-A' indicated in Figure 5.11. The 1-D projection data for this orientation is shown in Figure 5.12.

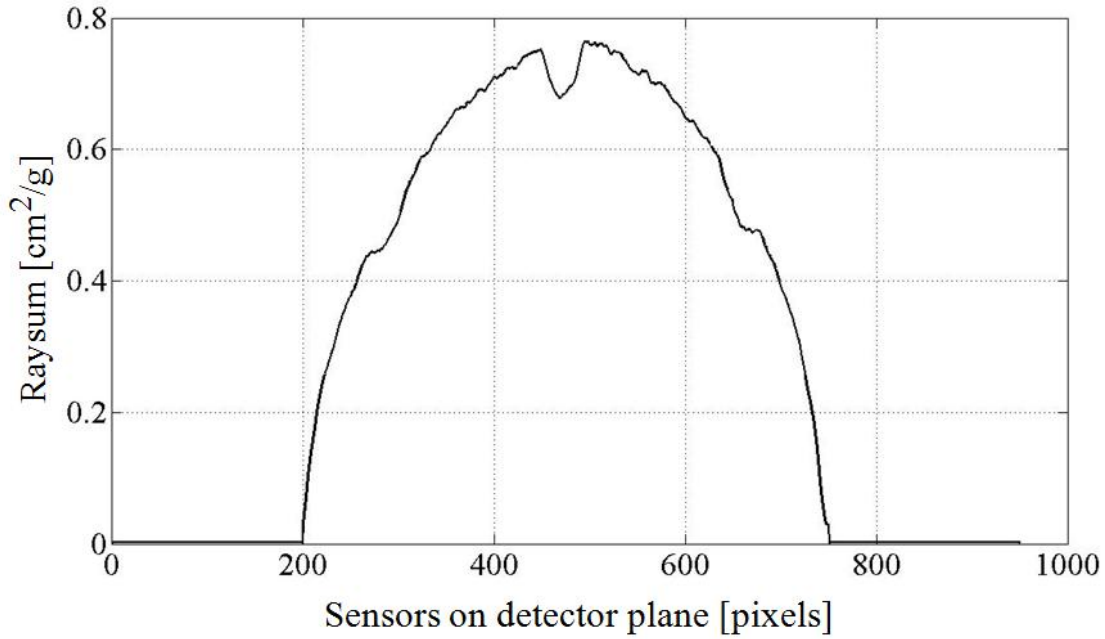


Figure 5.12: Projection data acquired at angle 0°

A cross-sectional slice of the sample (with machined defects) was reconstructed by implementing the technique proposed above using 18 experimental projections and the reconstructed result is shown in Figure 5.13. This reconstructed image was further thresholded to detect the four defects as shown in Figure 5.14.

FBP result, reconstructed using the same experimental projection without convex interpolation applied in the projection domain, is also given in Figure 5.15 for comparison. As shown in Figure 5.15, data insufficiency in the projection domain leads to undesired artifact lines in the FBP reconstructed image rendering it unusable to detect the presence of defects. Even though, there

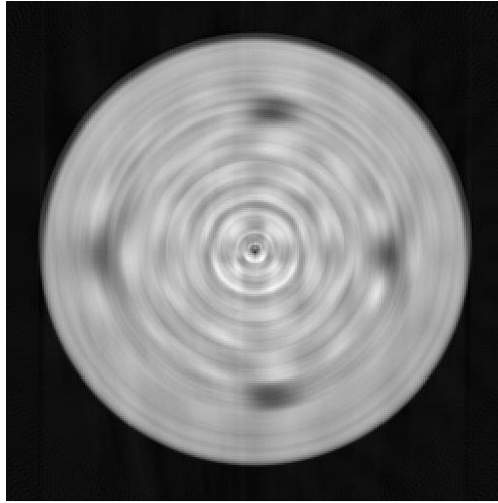


Figure 5.13: Reconstructed result with convex interpolation

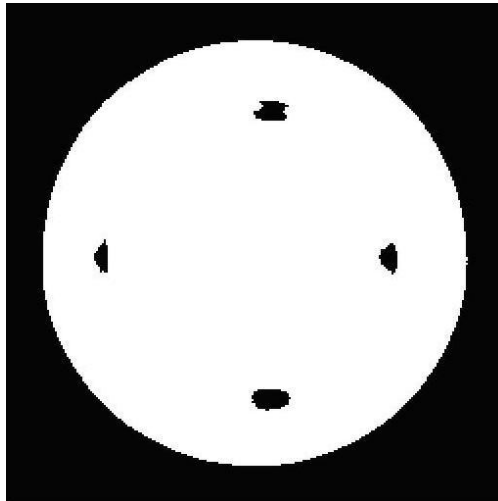


Figure 5.14: Result with convex interpolation and thresholding

is still some indication of the presence of defects in Figure 5.15, it is however difficult to tell exactly where and how many defects are there without any prior knowledge about the sample. But by applying convex interpolation to the limited number of projections available, it is possible to reconstruct a cross-sectional slice of the sample and detect defects as evident from the result in Figure 5.13. Thresholding even enhances the detectability of the defects even further as shown in Figure 5.14.

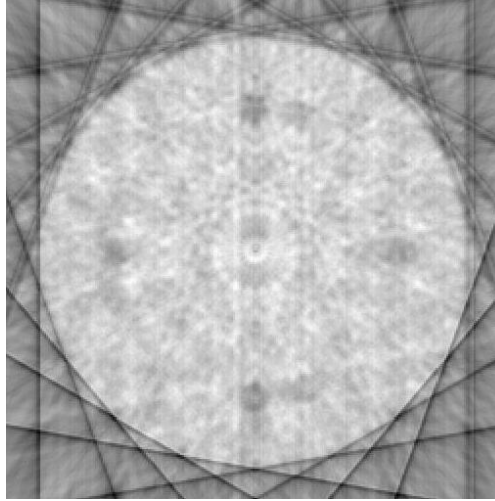


Figure 5.15: FBP reconstructed result without convex interpolation

5.3.4 Implementation Results with Low Contrast Data

The performance of the proposed interpolation technique was further investigated by using a phantom with very low (10 %) contrast defects shown in Figure 5.16. The sample consists of 2 concentric circles with inner and outer radii of 0.38 " and 0.44 " respectively. The materials in the 2 concentric layers are Uranium dioxide (inner) and Zirconium alloy (outer), whose mass attenuation coefficients at 300 keV are $0.4704 \text{ cm}^2/\text{g}$ and $0.1322 \text{ cm}^2/\text{g}$ respectively.

The phantom shown in Figure 5.16 was reconstructed by implementing the proposed convex interpolation technique on 9 acquired X-ray projections at 300 keV. The reconstructed results are shown in Figure 5.17 for the case obtained with FBP without convex interpolation (a) and with convex interpolation applied (b).

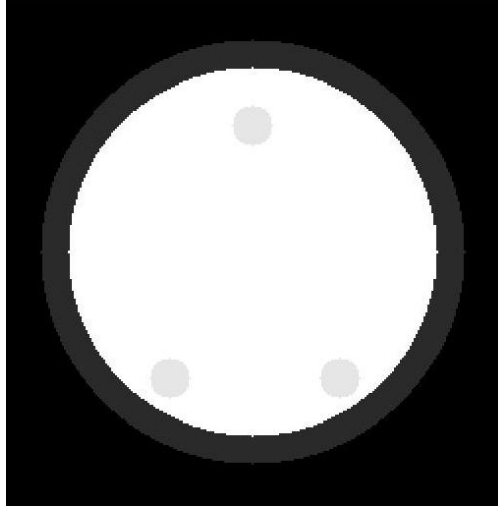
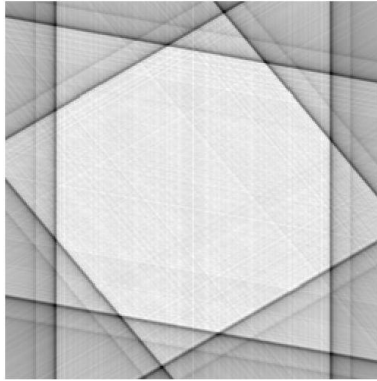
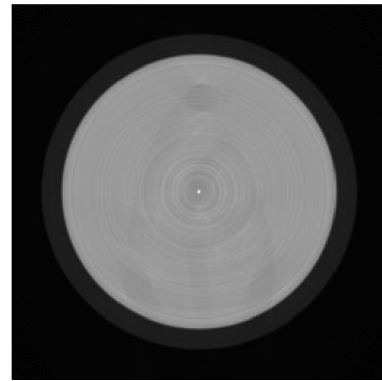


Figure 5.16: Phantom with defects



(a)



(b)

Figure 5.17: Reconstructed Images with 9 projections: (a) Without and (b) With convex interpolation

5.3.5 Reconstruction Error as a Function of Number of Projections

The effect of the number of projections on the quality of a reconstructed image was evaluated by computing the mean-square-error (MSE) of the reconstructed image as a function of number of projection. MSE is computed using Equation (4.8) and the result is shown in Figure 5.18 from 1 to 360 projections.

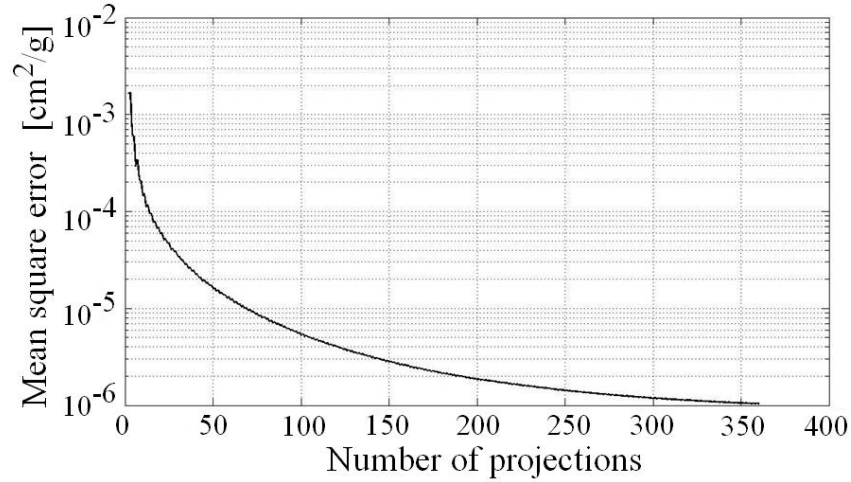


Figure 5.18: Mean square error as a function of number of projections

As seen in Figure 5.18, MSE decreases with increase in the number of projections from which the image is reconstructed. An ideal number of projections can be recommended based on the desired image quality of the reconstructed image.

5.4 Conclusion

Fuel rods in nuclear power plants consist of ceramic uranium dioxide pellets enclosed in Zircaloy tubes. It is vitally important for the pellet surface to remain free from pits, cracks and chipping defects after it is loaded into the tubes to prevent local hot spots during reactor operation. The inspection of the fuel rod presents several challenges. Low frequency electromagnetic methods cannot be used since the ceramic pellets are nonconducting. Microwave methods cannot be employed since the cladding acts as a shield and would prevent the energy from entering the tube. Ultrasonic methods (UT) offer poor signal-to-noise ratio due to the ceramic nature of the pellet. Flaws that are located close to the axis of the tube are particularly difficult to detect using UT.

The feasibility of using X-ray Computed Tomography (CT) to inspect nuclear fuel rods has

been investigated in this chapter. Simulation and experimental results show that, using an X-ray source of 320 keV, it should be possible to image defects of size $0.04'' \times 0.02''$ in nuclear fuel rods. For real-time tomography, data acquisition time is critical. This calls for the need to reconstruct from limited number of projections. However, projection data insufficiency leads to undesired artifacts in FBP reconstructed image. Filling up the Radon space is essential to remove these artifacts.

This chapter has presented a convex interpolation technique for filling up the Radon space. The performance of the technique has been demonstrated using simulation data. Experimental validation of the proposed technique on experimental data acquired from an HDPE rod with machined defects is also presented. The reconstruction results presented here indicate that convex interpolation technique is an effective technique for filling up insufficiently filled sinogram in X-ray CT. This technique is effective even in the presence of very low contrast defects as shown in the results in Section 5.3.4.

Instead of using energy of X-rays to inspect uranium dioxide pellets in the nuclear power plant, an interesting technique will be to use the uranium dioxide pellet itself as the source of the energy. These pellets are made up of uranium-235 (U-235), an isotope of uranium making up 0.72% of natural uranium. The fission of one atom of U-235 generates 202.5 MeV of energy [50]. This energy is made up of energy of different products of the fission reaction including gamma rays, beta particles, neutrons etc. If at least one neutron from U-235 fission strikes another nucleus and causes it to fission, then the chain reaction will continue. This fission chain reaction produces intermediate mass fragments which are highly radioactive and produce further energy by their radioactive decay. An understanding and modeling of this fission chain reaction could open up a new research window in using uranium as a source of energy for computed tomography.

Chapter 6

X-ray Tomographic Inspection of Nuclear Fuel Rods using a Limited Number of Projections

6.1 Introduction

For real-time X-ray CT imaging of nuclear fuel rods, data acquisition and processing speed are very critical. Thus there is a need to reduce the number of projections. However limited number of projections implies an insufficiently filled Radon Space rendering imaging via inverse Radon transform unsuitable [46]. Any attempt to invert from the insufficiently filled Radon space back to the object space using a conventional Filtered Back Projection (FBP) algorithm gives rise to undesired artifacts. In [17] the feasibility of using x-ray inspection techniques for imaging fuel pellets using a limited number of projections was investigated and a statistical reconstruction algorithm is presented along with results on experimental data.

6.2 Experimental work and Projections

Given the radioactive nature of Uranium, for the purpose of experimental work, heavy Tungsten Alloy was used as a surrogate material for UO_2 [48]. Tungsten Alloy 18.5 was selected based on the close resemblance of their attenuation coefficients as shown in Figure 6.1. Tungsten Alloy 18.5 is a heavy metal alloy made up of 97% tungsten, 2.1% nickel and 0.9% iron. 18.5 refers to the density of the alloy in g/cm^3 .

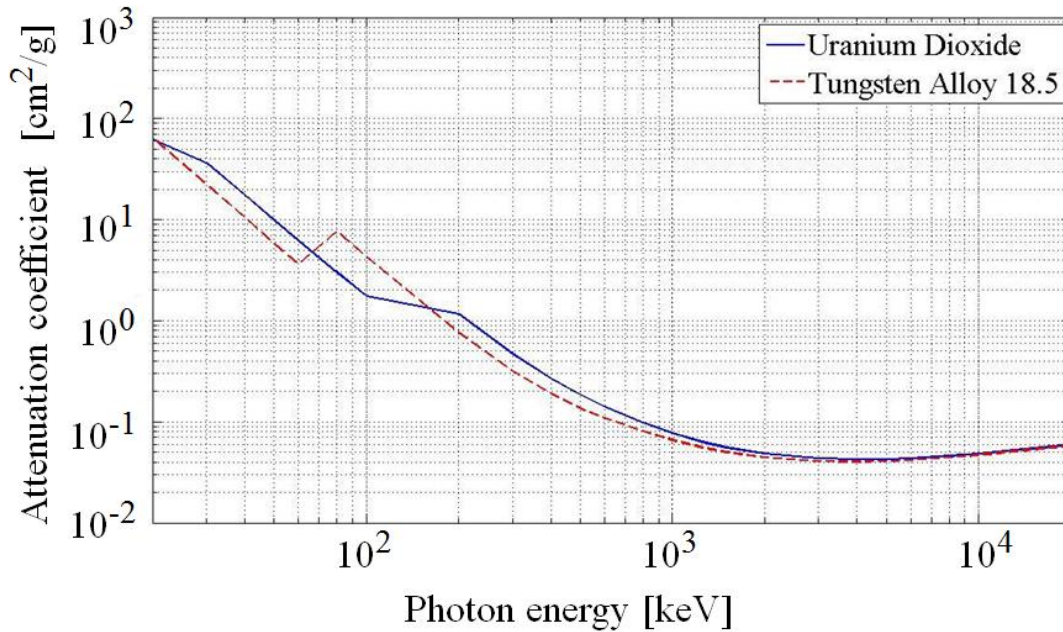


Figure 6.1: Photon mass attenuation coefficients for Uranium dioxide and Tungsten alloy 18.5

A 12" tungsten rod of 0.375" diameter was acquired and a circular notch of diameter 0.065" and depth 0.045" was machined on it. Figure 6.2 shows a photograph of the tungsten rod alongside a zirconium alloy (zircaloy) tube that is used as cladding to enclose the nuclear fuel (UO_2) pellet. This specimen (UO_2 pellet inside zircaloy cladding) served as a surrogate for a nuclear fuel rod.

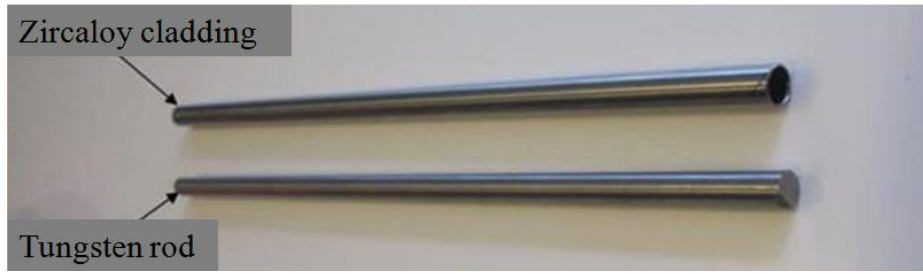


Figure 6.2: Photograph of Tungsten rod alongside Zircaloy cladding

Figure 6.3 below shows a side view of the experimental set-up using a computed radiography system where the Source-to-Film distance was 60" and the focal spot was 4.0 mm. A 1/32" lead filter was placed between the X-ray source and the sample to minimize beam hardening effect caused by the polychromatic beam produced by the X-ray source [49]. The spatial resolution of the computed radiography plate used was 500 μm

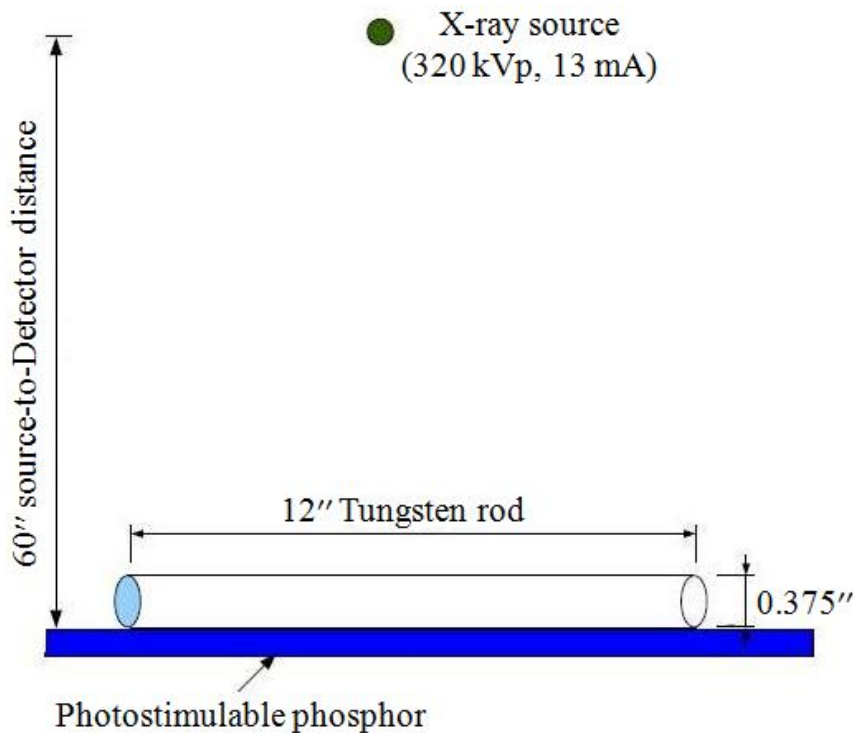


Figure 6.3: Experimental Set-Up (side view) of CR system

The values for the tube voltage, current and exposure time were optimized to acquire the best signal (projection data). X-ray projection measurements were taken at eight different orientations

at angular increments of 45° using a 320 KV_p and 13 mA X-ray source with the notch defect directly beneath the X-ray source for 4 min. Figures 6.4 - 6.7 show the eight experimental projection data (ray-sums) of the tungsten rod sample inside the Zircaloy tube after processing the raw data based on Equation (5.1).

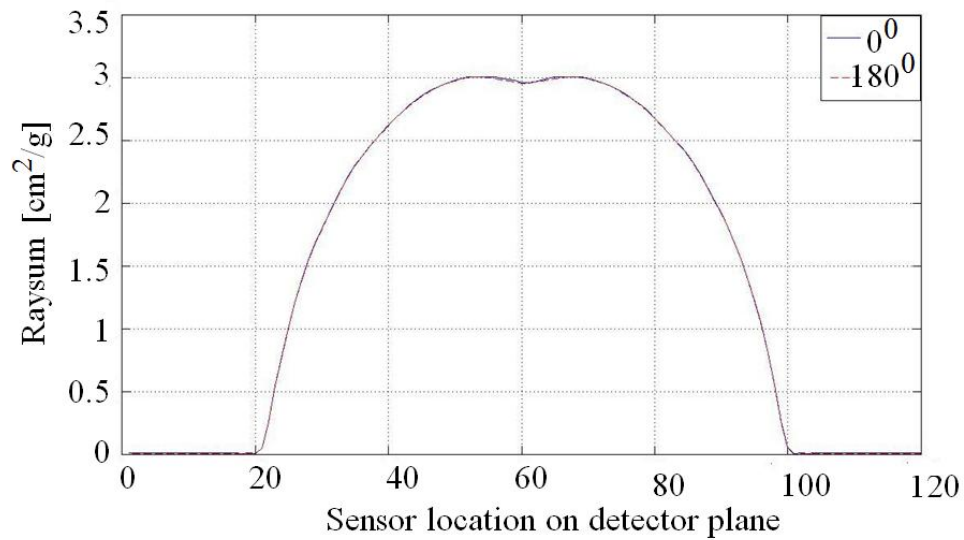


Figure 6.4: Projection data acquired at 0° and 180°

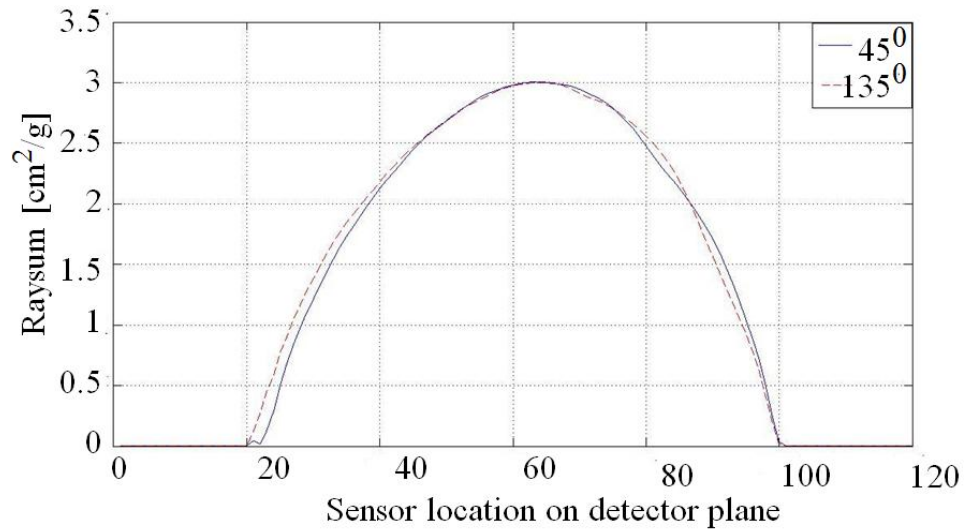


Figure 6.5: Projection data acquired at 45° and 135°

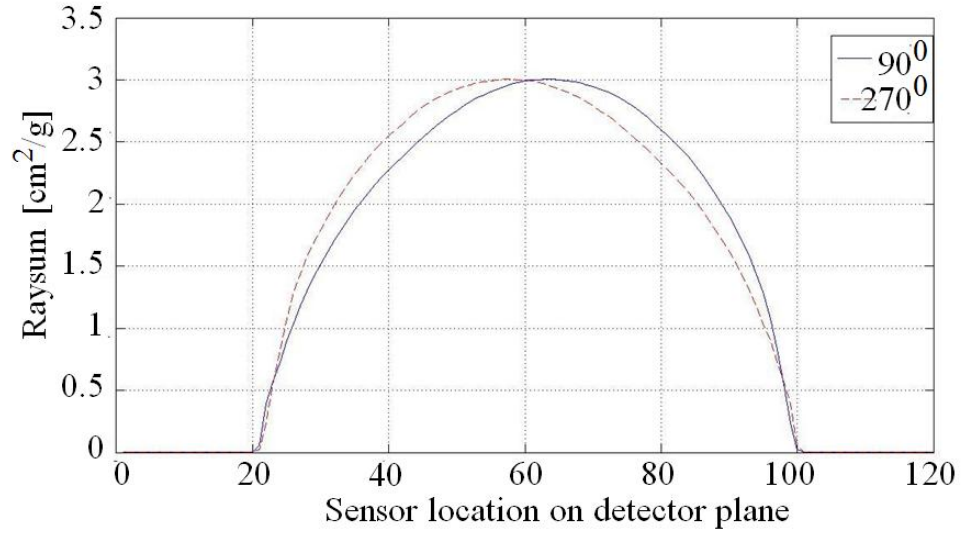


Figure 6.6: Projection data acquired at 90° and 270°

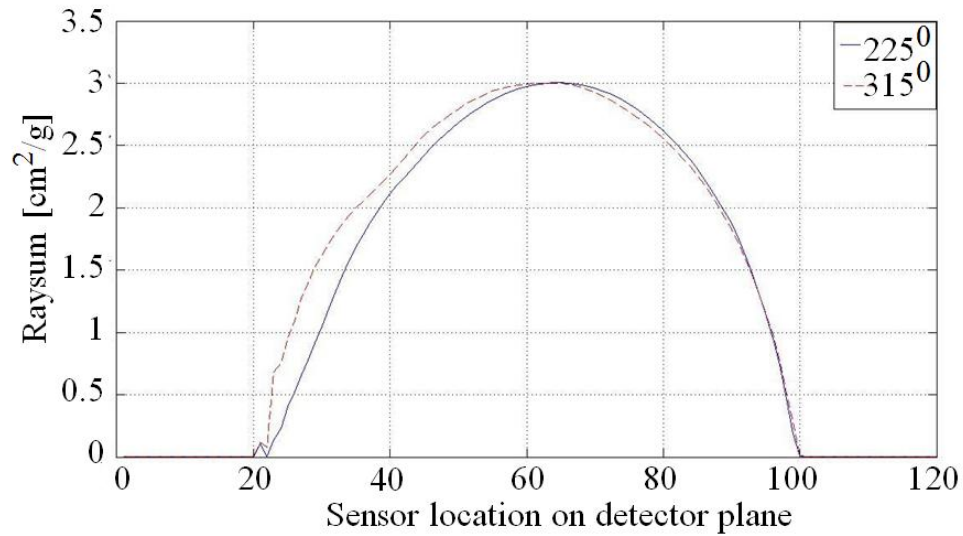


Figure 6.7: Projection data acquired at 225° and 315°

6.3 Tomographic Reconstruction

6.3.1 The Filtered Back-projection Algorithm

Filtered Back-projection (FBP) is an analytical reconstruction technique that is used in commercial computed tomography scanners. It is based on the Radon transform and Fourier slice

theorem (described in Section 3.3), and its practical implementation takes advantage of the fast Fourier transform. The Radon Transform however assumes ideal conditions namely: infinite number of projections with infinitely thin X-ray beams, noiseless data, monoenergetic X-rays, etc. Thus for the case of limited number of X-ray projections, these conditions are violated and the FBP algorithm fails. There is thus the need of a more robust statistical reconstruction algorithm for image reconstruction from extremely limited number of X-ray projections.

6.3.2 Statistical Reconstruction Algorithm

Statistical reconstruction algorithms are typically based on accurate statistical modeling. Using the statistical model, a derived cost function is optimized by an iterative procedure that is subject to certain constraints.

According to Radon Theory, the projection $p(s, \theta)$ or Radon Transform of an object $\mu(x, y)$ at an angle θ represents an analytic transform for that object and is given by [1]:

$$p(s, \theta) = \ln \left(\frac{I_0}{I} \right) = \int_L \mu(x, y) du \quad (6.1)$$

In matrix form, Equation (6.1) can be written as:

$$p = T\mu \quad (6.2)$$

where

p is the projection data

T is the projection operator

μ is the mass attenuation coefficient

The inverse problem is the evaluation of μ from p . The ill-posed inversion problem in Equation (6.2) can be written in terms of a variational problem:

$$\hat{\mu} = \operatorname{argmin}_{\mu \in D} \{A(p, T\mu) + \alpha B(\mu)\} \quad (6.3)$$

where

A is the cost function

B is the smoothness constraint function

α is the regularization parameter

D is the set of admissible solutions

A statistical iterative algorithm (Binary Minimization Algorithm) for minimizing Equation (6.3) is presented in [46] for binary materials using a limited number of X-ray projections. Here, a binary material is defined as a sample that is characterized in terms of two states: 0 in regions of the host sample and 1 in the location of a defect. In solving Equation (6.3), start from a zero-level approximation $\mu^{(0)}$ (determined after the first step of reconstruction) and introduce an iterative sequence of approximations. At the end of the iteration, pixel values are inverted based on a criterion with a value that dictates the probability, ω_j , of inverting the value of pixel j . This transition probability, ω_j , is defined by [46]:

$$\omega_j = \begin{cases} |g_j| & \text{if } \left(\mu_j^{(k)} = 1 \text{ and } g_j < 0 \right) \\ & \text{or } \left(\mu_j^{(k)} = 0 \text{ and } g_j > 0 \right) \\ 0 & \text{otherwise} \end{cases} \quad (6.4)$$

where g_j represents the gradient of the weighted sum of the functionals A and B in Equation (6.3) at pixel j .

The value of g_j after the k^{th} iteration is expressed as [46]:

$$g_j = -2 \sum_{n=1}^N \sum_{i=1}^I \frac{I_{i,n} \left(P_{i,n} - P_{i,n}^{(k)} \right)}{\sigma_{i,n}^2} - 54\alpha \sum_{a=1}^{27} \left(\mu_{j,a} - \mu_j \right) \quad (6.5)$$

6.4 Proposed Technique

The cross-section of a nuclear fuel rod consists of two concentric layers of zircaloy tube and uranium dioxide pellet (UO_2). A defect can occur in the zircaloy layer, the UO_2 layer, or both. The technique given in Section 6.3.2 is valid for a problem containing two regions. In [17], an approach which extends the Binary Minimization Algorithm for a more complex test geometry comprising three materials was presented. In this approach, an *a priori* knowledge about the structure of the material is incorporated in the algorithm. The region of interest (ROI) is divided into 2 sub-regions: zircaloy tube layer and UO_2 pellet layer. Each of the sub-regions is a two-material problem. Region 1 contains a zircaloy layer with/without defect. Region 2 contains a UO_2 pellet with/without defect. Therefore, the reconstruction of each sub-region can be performed using the binary minimization procedure. In some cases, however, a defect can propagate from one region in to another, as shown in the photographic image of a Missing Pellet Surface (MPS) and through-wall crack of a failed fuel Rod in Figure 5.1 [33]. This situation is incorporated in the choice of B , the smoothness constraint function, in Equation (6.3).

Reconstructing a cross-section of the fuel rod was from the experimental projections in Figures

6.4 - 6.7 using the FBP algorithm gives the result shown in Figure 6.8, from where undesired artifact lines due to data insufficiency can be seen.

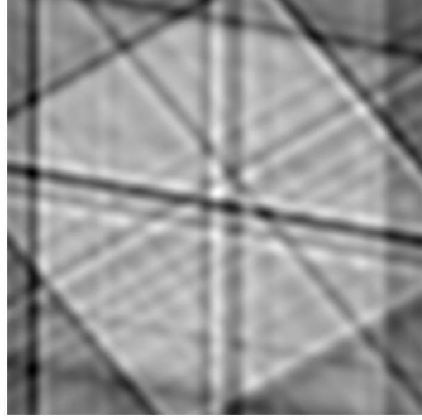


Figure 6.8: Reconstruction using FBP algorithm

The *a priori* knowledge about the location of the different materials was then added to the FBP reconstructed image of Figure 6.8 to create a virtual defect space (VDS). The set of admissible solutions D can be determined with the help of VDS [46]:

$$D = \left\{ \mu : \mu_j = \begin{cases} 0 \text{ or } 1 & j \in VDS \\ 0 & j \notin VDS \end{cases}, j = 1, \dots, J \right\} \quad (6.6)$$

The set of admissible solutions, D is a binary image shown in Figure 6.9. This is effectively the zero-level approximation used as the starting point in the proposed statistical reconstruction image. The algorithm then ran to adjust the values of the reconstructed attenuation coefficient at each pixel location.

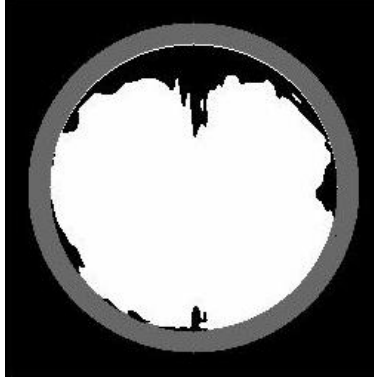


Figure 6.9: Initial guess

6.5 Results with Experimental data

A cross-sectional slice of the Tungsten rod (with machined notch defect) inside the Zircaloy tube was reconstructed by implementing the technique proposed above using the eight experimental projections of Figure 6.4, and acquired by the experimental procedure explained in Section 6.2. The reconstruction time varied with the regularization parameter, α , as the value of α controls the convergence of the reconstruction algorithm at each pixel location. The computational cost is 10 min. on a machine with 16 GB of memory and eight processors (each of 2.66 GHz speed) for the chosen value of $\alpha=50$ and imaging space of 512×512 pixels. Figures 6.10 and 6.11 show the reconstructed cross-sections of the nuclear fuel rod without and with zircaloy tube respectively.

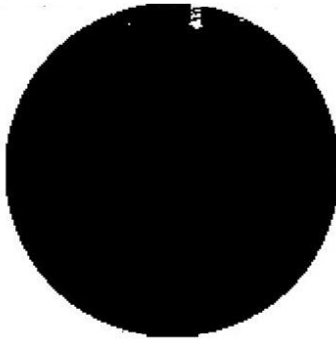


Figure 6.10: Reconstructed cross-section using eight experimental projections without tube

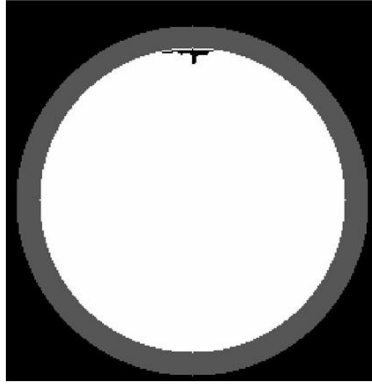


Figure 6.11: Reconstructed cross-section using eight experimental projections with tube

The results show that the presented statistical reconstruction technique is a promising technique to obtain accurate inversion results, even in the presence of an extremely limited number of X-ray projections and noise. The technique exploits the advantages of iteration methods, which make the solution more stable if an a priori information is introduced. Since standard FBP algorithm was employed as our first-level of reconstruction, the proposed reconstructed technique can be regarded as an improvement to FBP reconstruction in the case of an extremely low number of projections.

Chapter 7

Tikhonov Inversion Technique in X-ray Computed Tomography

7.1 Introduction

Given an object with 2-D spatial distribution of mass attenuation coefficients $\mu(x, y)$, the projection $p(s, \theta)$ or Radon Transform of μ at an angle θ is given as:

$$p(s, \theta) = \ln \left(\frac{I_0}{I} \right) = \int_L \mu(x, y) du \quad (7.1)$$

where

L is the path of the ray

u is the length along L

s are the sensor positions on the detector array

The object μ is usually reconstructed from these measured projections p using Filtered Back-projection (FBP) algorithm which is based on Radon Transform and the Fourier Slice theorem as discussed in Chapter 3 of this thesis. FBP however requires a very large number (hundreds and even thousands) of projections at uniformly-spaced axial or angular intervals. Any deviation from these strict requirements will produce undesirable artifacts in the FBP reconstructed image. In particular, in the presence of a limited number of projections, these artifacts are caused by insufficiently filled Radon space.

The mathematical problem of reconstructing an image from a limited number of X-ray projections is in general ill-posed and various statistical techniques have been developed to estimate solutions of such ill-posed problems [17, 51, 52]. However, these techniques are based on exploiting *a priori* knowledge introduced in iterative procedures. In this thesis, we use Tikhonov inversion technique for X-ray Computed Tomography that does not require any *a priori* information. The X-ray CT problem is reformulated in terms of matrix-vector product with incorporation of direct Tikhonov inversion technique.

7.2 Problem Formulation

Given the 2-D attenuation coefficient of size $M \times N$ in discrete form, the raysum p_j of Equation (7.1) for a particular projection θ of parallel ray geometry with N rays can be written as:

$$p_j = \sum_{i=1}^M l_{ij} \mu_{ij}, \quad j = 1, 2, \dots, N \quad (7.2)$$

where l_{ij} is the length of the j^{th} ray in the i^{th} cell.

Rewriting Equation (7.2) in matrix form, we get:

$$p = T\mu \quad (7.3)$$

where

p is the projection data

T is the projection operator

μ is the attenuation coefficient

For the case of limited number of projections, the inversion problem of evaluating μ from p in Equation (7.3) is ill-posed and underdetermined. For an underdetermined situation with a non-square T matrix, the general approach is to determine the least squares estimate of the solution obtained by minimizing the error function:

$$f(\mu) = \|p - T \cdot \mu\|^2 \quad (7.4)$$

The least square estimate is then given by:

$$\hat{\mu} = \left[T^T \cdot T \right]^{-1} \cdot T^T \cdot p \quad (7.5)$$

where T^T denotes transpose of T .

The solution obtained using Equation (7.5) is in general noisy and unstable. In order to obtain solutions to Equation (7.3) which are physically meaningful, additional constraints or regularization of the solution is necessary.

Regularization is a technique to solve inverse problems where additional information pertaining directly to the system parameters, is introduced as a penalty term. It takes into account the finiteness and imperfection of the data. Here the classical Tikhonov regularization technique is used [53]. The cost function in Equation (7.4) is modified by adding the regularization term and the solution is obtained by minimizing the cost function [53]:

$$f(\mu) = \|p - T \cdot \mu\|^2 + \lambda \|\mu\|^2 \quad (7.6)$$

where $\lambda \geq 0$ is the regularization parameter. This is the Tikhonov minimization problem. The first term on the right hand side of Equation (7.6) is the model error function and the second term is the regularization term. Using norm of the solution as the regularization term ensures that the value of the solution is restricted within some bounds. The regularization parameter controls the contribution of the regularization term. The functional $f(\mu)$ can be minimized for a given λ by:

$$\hat{\mu} = \left[T^T \cdot T + I \cdot \lambda \right]^{-1} \cdot T^T \cdot p \quad (7.7)$$

The proper choice of λ is the key element in the use of Equation (7.6). In choosing λ there is a tradeoff between fidelity to the measurements ($\lambda \rightarrow 0$) and small norm of the solution ($\lambda \rightarrow \infty$) [54]. If λ is chosen to be too small (*under-regularization*), then large high-frequency noise components will dominate the reconstruction. On the other hand, if λ is chosen to be too large (*over-regularization*), then important information in the data will be lost as the solution will be dominated by the effect of the regularization term.

There are several regularization methods at our disposal for choosing the Tikhonov regularization parameter λ in Equation (7.6) [55, 56, 57]. These methods include the *discrepancy principle*,

L-curve criterion, *normalized cumulative periodogram* (NCP) and *Generalized Cross-Validation* (GCV) criterion. Of all these methods, GCV is the most robust method and provides a scheme for which λ is independent of any orthogonal transformation of the measurement data p .

The basic principle of GCV is to perform the minimization by leaving out the measurement data points one at a time and to choose the value of λ which gives the best prediction of the missing data points as described next. Let $\mu_{\lambda,k}$ be the regularized solution obtained by minimizing the function:

$$\Phi_{\lambda,k}(\mu) = \sum_{q \neq k} \left| (T\mu)_q - p_q \right|^2 + \lambda \|\mu\|^2 \quad (7.8)$$

The cross validation function is defined as:

$$V_0(\lambda) = \sum_{k=1}^M \left| (T\mu_{\lambda,k})_k - p_k \right|^2 \quad (7.9)$$

The quantity $(T\mu_{\lambda,k})_k - p_k$ of Equation (7.9) is the discrepancy on component k . Thus, λ is chosen so as to minimize the error $V_0(\lambda)$.

The GCV function is defined as:

$$V(\lambda) = \frac{\|T\mu_{\lambda} - p\|^2}{[\text{trace}(I - T(\lambda))]^2} \quad (7.10)$$

where $T(\lambda)$ is defined as:

$$T(\lambda) = T \cdot T^T \cdot (T \cdot T^T + \lambda \cdot I)^{-1} \quad (7.11)$$

The regularization parameter λ in Equation (7.6) is thus chosen as the minimizer of the gener-

alized cross-validation function given as [58]:

$$V(\lambda) = \frac{\left[\sum_{k=1}^r \left(\frac{\lambda}{\mu_k^2 + \lambda} \right)^2 \cdot p_k^2 + \sum_{k=r+1}^m p_k^2 \right]}{\left[\sum_{k=1}^m \frac{\lambda}{\mu_k^2 + \lambda} \right]^2} \quad (7.12)$$

Here r and m are the rank and number of rows of the projection operator matrix T , and p_k is given as:

$$p_k = u_k^T \cdot p \quad (7.13)$$

where u_k is the k^{th} column vector of the left singular matrix U obtained by singular value decomposition (SVD) of the projection operator matrix T .

The implementation of the Tikhonov inversion technique is described next. Consider an object in an $M \times N$ imaging space, an X-ray source and detector with S sensors as shown in Figure 7.1.

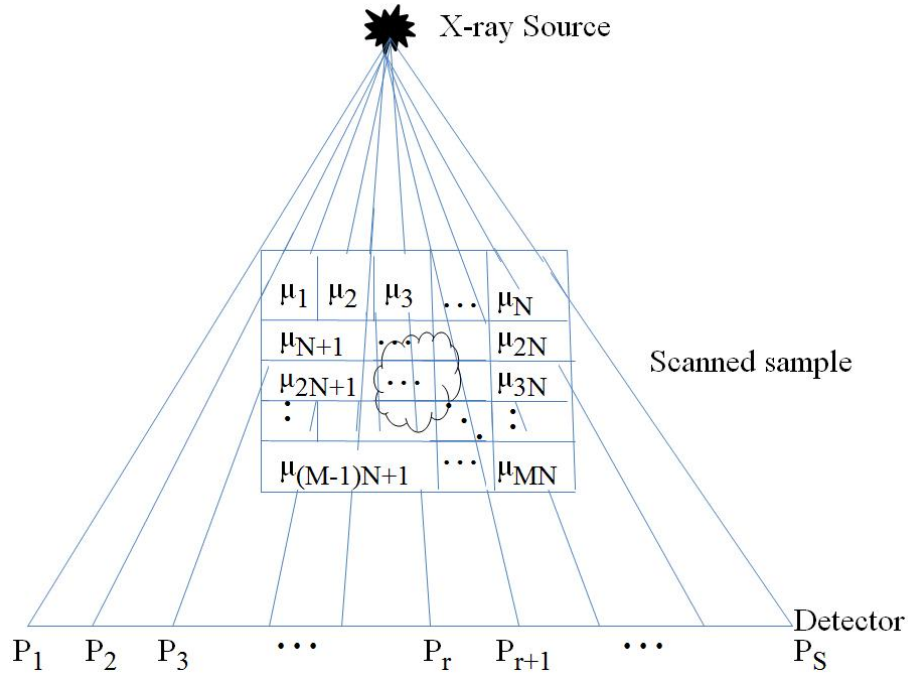


Figure 7.1: $M \times N$ imaging space in fan-beam geometry

In discrete form, Equation (7.3) can be written as a *ray-sum* for a particular projection:

$$p_r = \sum_{j=1}^{MN} l_{rj} \mu_j \quad r = 1, \dots, S \quad (7.14)$$

where μ_j is the attenuation of pixel j and r is a detector element of a detector array of S sensors.

For a particular projection, the matrix equation of Equation (7.3) will take the form:

$$\underbrace{\begin{bmatrix} p_1 \\ \vdots \\ p_r \\ \vdots \\ p_S \end{bmatrix}}_{S \times 1} = \underbrace{\begin{bmatrix} \gamma_{1,1} & \cdots & \gamma_{1,j} & \cdots & \gamma_{1,N} & \cdots & \gamma_{1,MN} \\ \vdots & \ddots & \vdots & \ddots & \vdots & \ddots & \vdots \\ \gamma_{r,1} & \cdots & \gamma_{r,j} & \cdots & \gamma_{r,N} & \cdots & \gamma_{r,MN} \\ \vdots & \ddots & \vdots & \ddots & \vdots & \ddots & \vdots \\ \gamma_{S,1} & \cdots & \gamma_{S,j} & \cdots & \gamma_{S,N} & \cdots & \gamma_{S,MN} \end{bmatrix}}_{S \times MN} \underbrace{\begin{bmatrix} \mu_1 \\ \vdots \\ \mu_j \\ \vdots \\ \mu_N \\ \vdots \\ \mu_{MN} \end{bmatrix}}_{MN \times 1} \quad (7.15)$$

where the elements of the projection operator matrix T in Equation (7.3) can be described following Equation (7.14) as:

$$[T] = T_{rj} = \gamma_{rj} = \begin{cases} 1 & \text{if } \mu_j \in \text{Ray Path} \\ 0 & \text{otherwise} \end{cases} \quad (7.16)$$

7.3 Implementation Results with Simulation Data

To demonstrate the validity of the Tikhonov inversion for tomographic reconstruction proposed in Section 7.2, a uniform circular phantom was simulated in a 128×128 imaging space using attenuation coefficients values of Tungsten obtained from the National Institute of Science and Technology (NIST) database [30]. The incident photon energy used in the simulation was 300 keV. Four low contrast circular defects were introduced in the simulated uniform circular phantom as shown Figure 7.2. The diameters of the phantom and each of the defects are 1.56" and 0.11" respectively. The mass attenuation coefficients of the host material and defects at 300 keV are $0.324 \text{ cm}^2/\text{g}$ and $0.292 \text{ cm}^2/\text{g}$ respectively.

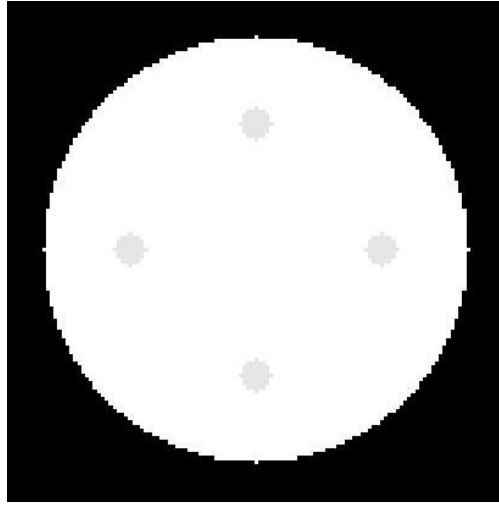


Figure 7.2: Phantom with Defects

X-ray projections were then obtained from the simulated phantom using Equation (7.2) for fan beam geometry over a complete rotation at angular increment of 36° . There are 185 rays per projection. A typical projection data obtained is shown in Figure (7.3) for the case of projection at angle 0° .

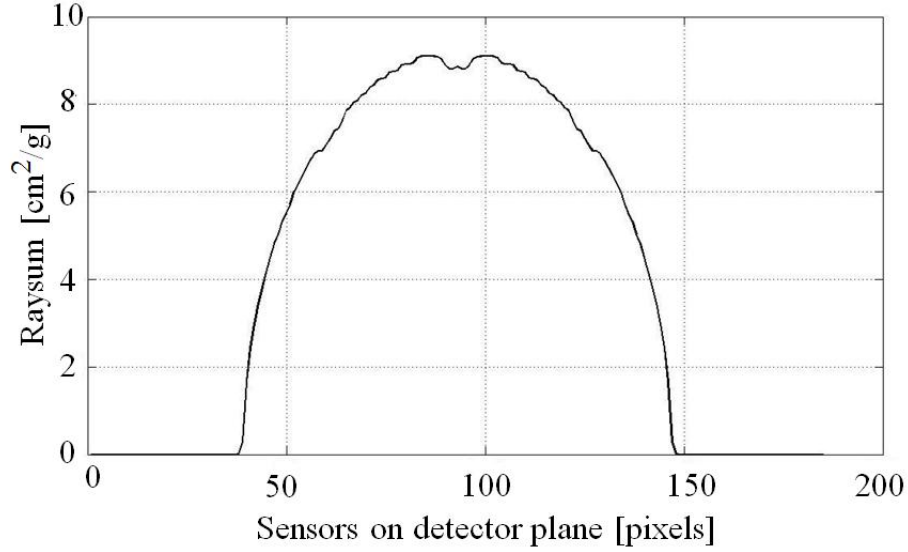


Figure 7.3: Simulated projection data acquired at angle 0°

The novelty of the proposed technique lies in the determination of the projection operator matrix T given in Equations (7.7) and (7.16). The following step-wise procedure is used for filling up the T matrix and reconstructing the object for all projection angles:

1. Initialize an $M \times N$ imaging space with no object
2. Initialize T matrix by creating a matrix of zeros
3. To provide complete fan coverage of the X-ray beam for all projections, pad the image space to $M_2 \times N_2$, where:

$$\begin{aligned}
 M_2 &= M + D \\
 N_2 &= N + D \\
 D &= \sqrt{M^2 + N^2}
 \end{aligned} \tag{7.17}$$

4. *for* $j=1:N_2$

for $i=1:M_2$

Set $R_1(i,j)=j$;

5. *for* $th=1:N_{proj}$; where N_{proj} is the number of projections

Rotate R_1 by angle θ_{th} to get R_2

Unpad R_2 back to size $M \times N$ to get R_3

for $jj=1:N$

$$R_4 = (\text{Find } R_3 = \left\lfloor \frac{D}{2} \right\rfloor + jj)$$

R_5 = Reshape the transpose of R_4 to $1 \times MN$

Set $T_{th}(jj, :) = R_5$

$$\mu_{th}^{\hat{}} = \left(T_{th}^T \cdot T_{th} + I \cdot \lambda \right)^{-1} \cdot T_{th}^T \cdot p_{th}$$

6. Final reconstruction: $\hat{\mu} = \frac{\sum_{th=1}^{N_{proj}} \mu_{th}^{\hat{}}}{N_{proj}}$

The reconstruction result with 10 simulated projections is shown in Figure 7.4. For comparison, the reconstruction was performed on the same 10 simulated projections using FBP algorithm and the result is shown in Figure 7.5.

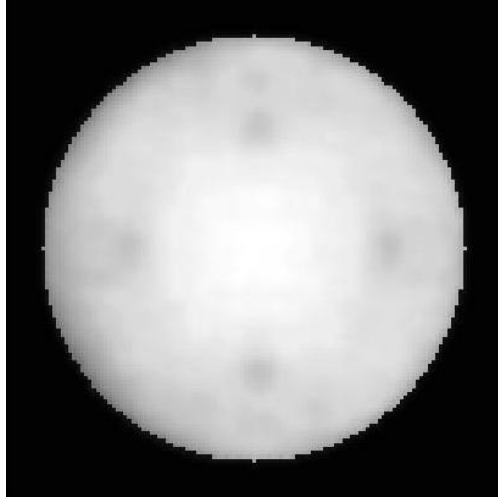


Figure 7.4: Reconstructed cross-section using 10 simulated projections

It is evident by comparing the reconstructed results in Figures 7.4 and 7.5 that the proposed technique is a promising technique for reconstruction from a limited number of projections.

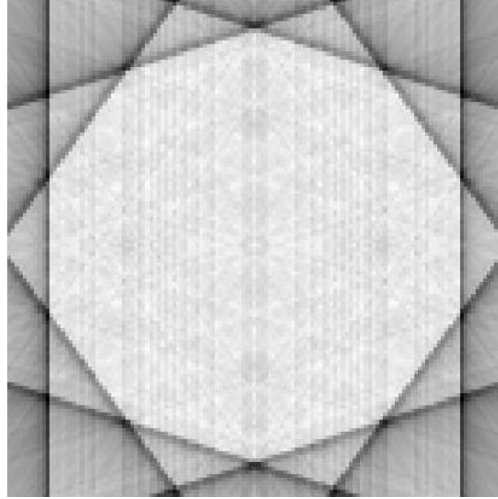


Figure 7.5: FBP reconstructed cross-section using 10 simulated projections

7.4 Results with Experimental Data

The validity of the technique was next tested using experimental data. The sample used in the experiment was an HDPE rod of diameter 1.56 ". Four defects, each of diameter 0.11 ", were machined along the axial direction of the rod. Figure 7.6 is a schematic diagram of the cross-section of the HDPE rod showing the machined defects with specified dimensions. The machined holes were filled with wood in order to reduce the contrast between the defect and the host material. The mass attenuation coefficient for HDPE is $0.203 \text{ cm}^2/\text{g}$ at 60 keV [30], while that for wood is $0.197 \text{ cm}^2/\text{g}$ at 59.54 keV [60].

Experimental projections were acquired using a GE vertical X-ray inspection system having a 150 kV_p microfocus X-ray source from Hamamatsu with peak current of 500 μA . The detector is a high resolution 12-bit CCD with 1024×1024 pixels, 4096 gray levels. The source-to-object and source-to-detector distances were 20 " and 36 " respectively. Since the X-ray source and detector are both fixed, the sample was mounted on a rotational stage to get a complete tomographic scan. This rotational stage was controlled by Labview software. The sample was rotated at regular

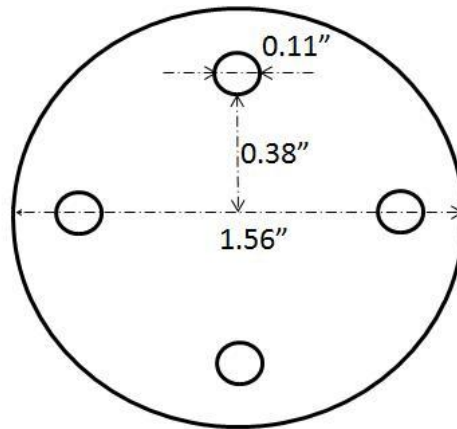


Figure 7.6: Cross-sectional diagram of the test sample with machined defects

angular intervals over a complete range (0° to 360°) to collect projection data from different directions. Figure 7.7 shows the side view of the sample mounted on the rotational stage inside the X-ray chamber. The X-ray source and the detector are not shown in the photo. A front view of the sample is also inserted in Figure 7.7.

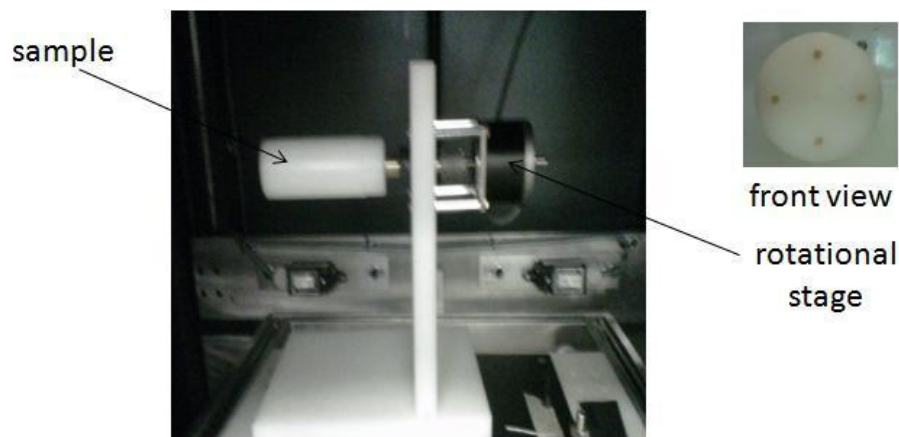


Figure 7.7: Side view of the sample mounted on a rotational stage. Front view of the sample also inserted

The tube voltage and current were optimized to acquire the best signal (radiographic data). The optimum values used for the sample in this experiment were 77.7 kV_p and $122 \mu\text{A}$. X-ray measurements were taken at 12 different orientations at angular increments of 30° . Figure 7.8

shows the raw 2-D radiographic data of the sample taken at angle 0° relative to the X-ray source.



Figure 7.8: Raw 2-D radiographic data of the sample taken at angle 0°

The 2-D raw data was preprocessed and log-normalized according to Equation (7.1) to give a 2-D projection data at that particular angle $\theta = 0^\circ$. For 2-D tomographic reconstruction of the sample, a 1-D projection data was taken from the 2-D projection data along the line A-A' indicated in Figure 7.8. The 1-D projection data for this orientation is shown in Figure 7.9.

A cross-sectional slice of the sample (with machined defects) was reconstructed by implementing the technique proposed above using 12 experimental projections. Figure 7.10 shows the reconstructed cross-section. Reconstructed result applying FBP on the same experimental projection is also given in Figure 7.11 for comparison.

As shown in Figure 7.11, the circular geometry as well as defects in the sample are not captured successfully using FBP technique due to insufficient number of projections. The reconstruction by the proposed technique is significantly better as compared to the FBP based reconstruction. The reconstructed values of μ for HDPE and wood are $0.157 \text{ cm}^2/\text{g}$ and $0.139 \text{ cm}^2/\text{g}$ respectively.

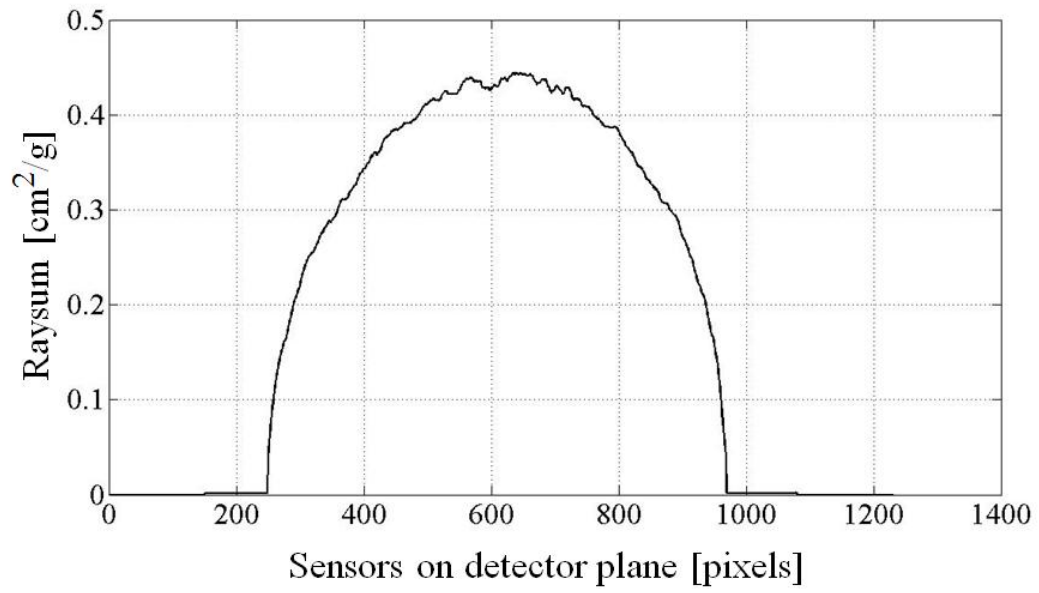


Figure 7.9: Projection data acquired at angle 0°

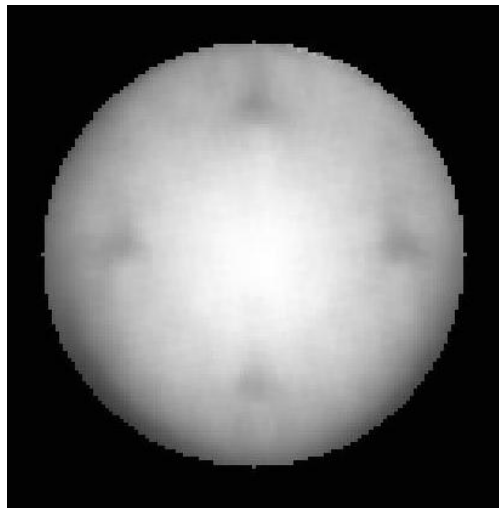


Figure 7.10: Reconstructed cross-section using 12 experimental projections

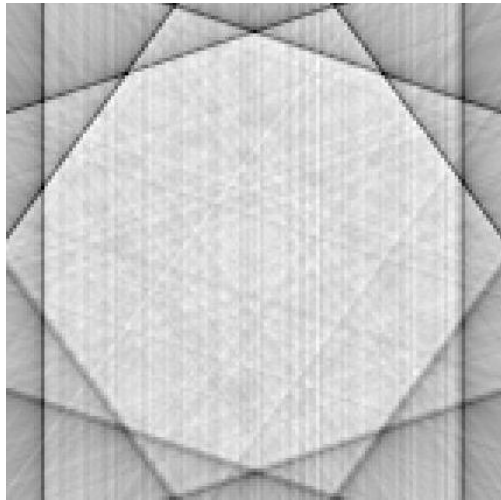


Figure 7.11: FBP reconstructed cross-section using 12 experimental projections

Chapter 8

Conclusion and Future Work

X-ray Computed Tomography (CT) is an important imaging modality in Nondestructive Evaluation and Biomedical applications, and will continue to be in the future. Its usage has dramatically increased over the last two decades. This calls for more research and development of new reconstruction algorithms that offer enhanced accuracy of images. This thesis presented novel algorithms for enhancing the quality of current X-ray CT images.

- Chapter 4 of this thesis proposes a physics-based beam-hardening correction scheme in X-ray CT given the source spectrum and CAD model of the object. This new technique exploits the underlying physics of beam hardening phenomenon by incorporating energy dependence in the Lambert-Beer's attenuation law. The proposed technique has been applied to both simulation and experimental X-ray data. The simulation results clearly demonstrate the importance of the correction scheme particularly when there is a low contrast defect in a sample. In the case of experimental data of a heavy tungsten sample, where the inherent cupping artifact due to beam hardening is apparent, the FBP reconstructed on BH corrected

projection data has greatly reduced the artifacts. Future work on the evaluation of the performance of the algorithm on more complex defect shapes and extensions of the algorithm to 3D reconstruction will further prove the efficacy of the technique.

- The problem of nuclear fuel rods inspection in the nuclear industry was discussed in Chapter 5. Current methods of nuclear fuel rods inspection were presented together with their drawbacks. The feasibility of using an X-ray tomographic inspection technique for detection and characterization of defects in fuel pellets was investigated. Limited number of projections is considered for reducing time for projection data acquisition. However a limited number of projections implies an insufficiently filled Radon Space rendering imaging via FBP algorithm not suitable. Filling up the Radon Space is essential to remove the artifact lines created in the reconstructed image by data insufficiency. Method of convex interpolation is simple and effective.
- A statistical reconstruction algorithm for reconstruction from a limited number of projections was presented in Chapter 6. The results from this study show that the presented statistical reconstruction technique is a promising technique to obtain accurate inversion results, even in the presence of an extremely limited number of X-ray projections and noise. Evaluation of the performance of the algorithm on more complex anomaly shapes is under progress. Work on optimizing the reconstruction algorithm with respect to computation time and reconstruction accuracy is also in process. Future work on the evaluation of the performance of the algorithm on more complex defect shapes and extensions of the algorithm to 3D reconstruction will further prove the efficacy of the technique.
- Availability of limited projection data renders computed tomography problem ill-posed. The X-ray CT imaging problem is reformulated in Chapter 7 to facilitate the application

of Tikhonov inversion technique. The ill-posedness in X-ray CT problem is addressed by Tikhonov inversion technique. Regularization parameter required in Tikhonov based inversion is computed using GCV method. Other variants of computing the regularization parameter will also be tried out in the future. There is also a strong potential of extending the proposed technique for imaging sample containing multiple materials as the technique does not require any *a priori* knowledge of the material distribution within the sample.

- For real time tomography, data acquisition time is critical. This calls for the need of tomographic reconstruction from limited number of projections. This thesis has presented novel algorithms for tomographic reconstruction from limited number of projection. These algorithms have strong potentials in biomedical applications where radiation dose to the patient is of paramount concern. One way to reduce such high radiation dose in current CT scanners is to perform tomographic reconstruction from fewer projections than presently used.
- The basic principle of conventional X-ray imaging is the absorption of the X-rays as they travel through an object. On the other hand, because X-rays are electromagnetic waves similar to visible light rays, their phase changes as they travel through an object. This phase change is generally observed as a refraction or interference and forms the basis of *phase contrast imaging* (PCI). PCI offers improved contrast sensitivity, especially in biomedical applications when imaging soft-tissue like breast. PCI is a promising technique to revolutionize breast imaging and diagnostic radiology.

BIBLIOGRAPHY

BIBLIOGRAPHY

- [1] D. E. Dudgeon and R. M. Mersereau, *Multidimensional Digital Signal processing*, PRENTICE-HALL, INC, 2000
- [2] J. Hsieh, *Computed Tomography: Principles, Design, Artifacts, and Recent Advances*, SPIE PRESS, 2003
- [3] F. Hopkins, Y. Du, B. Lasiuk, A. Abraham and S. Basu, *Analytical Corrections for Beam-Hardening and Object Scatter in Volumetric Computed Tomography Systems*, 16th World Conference on Nondestructive Testing, Aug. 30th- Sept. 3rd, 2004, Montreal, Canada
- [4] H. E. Johns and J. R. Cunningham, *The Physics of Radiology*, Charles C. Thomas, Springfield, IL, 1983
- [5] S. Iwamoto and A. Shiozaki, *Evaluation of the accuracy of CT numbers in statistical Correction of Nonlinearity for Polychromatic X-ray CT projection data*, Radiol. Phys. Technol., vol. 1, pp. 162-170, 2008
- [6] R. A. Brooks and G. D. Chiro, *Beam Hardening in X-ray Reconstruction Tomography*, Phys. Med. Biol., vol. 21, N^o. 3, pp. 390-398, 1976
- [7] R. E. Alvarez and A. Macovski, *Energy-Selective Reconstructions in X-Ray Computerized Tomography*, Phys. Med. Biol., vol. 21, pp. 733-744, Sept. 1976
- [8] N. Menvielle, Y. Goussard, D. Orban and G. Soulez, *Reduction of Beam-Hardening Artifact in X-Ray CT*, In Proceedings of the 2005 IEEE Engineering in Medicine and Biology, 27th Annual Conference, Shanghai, China, Sept. 1st- 4th, 2005

- [9] R. J. Jennings, *A method for comparing beam hardening filter materials for diagnostic Radiology*, Medical Physics, 15(4), pp. 588-599, July/Aug. 1988
- [10] G. T. Herman, *Correction for Beam Hardening in Computed Tomography*, Phys. Med. Biol., vol. 24, pp. 81-106, January 1979
- [11] G. T. Herman and S. S. Trivedi, *A Comparative Study of Two Post Reconstruction Beam Hardening Correction Methods*, IEEE Trans. Med. Imaging, vol.2, pp. 128-135, 1983
- [12] I. A. Elbakri and J. A. Fessler, *Statistical Image Reconstruction for Polyenergetic X-Ray CT*, IEEE Trans. Med. Imag., vol. 21, N^o. 2, pp. 89-99, Feb. 2002
- [13] H. S. Chueh, W. K. Tsai, C. C. Chang, S. M. Chang, K. H. Su and J. C. Chen, *Development of Novel Statistical Reconstruction Algorithms for Poly-Energetic X-Ray Computed Tomography*, Computer Methods and Programs in Biomedicine, vol. 92, pp. 285-293, 2008
- [14] P. Lekeaka-Takunju, S. S. Udpa and L. Udpa, *A Model-Based Correction Scheme for Beam-Hardening in X-ray Computed Tomography*, Research in Nondestructive Evaluation, (Under Review)
- [15] P. Lekeaka-Takunju, T. Khan, C. Bardel, J. Kim, K. Kryzwosz, S. S. Udpa and L. Udpa, *Assessment of Nuclear Fuel Pellets using X-ray Tomography*, International Journal of Applied Electromagnetics and Mechanics, vol. 33, N^o. 3-4, pp. 1267-1272, Oct. 2010
- [16] P. Lekeaka-Takunju, S. S. Udpa and L. Udpa, *Convex Interpolation Technique in X-ray Computed Tomography*, Materials Evaluation, (Under Review)
- [17] P. Lekeaka-Takunju, T. Khan, G. Harmon, S. S. Udpa and L. Udpa, *X-ray Tomographic Inspection of Nuclear Fuel Rods using a Limited Number of Projections*, Materials Evaluation, Vol. 69, N^o. 4, pp. 495-500, April 2011
- [18] P. Lekeaka-Takunju, T. Khan, S. S. Udpa and L. Udpa, *Tikhonov Inversion Technique in X-ray Computed Tomography*, Research in Nondestructive Evaluation, (Under Review)
- [19] E. Van de Castele, *Model-Based Approach for Beam-Hardening Correction and Resolution Measurements in Microtomography*, PhD Dissertation, Universiteit Antwerpen, June 2004
- [20] A. H. Compton and S. K. Allison, *X-rays in Theory and Experiments*, D. Van Nostrand, NY, 1935

- [21] C. L. Morgan, *Basic Principles of Computed Tomography*, University Park Press, Baltimore, 1983
- [22] M. J. Yaffe and J. A. Rowlands, *X-ray detectors for digital radiography*, Phys. Med. Biol. 42, pp. 1-39, 1997
- [23] M. Hoheisel, M. Arques, J. Chabbal, C. Chaussat, T. Ducourant, G. Hahm, H. Horbaschek, R. Schulz and M. Spahn, *Amorphous Silicon X-ray Detectors*, Journal of Non-Crystalline Solids, 227-230, pp. 1300-1305, 1998
- [24] U. Bick and F. Dickmann, *Digital Mammography*, Medical Radiology, Springer, pp. 13-31, 2010
- [25] W. Zhao, D. C. Hunt, K. Tanioka and J. A. Rowlands, *Amorphous Flat Panel Detectors for Medical Applications*, Nuclear Instruments and Methods in Physics Research Section A: Accelerators, Spectrometers, Detectors and Associated Equipment, vol. 549, Issue 1-3, pp. 205-209, Sept. 1st 2005
- [26] W. Harara, *Digital Radiography in Industry*, 17th World Conference on Nondestructive Testing, Shanghai, China, 25th-28th Oct. 2008
- [27] A. C. Kak, *Computerized Tomography with X-ray Emission and Ultrasound Sources*, Proc. IEEE, vol. 67, pp. 1245-1272, 1979
- [28] A. C. Kak and M. Slaney, *Principles of Computerized Tomographic Imaging*, IEEE Press, 1988
- [29] G. T. Herman, *Image Reconstruction from Projections: The Fundamentals of Computerized Tomography*, Computer Science and Applied Mathematics, Academic Press, Inc, New York, 1980
- [30] J. H. Hubbell and S. M. Seltzer, *Tables of X-ray mass Attenuation Coefficients and Mass Energy-Absorption Coefficients*
<http://physics.nist.gov/PhysRefData/XrayMassCoef>
- [31] A. Saffor, A. bin Ramli , K. Ng and D. Dowsett, *Objective and Subjective Evaluation of Compressed Computed Tomography (CT) Images*, The Internet Journal of Radiology, Vol. 2 N^o. 2, 2002

- [32] O. Diard, S. Leclercq, G. Rousselier, F. Azzouz and G. Cailletaud, *Modeling of Pellet-Cladding Interaction during power ramps in Pressurized Water Reactors*, Transactions, SMiRT 16, Washington DC, Aug. 2001
- [33] E. Mader, presentation on *Missing Pellet Surface Defects in Nuclear Fuel*, Electric Power Research Institute (EPRI), April 13th, 2009
- [34] N. Saratchandran, *Role of Nondestructive testing during Manufacture of Zircaloy Structural and Nuclear Fuel for Power Reactors in India*, In Proceedings of the 15th World Conference on Nondestructive Testing, Rome, Oct. 2000
- [35] W. C. A. Pereira, Z. D. Thome, J. M. Seixá and M. C. Bossan, *Ultrasonic Pulse-Echo Method for Failed Rod Detection Based on Neural Network*, Available at: <http://www.ndt.net/article/wcndt00/papers/idn008/idn008.htm>
- [36] H. Kwun, E. V. Mader and K. J. Krzywosz, *Guided Wave Inspection of Nuclear Fuel Rods*, Available at: <http://www.ndt.net/article/jrc-nde2009/papers/75.pdf>
- [37] M. S. Choi, M. S. Yang and H. C. Kim, *Detection of leak-defective fuel rods using the circumferential Lamb waves excited by the resonance backscattering of ultrasonic pulses*, Ultrasonics, Vol. 30, pp. 221-223, 1992
- [38] H. C. Kim, M. S. Choi and M. S. Yang, *Resonance scattering of acoustic waves from circular cylindrical shell and circumferential wave propagation*, J. Korean Phys. Soc., vol. 22, pp. 176-180, 1989
- [39] B. K. Kumar, A. Lakshminarayana, S. V. Kulgod, P. P. Deshpande, S. Palod, V. P. Singh and G. H. Rao, *Vision systems for inspection of nuclear fuel components*, In Proceeding of National Seminar on Non-Destructive Evaluation, Hyderabad, Dec. 7th - 9th, 2006
- [40] X. Song, *Nuclear Fuel Pellet Quality Control using Artificial Intelligence Techniques*, Ph.D Dissertation, University of Missouri-Rolla, Nov. 1999
- [41] S. Keyvan, X. Song and M. Kelly, *Nuclear Fuel Pellet Inspection using Artificial Neural Networks*, Journal of Nuclear Materials, 264, 141-154, 1999
- [42] A. Alghem, M. Kadouma and R. Benaddad, *NDT as a tool for Post-Irradiation Examination*, 17th World Conference on Non-Destructive Testing, Shanghai, China, 25th-28th, Oct. 2008

- [43] J. L. BATES, C. A. HINMAN and T. KAWADA, *Electrical Conductivity of Uranium Dioxide*, 68th Annual Meeting of the American Ceramic Society, Washington D. C., May 11th, (Refractories Symposium, N^o. 9-RS-66), 1966
- [44] J. E. Rosa da Silva, *Non Destructive testing of Irradiated Fuel Assemblies at the IEA-RI Research Reactor*, International Nuclear Atlantic Conference-INAC, Santos, SP, Brazil, Sept. 30th - Oct. 5th, 2007
- [45] <http://en.wikipedia.org/wiki/Zircaloy>
- [46] V. L. Vengrinovich and Y. B. Denkevich, *Multi Step 3D X-ray Tomography for a limited number of projections and views*, Review of Progress in Quantitative Non-Destructive Evaluation, Vol. 16, New York 1997
- [47] Z. Chen and R. Ning, *Filling the Radon domain in computed tomography by local convex combination*, Applied Optics, vol. 42, N^o. 35, 10th Dec. 2003
- [48] D.E. McClain, A.C. Miller and J.F. Kalinich, *Status of Health Concerns about Military Use of Depleted Uranium and Surrogate Metals in Armor-Penetrating Munitions*, NATO RTG-099 2005
- [49] F. Jian and L. Hongnian, *Beam Hardening Correction Method based on original sinogram for X-CT*, Nuclear Instruments and Methods in Physics Research A 556, pp. 379-385, 2006
- [50] <http://en.wikipedia.org/wiki/Uranium-235>
- [51] M. Bertero and P. Boccacci, *Introduction to Inverse Problems in Imaging*, CRC Press, 1998
- [52] A. Tarantola, *Inverse Problem Theory and Methods for Model Parameters Estimation*, SIAM, 2005
- [53] A. N. Tikhonov, *Solutions of Ill-Posed Problems*, Halsted Press, New York, 1977
- [54] Q. Zhang *et al*, *Coregistered Tomographic X-ray and Optical Breast Imaging: Initial Results*, Journal of Biomedical Optics, vol. 10, N^o. 2, March/April 2005
- [55] W. C. Karl, *Regularization in Image Restoration and Reconstruction*, Handbook of Image and Video Processing, A. Bovik, Ed., pp.141-160, Academic Press, 2000

- [56] H. W. Engl, M. Hanke and A. Neubauer, *Regularization of Inverse Problems*, Kluwer, Dordrecht, 1996
- [57] S. Orintara, W.C. Karl, D.A. Castanon and T.Q. Nguyen, *A Method for choosing the Regularization Parameter in Linear Inverse Problems*, In the Proceedings of the International Conference of Image Processing, vol. 1, pp. 93-96, 2002
- [58] T. Khan, P. Ramuhalli, W. Zhang and T. Raveendra, *De-noising and Regularization in Generalized NAH for Turbomachinery Acoustic Noise Source Reconstruction*, Noise Control Engineering Journal, vol. 58, N^o. 1, pp. 91-103, 2010
- [59] C. R. Vogel, *Computational Methods for Inverse Problems*, SIAM, 2002
- [60] D. A. Bradley, A. A. Tajuddin, C. W. Ahmad, C. W. Sudin, and S. Bauk, *Photon Attenuation Studies on Tropical Hardwoods*, International Journal of Radiation Applications and Instrumentation, Part A, Appl. Radiat. Isot., vol. 42, N^o. 8, pp. 771-773, 1991